

MATILDA: A MASS FILTERED NANOCUSTER SOURCE

by

GIHAN KWON

A DISSERTATION

Submitted in partial fulfillment of the requirements
for the degree of Doctor of Philosophy in the
Department of Chemical and Biological
Engineering in the Graduate School of
The University of Alabama

TUSCALOOSA, ALABAMA

2009

Copyright GiHan Kwon 2009
ALL RIGHTS RESERVED

Submitted by GiHan Kwon in partial fulfillment of the requirements for the degree of Doctor of Philosophy specializing in Chemical and Biological Engineering.

Accepted on behalf of the Faculty of the Graduate School by the dissertation committee:

Alan M. Lane, Ph.D

C. Heath. Turner, Ph.D.

Mark L. Weaver, Ph.D.

Gary J. Mankey, Ph.D.

Tonya M. Klein, Ph.D.
Chairperson

Viola L. Acoff, Ph.D.
Department Chairperson

Date

David A. Francko, Ph.D.
Dean of the Graduate School

Date

LIST OF ABBREVIATIONS AND SYMBOLS

BTU	British thermal unit
DOE	Department of Energy
PEMFC	Polymer electrolyte membrane fuel cells
FT-IR	Fourier transform infrared spectroscopy
UHV	Ultra high vacuum
STM	Scanning tunneling microscopy
DC	Direct current
RF	Radio frequency
PACIS	Pulsed arc cluster source
QMF	Quadrupole mass filter
WVF	Wien velocity filter
MSMF	Magnetic sector mass filter
TOF	Time-of-flight
amu	Atomic mass unit
PFMS	Pulsed field mass selector
V(t)	Total potential
VDC	Direct potential
VRF	Amplitude of radio frequency voltage
M	Ion mass
ΔM	Difference in mass between two resolvable peaks in a mass spectrum

R	Mass resolution
XPS	X-ray photoelectron spectroscopy
AFM	Atomic force microscopy
TEM	Transmission electron microscopy
CCD	Charged coupled device camera
STEM	Scanning transmission electron microscopy
EDX	Energy dispersive X-ray spectroscopy
EELS	Electron energy loss spectroscopy
ADF	Annular dark field
HAADF	High angle annular dark field
B. E	Binding energy
RFA	Retarding Field Analyzer
MFC	Mass flow controller
CEM	Channeltron electron multiplier
OD	Outside diameter
L/s	Litter per second
eV	Electron volt
FWHM	Full width at half maximum

ACKNOWLEDGMENTS

I would like to thank my advisors, Tonya Klein and Gary Mankey, for their consistent guidance, support, and encouragement in my research. I would like to thank my dissertation committee members, Alan Lane, Mark Weaver, and Heath Turner, for their valuable suggestions. I would like to thank my lab members, Harish Bhandari, Ping Chen, Lucas Falco, Shilpa Dubey, Jinwen Wang, Ning Li, and Kejing Li for their helping, kindness, and sharing. I am thankful for the opportunity to work with the nanocatalyst research team: John Wiest, Shane Street, David Nikles, Zhufang Liu, Wei Li, James Burgess, Chethan Acharya, and Brian Flowers. I would like to thank the faculty, staff, and graduate students of the Department of Chemical and Biological Engineering at the University of Alabama for their support. I would like to express my appreciation for financial support from Department of Chemical and Biological Engineering and also from DOE EPSCoR, Alabama EPSCoR, NSF equipment sharing, Central Analytical Facility, and KOSEF (Korea Science and Engineering Foundation). I really appreciate AJA international, Inc., the physics machine shop: David Key, Joe Howell, and Michael Perrigin; and the Physics electronic shop: Danny Whitcomb and Jason Kuykendall for their consistent supports.

I would like to thank my parents and my family for their encouragement and spiritual support.

Now faith is being sure of what we hope for and certain of what we do not see. This is what the ancients were commended for.

-Hebrews 11:1-2

CONTENTS

LIST OF ABBREVIATIONS AND SYMBOLS	iii
ACKNOWLEDGMENTS	v
LIST OF FIGURES	x
ABSTRACT.....	xiv
CHAPTER I. INTRODUCTION.....	1
Motivation.....	1
Preparations of Metal Catalysts	2
Impregnation Techniques.....	3
Colloid Chemistry Technique.....	3
Lithography Technique.....	4
Vacuum Technique	6
CHAPTER II. CLUSTER BEAM TECHNOLOGY	8
Cluster Source.....	8
Gas Condensation Cluster Source.....	9
Laser Ablation Cluster Source.....	10
Sputtering Cluster Source	11
Pulsed Arc Cluster Ion Source.....	13
Mass Filter	13
Quadrupole Mass Filter (QMF)	14
Wien Velocity Filter (WVF).....	16

Time of Flight (TOF).....	17
Pulsed Field Mass Selector (PFMS).....	18
Magnetic Sector Mass Filter (MSMF).....	18
CHAPTER III. CHARACTERIZATION TECHNIQUES.....	20
X-Ray Photoelectron Spectroscopy (XPS).....	20
Atomic Force Microscopy (AFM).....	21
Transmission Electron Microscopy (TEM).....	23
CHAPTER IV. EXPERIMENTAL SETUP.....	25
Matilda: Nanocluster System.....	26
Retarding Field Analyzer.....	32
Three-Element Lenses.....	34
Magnetic Sector Mass Filter for Mass Separation.....	36
Detection Methods of Charged Particle.....	38
Modification of Nanocluster Source.....	41
CHAPTER V. PERFORMANCE OF MATILDA.....	43
Pressure Ratio of Helium to Argon.....	43
Ion Energy Distribution.....	49
Ion Optics for Retarding Field Analyzer.....	54
CHAPTER VI. PROGRESS OF SIZE SELECTION OF CLUSTER.....	60
Beam Profile.....	60
Magnetic Field Distribution in Magnetic Sector Mass Filter.....	63
Size Selection of Cluster.....	64
2 nd Version of Lens for Focusing Beam.....	69

CHAPTER VII. CONCLUSION AND FUTURE WORK.....	72
Conclusions.....	72
Future Work.....	74
REFERENCES	76
APPENDIX A. SCHEMATICS OF NANOCLUSTER SOURCES.....	84
APPENDIX B. PERFORMANCE OF 1 ST VERSION OF NANOCLUSTER SOURCE.....	86
AFM Images (Scale: 1×1μm)	86
Experimental Conditions	88
Particle Size Distribution	88
TEM Images.....	89
Experimental Conditions	90
Particle Size Distribution.....	91
APPENDIX C. ION ENERGY DISTRIBUTION OF 1 ST VERSION RFA	92
APPENDIX D. SCHEMATIC OF APERTURE.....	94
APPENDIX E. LABVIEW PROGRAMMING	95
Depositter of Nanoclusters.....	95
Analyzer for Measuring Ion Energy Distribution.....	96
Detector for Measuring Ion Voltage Signal from CEM	96
APPENDIX F. SIMULATION CODING FOR RFA AND LENS.....	97
APPENDIX G. SIMULATION CODING FOR MSMF	102
APPENDIX H. MAXIMUM CLUSTER LANDING ENERGY.....	103

APPENDIX I. SCHEMATIC DIAGRAM OF 2 nd VERSION OF LENS AND LENS HOLDER	104
Schematic Diagram of 2 nd Version of Lens	104
Lens Holder.....	105

LIST OF FIGURES

1. Schematic diagram of a typical gas condensation cluster source	9
2. A laser ablation cluster source	10
3. Sputtering cluster source : (a) using an ion gun to accelerate ions to the target and (b) using a magnetron-based plasma as an ion source for sputtering	12
4. Mass filters for charged clusters: (a) RF quadrupole, (b) wien velocity, (c) TOF mass spectrometer with direct and reflection, and (d) pulsed filed mass selector. Δt is time delay between the end of acceleration pulse and the start of the deceleration pulse. U_p is the voltage pulse height.....	16
5. (a) Basic principle of the motion of an ions in a magnetic field. (b) The effect of a magnetic field on the ion trajectory. B is the magnetic field. F is the force on an ion in a homogeneous magnetic field. v is ion velocity	19
6. (a) The basic principle of X-ray photoelectron spectroscopy and (b) concentric hemispherical analyzer used in XPS.....	21
7. Schematic diagram of the AFM system in tapping mode.....	22
8. Schematic diagrams of (a) TEM and (b) STEM.....	24
9. Schematic of the sections making up the complete size-selected nanocluster source system	26
10. Schematic of the control system mounted on (a) sample holder/CEM, (b) accessory port including mass spectrometer, CEM holder, view port, and three electrical feedthroughs, (c) RFA, (d) sputter gun with target (red), (e) water in and out line, (f) electrical feedthrough port, (g) electrical lines for RFA grids, (h) pumping port for evacuating contaminant in aggregation tube, (i) convection gauge to measure pressure of aggregation tube, (j) gas mixture inlet line, (k) clamp for adjusting aggregation distance, and (l) electrical housing.....	28

11. Schematic of gas line: (a) 0 ~ +5 VDC for flow signal output, (b) 0 ~ 10 K Ω Heliport 10 turn potentiometer for controlling flow signal output voltage, (c) mass flow controller, (d) gas mixture line to introduce into aggregation tube, (e) Ar inlet line, (f) He inlet line, and (g) \pm 15 VDC power for mass flow controller. SCB-68 is a shielded I/O connector block for data communication between DAQ card and computer from National Instruments.....	29
12. Comparison with (a) Harberland type, (b) conventional type of magnetron sputter gun	30
13. Schematic of the basic principle of retarding field analyzer.....	33
14. (a) 1 st version and (b) 2 nd version of RFA, and their grids shown as insets. The holes on cover of (b) vent the gas mixture to prevent a short circuit at high voltage.....	34
15. SIMION simulation of an Einzel lens. (a) cross sectional view of an Einzel lens with electric potential line (red line). Two electrodes are set to ground potential, the middle electrode to +110V. (b) three-dimensional view of the three electrodes and the particle beam. (c) and (d) show focusing effect in a different electric field of middle electrode. Roll outward shows positive and roll inward indicates negative potential.	35
16. Picture of the three-element lenses used for Matilda.....	36
17. Schematic of MSMF for mass separation.....	37
18. Picture of MSMF: (a) cover, (b) neodymium block, (c) pink colored insulator, (d) supporter with bolt and nut, and (e) electrical connector.....	38
19. Schematics of (a) Faraday cup and (b) CEM for detection of negatively charged ions.....	39
20. The circuit of CEM with discriminator (AMPTEK A101 and PC-10 board).....	40
21. The pictures of the modification of the 1 st version cluster source. (a) Deposited place after deposition, (b) pumping port and feedthrough for RFA, and electrical line with (c) 1 st and (d) 2 nd versions of the RFA.....	42
22. (a) HAADF image, (b) EDX analysis of Ag on c-TEM grid in red circle area of (a), and (c) XPS spectra of Ag/Si. Red lines are for Ag and black lines are for substrate	45
23. TEM images of Ag on c-coated grid with RFA as pressure ratio of He to Ar (a) 0, (b) 2.5 (c) 4.5, (d) 6, and (e) 9.5 at 2" aggregation distance and 20 minutes deposition.....	46
24. Particle size distribution from Fig. 23.....	47

25. Saturation ion current vs. pressure ratio (He/Ar) at 20 watt sputter power (Pressure ratio = 0 (only 0.4 sccm of Ar))	48
26. Ion energy distribution with different sputter power at 2" aggregation distance and 0.4 sccm Ar flow rate (solid line is the indicator of the center of ion energy distribution)	50
27. Ion energy distribution with different aggregation distances at 20 watt sputter power and a 0.4sccm Ar flow rate	51
28. Ion energy distribution with different He flow rates at 0.4 sccm Ar with 20watt sputter power and 2" aggregation distance	52
29. Ion energy distribution with different acceleration voltages at a zero pressure ratio and at 0.4 sccm Ar with 20 watt sputter power and 2" aggregation distance. G1 and G2 are applied with an acceleration voltage and G3 is the retarding grid.....	53
30. Maximum cluster landing energy at different pressure ratios (He/Ar).....	54
31. (a) Five grids and ceramic spacer in retarding field analyzer with magnification of 100% transparency copper mesh (real grids have 80% transparence) of each grid. (b) Beam trajectories for retarding voltage (-5V) at G2 (200V). Initial K.E of black and red line = 5eV and other lines have 6eV. (c) Beam trajectories for retarding voltage (-9V) at G2 (200V). Initial K.E of black and red line = 9eV and other lines have 10eV. Sample holder is grounded.....	56
32. (a) Ion current and (b) number of particles collected from TEM images.....	57
33. TEM image and particle size distribution at -5V of retarding voltage with a 6.0 pressure ratio at G1 = +200V. Other grids and sample holder are grounded	58
34. TEM image and particle size distribution at -9V of retarding voltage with a 9.5 pressure ratio at G1 = +200V. Other grids and sample holder are grounded	59
35. RFA and three-element lenses in SIMION for the potential setting. G0: ground, G1 ~ C: +20V, V1 and V3: +20V, and V2: +100V. This condition makes the beam spread the least after passing the lens.....	61
36. (a) The distribution of ions from the simulation and (b) simulated and experiment at 0.15" from lens. The ion beam is approximately 0.2" in diameter. Blue line in (a) is the beam profile line for (b). Deflector can shift the experimental peak to the simulation result.....	61
37. The ion beam profile of 1.4" distance from MSMF. Beam diameter is 0.7"	62

38. The real area for size selection after MSMF. Beam diameter is 0.5" and 0.7" from direct behind and 1.4" from MSMF. Yellow color is magnet and gray color is the cover of magnets. CEM must be installed as close as possible to increase selection region. Six TEM grids (from 0 to 5 in red circle) were installed at the end of MSMF at intervals of 0.5". TEM grid (0 in red circle) is neutral position	63
39. Comparison between (a) real magnetic field and (b) simulated magnetic field. Red line is the size of magnet. Both show the magnetic field without magnets	64
40. Ion trajectories of (a) 50eV kinetic energy for low mass ($\geq 2.0\text{nm}$), (b) 4eV for the zero pressure ratio, and (c) 1eV kinetic energy for high mass ($\leq 2.0\text{nm}$).....	65
41. CEM data of Ag clusters at different positions.....	66
42. CEM spectrum of negatively charged Ag nanoparticles. 0 position of CEM is for neutral and large clusters. All signals of positions are averaged and normalized from the previous figure	67
43. Ag clusters on the TEM grids at the neutral position	68
44. Ag clusters on the TEM grids at the 0.5" position.....	69
45. 2 nd version of three-element lens. <i>a</i> is the holder for installation on the cluster source. <i>b</i> is the electrical connector. <i>c</i> is the holder for fixing three tubes (V1, V2, and V3). <i>d</i> is the ceramic rod from electric field. <i>e</i> is the hole for threaded rods which are connected with cluster source. <i>g</i> is the beam guider.....	70
46. (a) 2 nd version of Einzel lens to minimize the beam spread including <i>g</i> , beam guider. (b) Beam trajectory at V1 and V3 = +20V, V2 = +100V. (c) Beam trajectory at V1 and V3 = +1.0kV, and V3 = +2.0kV	71
47. Ion energy distribution at 4" aggregation distance	92
48. Ion energy distribution at 6" aggregation distance	93
49. Ion energy distribution at 8" aggregation distance	93

ABSTRACT

Cluster science provides a good model system for the study of the size dependence of electronic properties, chemical reactivity, as well as magnetic properties of materials. One of the main interests in cluster science is the nanoscale understanding of chemical reactions and selectivity in catalysis. Therefore, a new cluster system was constructed to study catalysts for applications in renewable energy. Matilda, a nanocluster source, consists of a cluster source and a Retarding Field Analyzer (RFA). A moveable AJA A310 Series 1"-diameter magnetron sputtering gun enclosed in a water cooled aggregation tube served as the cluster source. A silver coin was used for the sputtering target. The sputtering pressure in the aggregation tube was controlled, ranging from 0.07 to 1 torr, using a mass flow controller. The mean cluster size was found to be a function of relative partial pressure (He/Ar), sputtering power, and aggregation length. The kinetic energy distribution of ionized clusters was measured with the RFA. The maximum ion energy distribution was 2.9 eV/atom at a zero pressure ratio. At high Ar flow rates, the mean cluster size was 20 ~ 80 nm, and at a 9.5 partial pressure ratio, the mean cluster size was reduced to 1.6 nm. Our results showed that the He gas pressure can be optimized to reduce the cluster size variations. Results from SIMION, which is an electron optics simulation package, supported the basic function of an RFA, a three-element lens and the magnetic sector mass filter. These simulated results agreed with experimental data. For the size selection experiment, the channeltron electron multiplier collected ionized cluster signal at different positions during Ag deposition on a TEM grid

for four and half hours. The cluster signal was high at the position for neutral clusters, which was not bent by a magnetic field, and the signal decreased rapidly far away from the neutral cluster region. For cluster separation according to mass to charge ratio in a magnetic sector mass filter, the ion energy of the cluster and its distribution must be precisely controlled by acceleration or deceleration. To verify the size separation, a high resolution microscope was required. Matilda provided narrow particle sized distribution from atomic scale to 4nm in size with different pressure ratio without additional mass filter. It is very economical way to produce relatively narrow particle size distribution.

CHAPTER I

INTRODUCTION

Motivation

Fuel cell technology holds the promise of revolutionizing energy conversion in that it can provide an efficient and clean alternative to fossil fuel. Currently, fuel cells are used to provide power in stationary and portable power applications in remote locations or as emergency backup. However, future applications may include the replacement of the gasoline engine or integration of fuel cells as an integral part of a hybrid vehicle as well as to power portable electronic devices such as laptops and cell phones. A fuel cell generates electricity by a chemical reaction occurring at two electrodes separated by an electrolyte through which electrically-charged particles travel from one electrode to the other. A catalyst on the electrodes facilitates the reaction. Hydrogen is a basic fuel; however, other fuels such as methanol can be more convenient in that a liquid fuel is easier to store and transport and has a larger BTU/volume ratio. In either case, the hydrogen and oxygen used in generating electricity ultimately combine to form water as a harmless by-product, as well as CO₂ in carbon containing fuels.

The Department of Energy (DOE) Office of Efficiency and Renewable Energy's Hydrogen, Fuel Cells & Infrastructure Technologies Program has identified cost and durability as two of the main barriers to the commercialization of polymer electrolyte membrane fuel cells (PEMFC).¹ A major factor in cost is the catalyst material, which

contains precious metal such as platinum.² To minimize the amount of catalyst needed, a high surface to volume ratio of the catalyst particles is desirable to maximize the surface area available for the reaction. Proper dispersion of particle size enables low-load catalyst design for an overall lower system cost. In addition, particles must maintain their structure over the lifetime of the fuel cell, as a change in the morphology from the initial state would result in a loss of electrochemical activity. Agglomeration of particles due to diffusion and sintering is considered to be a major cause for the decrease in fuel cell performance, and this problem increases for smaller catalyst size distributions.³

As a model system, in order to understand the effect of the substrate-particle interaction as a function of nanoparticle size as well as the modification of the support, a nanocluster source (Matilda) was developed for the deposition of size-selected nanoparticles in a range from atomic scale to 10nm. The research team planned to develop Matilda (a mass filtered nanocluster source) to produce size-selected nanoparticles for further application of the observation of diffusion and sintering behavior using sophisticated surface analysis.

Preparation of Metal Catalysts

Several methods have been developed to load metal particles on high surface area support materials.^{4,5} Catalysts nanoparticles are deposited on a high surface area porous support so that large surface areas of the metal particles are catalytically active. This section has brief reviews of the most common methods for preparing a supported model catalyst, including their advantages and limitations.

Impregnation Technique

The standard method to produce catalysts is impregnation, a commonly used technique for the synthesis of heterogeneous catalysts, in which the porous oxide support is impregnated with metal precursors (e.g., H_2PtCl_6 for Pt and PdCl_2 for Pd) in a solution phase, followed by thermal treatment and/or reduction with H_2 to form metal nanoparticles.⁶ Typically, the active metal precursor is dissolved in an aqueous or organic solution. Then, the metal-containing solution is added to a catalyst support with the same pore volume as the volume of solution that was added. Capillary action introduces the solution into the pores of support. The catalyst can then be dried and calcined to remove undesired and volatile components within the solution, to activate the catalyst, and to load the metal on the catalyst surface.⁶ This method is good for the large scale production of catalysts,⁷ and the particle size distribution produced on the support is nonuniform in size, shape, and metal-support interaction as well as structure.^{6, 8} On the other hand, stable catalysts at operating temperatures are produced with a high particle density.⁶

Colloid Chemistry Technique

Colloid chemistry is one of the main techniques for the synthesis of size controlled nanoparticles of metal, semiconductor, and magnetic materials. Synthesis of particles using this technique has several advantages. The colloidal technique can not only precisely control the particle size up to 30nm, but also shape, to some extent. In addition, it has high throughput and enlarges the surface area of particle-loaded 3D support surfaces such as carbon nanotube and mesoporous materials.⁹ The reaction for synthesizing particles is the reduction of metal salt in solution. Capping agents are used

for stabilizing nanoparticles and preventing them from aggregation. The capping agent, bound to nanoparticles, needs to be activated by thermal treatment in an inert environment or in oxygen, followed by reduction, to produce an active catalyst.⁹ Too high temperatures lead to the agglomeration of particles, and too low temperatures lead to surface contamination from capping agents blocking the active sites of nanoparticles.⁹ FT-IR can be used to observe the removal of capping agents bound to particle surfaces, which involves the removal of oleylamine and oleic acid on Pt₃Sn nanoparticles by repeated washing of the particles in ethanol and TMAOH.¹⁰ Heat treatment is one of the most appealing methods, with a low temperature activation approach preventing the growth of the particle.¹¹ Thermogravimetric analysis showed a distinct weight loss regime providing evidence for the removal of the capping agent.^{7, 11, 12}

Lithography Technique

Impregnation and colloidal methods are well known methods for producing commercial catalysts. These methods do not provide a narrow distribution of particle size, uniform inter-particle distance, uniform surface morphology, or invariability of sites on which catalysts are deposited. Many results show that the reaction efficiency of a catalyst depends on the particle size, the interaction between metal and support, and interparticle distance can be very important for explaining a catalyst's efficiency. Some well-known examples of this are the size dependence of the turnover frequency on gold nanoparticles for the low temperature oxidation of CO.¹³⁻¹⁶ It would be beneficial to make catalysts which are uniform in size and uniform in distance, with a specific geometric relationship between particles. Unsuccessful attempts have been made using electron beam

lithography to define regular arrays of platinum nanoparticles on ceria and silica. The attempts were unsuccessful in that the smallest particle size achieved was about 30nm which is an order of magnitude too large when compared to the anomalous activity range of 1-10nm. An array of platinum particles on ceria surfaces has been made with this method.^{6, 17} It has been shown that the particles on ceria support do not have thermal stability while the maintenance of the integrity of nanoparticles is an important matter in catalyst development. This method was inspired by technology used for the fabrication of semiconductor devices.¹⁸⁻²⁰ The fabrication of an array of platinum nanoparticles requires multiple steps and is slower than other processes. The first step is the deposition of a film of aluminum on a silicon substrate followed by oxidation of the film for making the oxide support. This is then followed by the spin coating of a polymer resist, which decomposes when it is exposed to an electron beam. The beam produces a series of dots in the film when the polymer resist is dissolved and then removed in a solvent, while the unexposed polymer areas are not removed. This process leaves the polymer film with a series of holes which are the underlying alumina. After, the platinum is deposited on this surface and then is washed with a solvent in order to dissolve the resist. Finally, a series of platinum dots is left in the holes in the resist which were exposed by electron beam. Although these processes can produce a regular array of catalysts, there are several problems in them. First, electron beam lithography has limited resolution. Currently, the interesting regime of catalyst research is around 1nm, while the production limitation is only 20nm. Second, a catalyst needs some special characteristics, such as thermal stability and resistance to sintering so that the integrity of uniformity is unchanged.²¹

Vacuum Technique

Single crystal surface science began with the development of surface science techniques in the 1960s and was used to observe the basic mechanisms of adsorption, desorption, dissociation, and the discovery of simple reaction mechanisms. Model catalysts were studied to evaluate the desorption-adsorption properties of vapor-deposited metal particles on supports under UHV.^{22, 23} The metal particles, the size of hundreds and thousands of atoms, revealed particle-size-dependent behavior for catalytic reactions. Currently, many people are developing size-selected cluster sources to investigate many different applications such as catalysis,²⁴⁻²⁷ irradiation,^{28, 29} cluster landing,^{30, 31} giant magneto-resistance,³² and biological applications.³³ Little research has been done on catalysts in size regime (<100 atoms) where the fundamental electronic structure can be changed. The properties of model catalysts were reviewed by depositing size-selected clusters on oxide surfaces. Benzene production was studied through acetylene on a size-selected Pd_n cluster from 1 to 30 atoms soft landed on MgO(100).²⁴ Benzene was mainly produced at 300K for small clusters from 1 to 6 atoms, while 430K was the temperature threshold for larger clusters from 7 to 30 atoms. It was suggested that at high temperature, benzene was produced on both single Pd atoms and on 3-fold Pd hollow sites. CO oxidation was also performed on a size-selected Pt_n from 8 to 20 atoms on MgO(100) substrates, and it was found that activity dramatically increased from a minimum at Pt₈ to a maximum at Pt₁₅ for CO oxidation.^{8, 26} Different oxidation temperatures for different cluster sizes was explained by changes in the cluster ionization potential. Using model catalysts prepared by size-selected Au ranging from 1 to 7 atoms on TiO₂, it was found that the activity of CO oxidation was not correlated to CO binding or cluster morphology

but was a strong function of cluster size.²⁷

The use of size-selected and supported clusters is promising for the investigation of size dependence of chemical reactions on small clusters, which is a crucial issue for fuel cells. This method can be utilized with any metal of any cluster. The main limitations are that it will be useful only for planar supports and the uncertainty of the cluster size distribution after deposition. Soft landing of clusters on the support may provide uniform size clusters without deformation, but there have been no experimental results so far. Soft landing of clusters can be achieved by applying the same polarity of voltage as the charged clusters on a decelerating grid or substrate. It is necessary to test size uniformity, migration and sintering on elevated temperatures using microscopes, such as STM.⁸

CHAPTER II

CLUSTER BEAM TECHNOLOGY

A cluster source for producing nanoscale metal clusters with a wide range of sizes by the gas evaporation-condensation method was formulated 28 years ago.^{34, 35} Laser ablation and sputtering have also been utilized as the technology has been developed. These four cluster sources will be introduced in this chapter. It has already been seen that the cluster properties are size-dependent, especially for catalysts.¹³ For cluster deposition experiments for catalysts, size-selection of the cluster beam is desired to understand size-dependant catalytic behavior. Mass filters for size-selection of clusters use the different kinetic energies or the mass-to-charge ratio of the cluster to disperse the beam. Currently, many different mass filters are presented for mass selection, such as the quadrupole, wien velocity, time of flight, and pulsed field mass filters.³⁶

Cluster Source

Although many different types of cluster sources are being used now, the basic design idea to produce clusters is always the same: the production of clusters by condensation from vapor. This concept is introduced in the four most common cluster sources in the following subsections.

Gas Condensation Cluster Source

The first generation of gas condensation cluster sources is the original type of cluster source.³⁴ Thermal evaporation is used to produce metal vapor into flow of cold inert gas. The cold inert gas cools the vapor which is grown into clusters. A schematic of a gas condensation cluster source is shown in Figure 1.³⁶ The metal is evaporated from a crucible and then flows into the stream of inert gas from the inlet tube. The clusters formed are moved from the growth region to the skimmer by the inert gas. The clusters undergo a supersonic expansion at the skimmer which creates a molecular beam of clusters and inhibits further cluster growth. An ionization stage is required to make ionized clusters for the separation based on mass-to-charge.³⁶

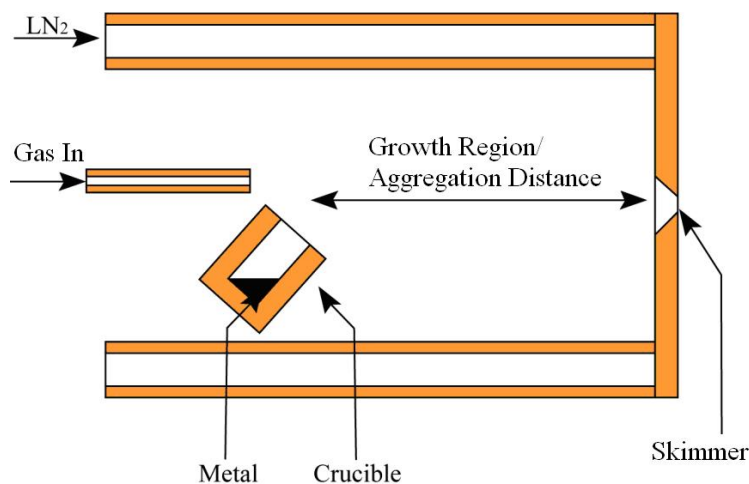


Figure 1. Schematic diagram of a typical gas condensation cluster source.

The size distribution of clusters can be controlled by changing the crucible temperature, inert gas pressure, and the aggregation distance. The gas condensation

cluster source has the advantage of producing a wide size range of clusters with a high intensity as well as being inexpensive to setup. However, this cluster source is likely to suffer from instabilities ; the size distribution and intensity of the cluster beam can change due to the formation of metal whiskers around the skimmer as well as the difficulty in controlling the evaporation rate during long deposition. Another disadvantage is that the melting point of the materials limits the selection of material for cluster.³⁶

Laser Ablation Cluster Source

Figure 2 is a schematic of a laser ablation cluster source.³⁶ A high power pulsed laser is focused on the rotating target during operation and then produce atoms, small clusters, and ionized clusters from rotating target.

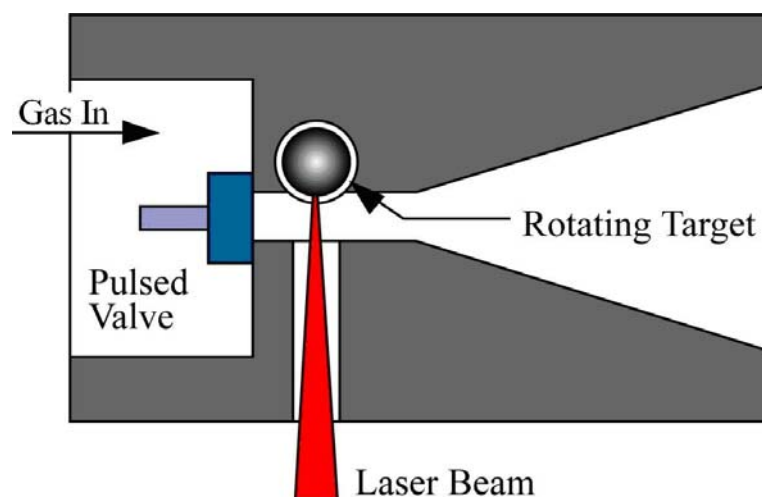


Figure 2. A laser ablation cluster source.

A proper condition for clustering can be achieved by ensuring that the laser pulse coincides with a pulse of inert gas across the target. The clusters grow in the nozzle as the metal vapor meets the inert gas. Then, the cluster and gas mixture undergoes strong supersonic expansion as they are ejected. Many of the small clusters are ionized, but the larger clusters need an additional ionization process for mass separation. During the laser pulse, the size distribution can be controlled by changing the average gas pressure.³⁷ The laser ablation cluster source is popular because of its stability and the high intensity achievable. Unlike the gas condensation cluster source, the laser ablation cluster source is not limited by the melting point of target materials and is much more flexible. Also, the application of phasing can be used to produce binary clusters with two targets, since it can control the distribution of elements in the cluster.³⁸ The disadvantages of the laser ablation cluster source are the very expensive laser required.

Sputtering Cluster Source

The surface of a target is bombarded by high energy ions from plasma during sputtering. These ions provide a continuity of atomic collision events on the target resulting in the production of atoms and small clusters from the surface of the target. Usually, an inert gas is used bombarding the surface of the target. Sputtering cluster source has the advantage that any material can be sputtered by DC or RF potential, despite differing yields of material. Cluster sources utilizing sputtering have a greater versatility. Figure 3 shows two methods for sputtering. In Figure 3(a), argon ions bombard the surface of a target from an ion gun. The incident energy and angle of the ions on the target is controlled to optimize the flux of clusters.

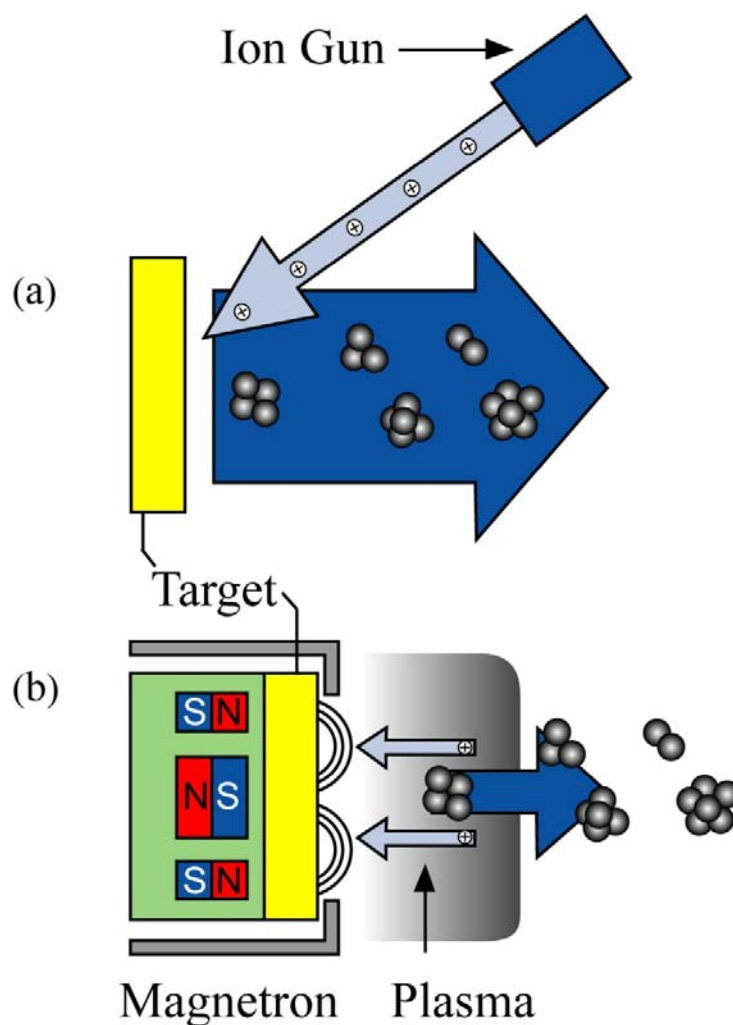


Figure 3. Sputtering cluster source: (a) an ion gun based sputter source and (b) a magnetron based sputter source to produce clusters.

In Figure 3(b), plasma is occurred over the target by a DC or RF potential to the target and confined by a magnetic field. It is called magnetron sputtering. Argon ions are accelerated from the plasma into the target by high biased voltage of target, inducing

sputtering. The portion of sputtered atoms and small clusters are ionized during their flight from the target through the plasma consisting of neutral, positive, and negative ions. Normally, the cluster yield of positively charged clusters is higher than that of negatively charged clusters.³⁹ Magnetron sputtering with gas condensation has been developed to produce a wider range of cluster sizes.^{40, 41} This cluster source is able to produce a high intensity cluster beam with sizes from a atom to several thousands of atoms. The clusters produced by magnetron sputtering are charged without an additional ionization stage. This type of cluster source also has the advantage of good stability and a wide range of materials.

Pulsed Arc Cluster Ion Source

Pulsed arc cluster ion source (PACIS) is similar to the laser ablation cluster source, but the evaporated plume is produced by a high pulsed arc between two electrodes made of the target material, coinciding with the pulse of inert gas. Then, the target is sputtered to form a vapor and small cluster.⁴¹ It can produce 10% ions in the beam and does not require the high power pulsed laser and an ionization stage to make the ionized cluster.³⁶

Mass Filter

The mass filter provides two important roles, which are mass analysis and the filtering of clusters. A mass analysis from a cluster source provides the most valuable information for developing cluster sources and experiments with cluster beams. Also, mass selection is needed for the study of size-dependent properties in many different

experiments. Size selection is beneficial for the possibility of the creation of monodispersed clusters on surfaces. Basically, cluster beams have to be ionized for size selection. The ionization of the cluster beam is attained in the cluster source itself or by a secondary ionization stage involving a plasma, electron bombardment and laser ionization. After ionization, the clusters can be size-selected as a function of their velocity or their charge to mass ratio. The following sections describe mass-selection techniques: quadrupole mass filter,⁴²⁻⁴⁵ Wien velocity filter,^{46, 47} time-of-flight^{48, 49}, pulsed field mass selector,^{50, 51} as shown in Figure 4³⁶, and the magnetic sector mass filter.^{28, 39, 52,}

53

Quadrupole Mass Filter (QMF)

The quadrupole in Figure 4(a) is the most widely used analyzer due to its ease of use and a relatively accessible price. The quadrupole is composed of two pairs of metallic rods, one of which is set at a positive electric potential and the other at a negative potential. A combination of DC and RF voltages is applied on each set. Total potential $V(t)$ applied to the rods is given by Equation (1).

$$V(t) = \pm(V_{DC} + U_{RF}\cos(\omega t)) \quad (1)$$

In this equation, V_{DC} is direct potential, U_{RF} is the amplitude of radiofrequency voltage, and ω is the frequency of RF potential. The positive pair of rods acts as a high mass filter. The other pair acts as a low mass filter. The resolution depends on the dc value in relationship to the RF value. The quadrupole is operated at constant resolution, which means that the RF/DC ratio is maintained at a constant level. For given amplitudes of the dc and RF voltages, only the ions of a given mass-to-charge ratio will resonate, have a

stable trajectory to pass the quadrupole, and be detected. Other ions will be destabilized and hit the rods. The performance (i.e., ability to separate two adjacent masses across the applicable range) depends on the quad geometry, on the electronics, on the voltage settings, and on the quality of the manufacturing. Increasing the resolution means that fewer ions will reach the detector and consequently impacts the sensitivity. The quadrupole is scanned with A (DC voltage)/ Q (RF voltage) = constant; the resolution depends on the slope of the scan line. The main disadvantages are the limited mass selection range and the low energy ion beam, which can incur a space charge problem. To increase the mass selection range, a high frequency power supply is required. Space charge problems can result in the malfunction of mass selection.⁵⁰

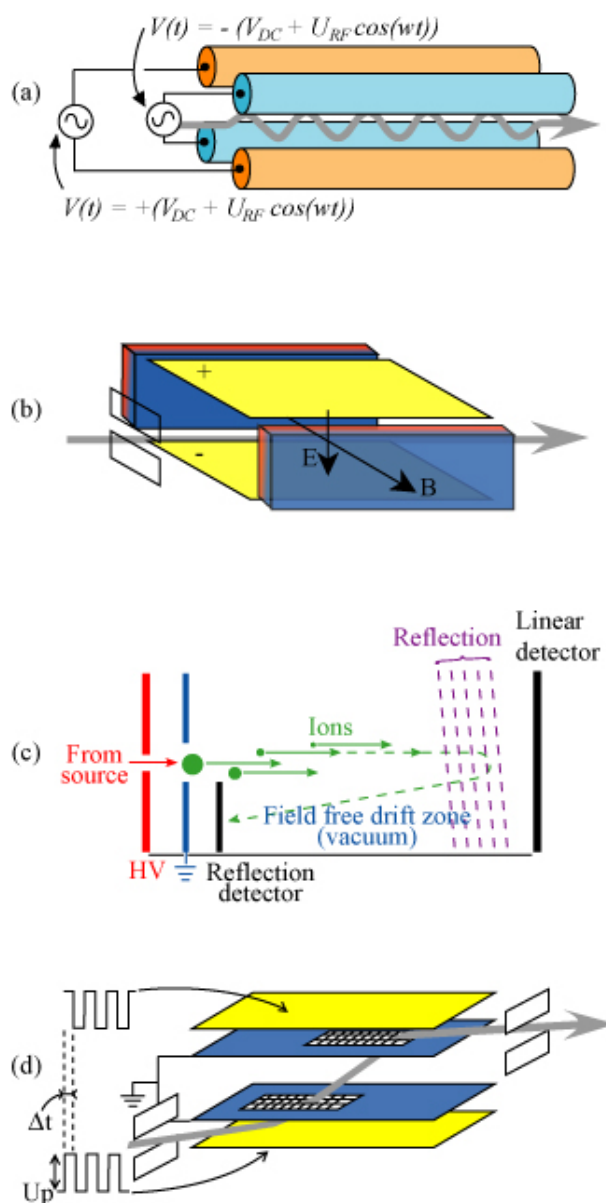


Figure 4. Mass filters for charged clusters: (a) RF quadrupole, (b) Wien velocity, (c) TOF mass spectrometer with direct and reflection, and (d) pulsed field mass selector. Δt is time delay between the end of acceleration pulse and the start of the deceleration pulse. U_p is the voltage pulse height.

Wien Velocity Filter (WVF)

The Wien velocity filter, employing perpendicular electric and magnetic fields

normal to ion trajectory, can serve to deflect the cluster beam according to either mass or energy, as shown in Figure 4(b). Only ions that have a charge/velocity ratio balanced with the force of the electric and magnetic field is transmitted through the filter without deflection, and the others are deflected according to size. The advantages are the ease installation with the cluster source, due to the size of the setup, and an undeflected beam after the selection process. It is only good for small clusters, due to the fact that velocity is inversely proportional to mass.^{46, 47}

Time-of-Flight (TOF)

Recently, the time-of-flight mass analyzer in Figure 4(c) has provided a very high resolution (resolution of $M/\Delta M = 1000$ at mass = 108amu).⁵⁴ Unlike other techniques, the time-of-flight technique uses the velocity of cluster by a given short impulse. The velocity of the clusters is inversely dependent on the square root of their masses. Ionized clusters are generated by the source and accelerated through an electric field into the TOF analyzer. Ions with a narrow kinetic energy distribution are required to prevent the reduction of resolution. The ion beam moves along and drifts some distance before being detected. As clusters in the beam have different velocities depending on its mass, they arrive at the detector at different times. The lightest clusters will reach the detector first. Then, a mass spectrum is plotted as the cluster current versus time, resulting in peaks with respect to each cluster mass. For size-selecting a cluster, this technique has two major drawbacks. The first is the benefit of high resolution, which comes at the cost of high transmission, as the use of a small beam pulse, leads to long deposition times. The second is that all the clusters hit the detector, only separated in time.⁵⁰ For these reasons,

the time-of-flight mass analyzer is not suitable for cluster deposition. To solve the low transmission and the spatial separation for cluster deposition, new configuration of time of flight mass filter, called pulsed field mass selector, is introduced

Pulsed Field Mass Selector (PFMS)

The pulsed field mass selector utilizes an electric field pulse, which is applied to both the top and bottom plates to displace an ion beam laterally into a field-free region (two plates in the center, as seen in Figure 4(d)).⁵⁰ There is a time delay (Δt) between acceleration at the bottom plate and the deceleration pulse at the top plate. After an acceleration pulse to introduce the beam into the field-free region plates, a deceleration pulse follows and changes the direction of the beam to evacuate the beam into aperture. Mass selection is determined by the time difference between acceleration and deceleration pulses. It filters a Pd cluster up to $9.0 \pm 2.0\text{nm}$ with a transmission greater than 50% with a mass resolution given by $R = \frac{M}{\Delta M}$.⁵⁵ It provides a mass resolution from 20 to 50. Though it does not provide high mass filter resolution, it is enough to study cluster deposition. A proper tuning is required for optimal cluster flux in real experiments.

Magnetic Sector Mass Filter (MSMF)

The most well known type of mass filter is the magnetic sector mass filter. The MSMF disperses the charged clusters accelerated from the cluster source into curved trajectories that depend on the mass-to-charge ratio of the charged cluster, as seen in Figure 5(a).⁵⁶ In a MSMF, clusters leaving the ion source are accelerated to a high kinetic energy. Then, the ions pass through an MSMF in which the magnetic field is applied in a

direction perpendicular to the direction of ion motion. Light mass clusters are more easily deflected than heavy clusters if kinetic energy and charge of both are the same. Neutral clusters just pass the magnetic field without changing their trajectory because they are not influenced by the magnetic field, as seen in Figure 5(b).⁵⁷

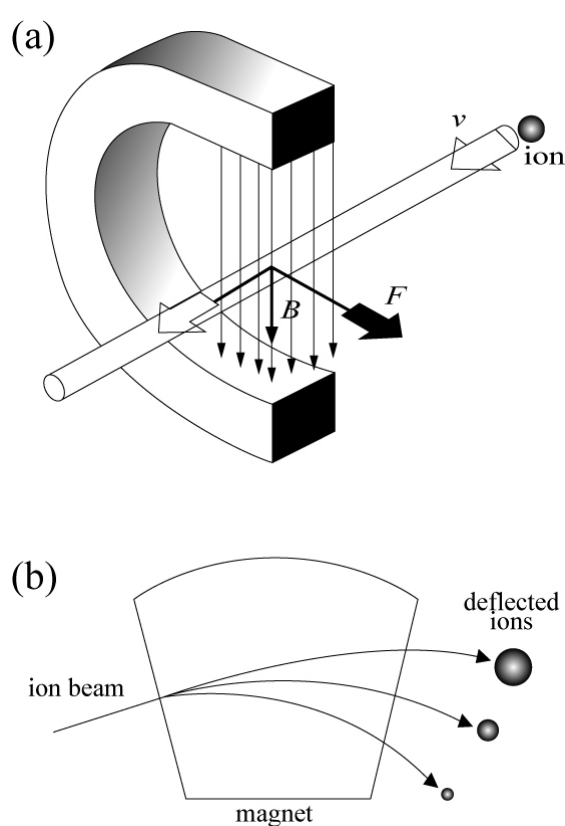


Figure 5. (a) Basic principle of the motion of an ion in a magnetic field. (b) The effect of a magnetic field on the ion trajectory. B is the magnetic field. F is the force on an ion in a homogeneous magnetic field. v is ion velocity.

MSMF mass filter works well for smaller clusters, but large magnets are required for

large clusters. The mass resolution with a magnetic field analyzer (AMD Intectra GmbH)

has been measured at $M/\Delta M = 300$, as Cs^+ cations were deposited.⁵³

CHAPTER III
CHARACTERIZATION TECHNIQUES

X-Ray Photoelectron Spectroscopy (XPS)

X-ray photoelectron spectroscopy is a well known technique for chemical analysis in surface science. The XPS technique provides qualitative and quantitative data on elements by inducing photoemission and is a nondestructive method.⁵⁸ An x-ray beam irradiates the surface of the sample to induce photoemission from both the core and valence levels of surface atoms into the vacuum level, as seen in Figure 6(a). Some of electrons emitted during photoemission are selected by a concentric hemispherical analyzer which has two electric fields to separate electrons according to their kinetic energy; they are collected by either a microchannel plate or a channeltron electron multiplier, as seen in Figure 6(b).⁵⁹ The kinetic energy of the emitted electron is measured by Equation (2):

$$E_K = h\nu - E_B - \Phi, \quad (2)$$

where $h\nu$ is the photon energy of the x-ray source from either Mg K α (1253.6 eV) or Al K α (1486.6 eV), E_B is the binding energy (BE) of the emitted electron in a solid and depends on the type of element and environment, and Φ is the spectrometer work function. The binding energy of the photoelectron can be calculated by utilizing Equation (2) and measuring the kinetic energy of an emitted electron from a solid with the known

values of $h\nu$ and Φ . Thus, XPS not only derives quantitative information from an element's surface, due to the unique binding energy of each element, but also provides the chemical state of the element.

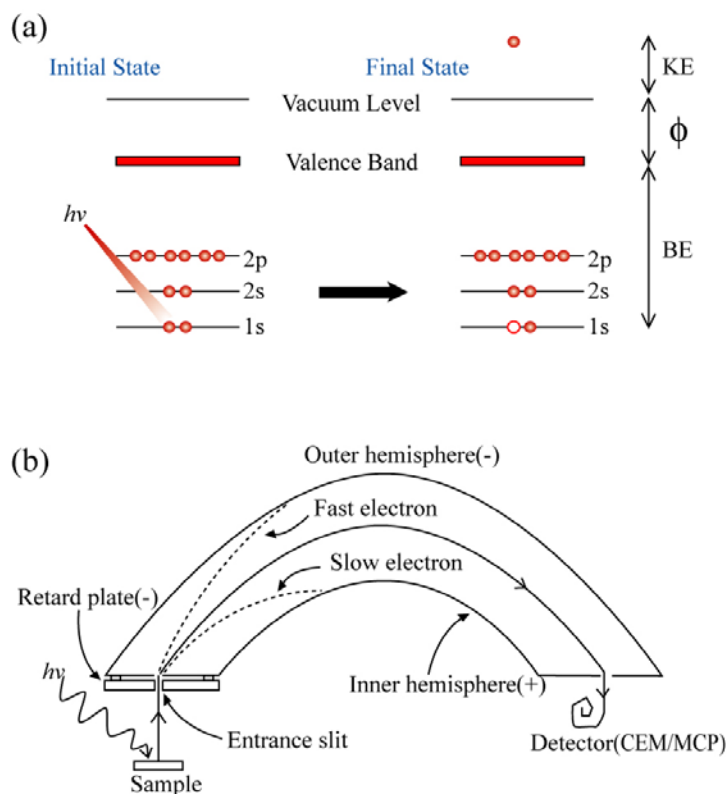


Figure 6. (a) The basic principle of X-ray photoelectron spectroscopy and (b) concentric hemispherical analyzer used in XPS.

Atomic Force Microscopy (AFM)

The Atomic Force Microscope was invented to overcome a basic drawback of the Scanning Tunneling Microscopy (STM), that it can only image conductors and semiconducting surfaces.⁵⁹ The AFM has the advantage of imaging almost any type of surface, including polymers, ceramics, glass, and biological samples. The atomic force

microscope was invented in 1986. A sharp single crystal silicon tip is attached on a force-sensitive cantilever and scanned on the sample surfaces. A variety of tip-surface interactions can be measured by AFM, depending on the separation between the tip and the surface. While scanning the sample, the tip predominately experiences repulsive van der Waals force. When lifted above the surface, long range interactions dominate the interaction with tip, as seen in Figure 7.

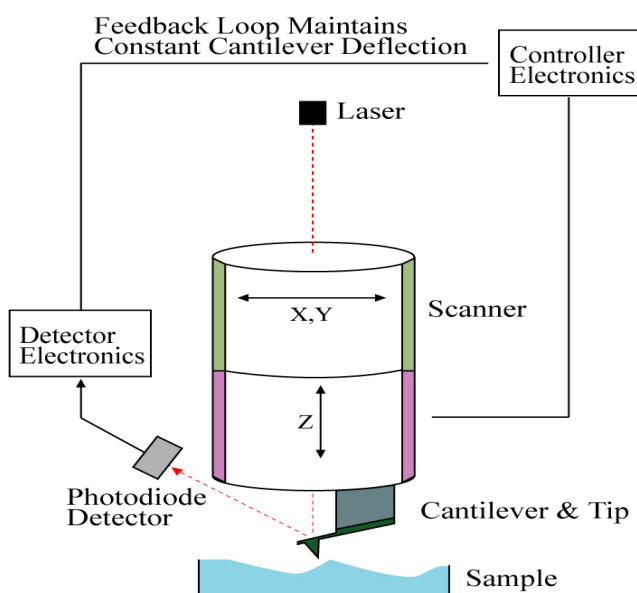


Figure 7. Schematic diagram of the AFM system in tapping mode.

The deflection of cantilever is monitored by the laser beam technique, as shown in Figure 7, in which a laser beam is reflected from the back of the cantilever to a segmented photodetector.

As a sample is scanned, the deflection of the beam occurs due to changes in the surface topography. AFM can be operated in three modes: tapping, contact, and

noncontact mode. In tapping mode, the cantilever is oscillated closer to the surface than in noncontact mode. Part of the oscillation extends into the repulsive regime, so the tip barely touches, or "taps," the surface. In the contact mode, a cantilever is scanned over the surface and the tip makes "physical contact" with the sample surface. It can obtain true atomic resolution images. The last operation mode of AFM is the noncontact mode. The tip does not contact the sample surface but oscillates above the sample surface during scanning. The change in amplitude or the phase of the oscillation is associated with the long-range attractive force sensed by the cantilever.

Transmission Electron Microscopy (TEM)

Transmission electron microscopy, as seen in Figure 8,^{60, 61} is a microscopy technique whereby a beam of electrons is transmitted through an ultra thin specimen, interacting with the specimen as they pass through. An image is formed from the interaction of the electrons transmitted through the specimen which is magnified and focused by an objective lens onto an imaging device, such as a fluorescent screen (as is common in most TEMs) or a layer of photographic film, or detected by a sensor, such as a charged couple device (CCD) camera. A scanning transmission electron microscope (STEM) is a type of transmission electron microscope. With it, the electrons pass through the specimen, but, as in scanning electron microscopy, the electron optics focus the beam into a narrow spot which is scanned over the sample in a raster. The rastering of the beam across the sample makes these microscopes suitable for analysis techniques such as mapping by energy dispersive x-ray (EDX) spectroscopy, electron energy loss spectroscopy (EELS), and annular dark-field imaging (ADF) and high-angle annular

CHAPTER IV

EXPERIMENTAL SETUP

To study the size dependent properties of clusters, several methods have been developed to afford the effective immobilization of metal particles on high surface area support materials. Unsuccessful attempts have been made using electron beam lithography to define regular arrays of Pt nanoparticles on silica.⁶ The attempt was unsuccessful in that the smallest particle size achieved was 20 ~ 30nm, which is an order of magnitude too large compared to the anomalous activity range of a few atoms ~ 10nm. Colloidal chemistry techniques have been employed to form uniform catalyst sizes down to a few nanometers, to create high throughput, and to enlarge the surface of particle loaded three dimensional support surfaces such as mesoporous materials.^{6,2} However, surfactant and other organic residues remain and may interfere with surface reactions. To remove contaminants, nanoparticles are cleansed by washing¹⁰ or thermal treatment with thermogravimetric analysis.^{7, 11} When using the impregnation method, a commonly used technique for the synthesis of heterogeneous catalysts, it is difficult to control particle size distribution, shape, and metal-support interaction as well as structure.^{6, 8} Due to these reasons, the use of size-selected, supported clusters is promising for the investigation of the size dependence of chemical reactions as well as sintering³ on small clusters such as gold,¹³ a crucial issue for fuel cells and for reducing cost.² Several groups have already developed a vacuum-based cluster source with a special mass filter for size-selected

nanoparticle deposition on different types of substrate. In order to develop size-selected clusters, a nanocluster source was developed based on magnetron sputtering to produce nanoparticles; a retarding field analyzer was used to measure cluster ion energy distribution and a magnetic sector mass filter was used to separate the cluster size according to mass to charge ratio. The following sections of this chapter discuss the design and parts of the cluster source chamber along with the retarding field analyzer (RFA), a small magnetic sector mass filter (MSMF), and the use of LabVIEW to control the mass flow controller (MFC), to collect ion currents from the RFA, and to obtain a pulse signal from the channeltron electron multiplier (CEM).

Matilda: Nanocluster System

Figure 9 depicts a final picture of the size-selected nanocluster source to understand the system easily.

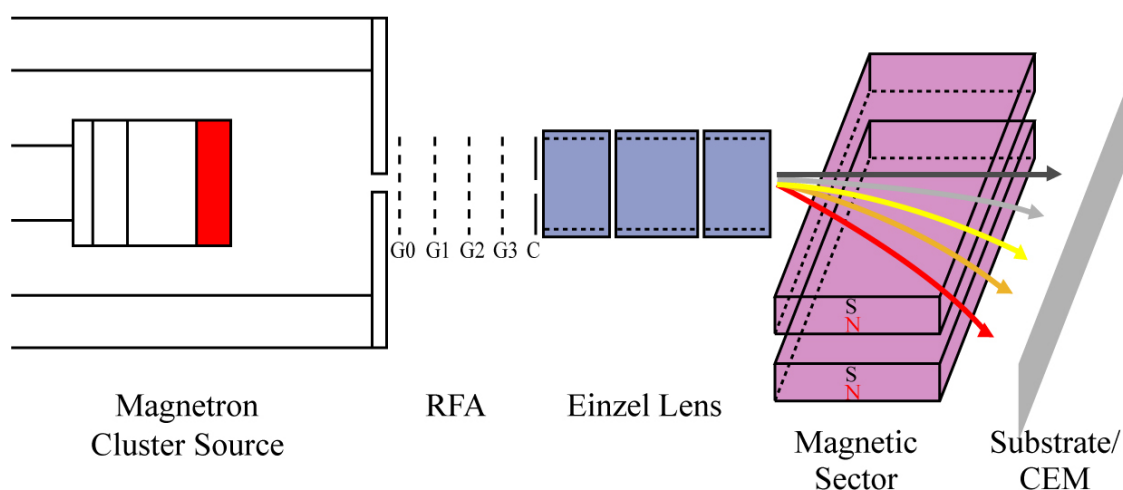


Figure 9. Schematic of the sections making up the complete size-selected nanocluster source system.

The whole system consists of four main parts. First, a cluster source produces nanoparticles. Second, a retarding field analyzer measures the ion current and its energy distribution to judge the soft or hard landing of clusters. Third, an Einzel lens focuses the beam introduced into the MSMF. Finally, the MSMF separates the negatively charged clusters according to mass to charge ratio, and the separated particles will be deposited on the substrate or detected by the channeltron electron multiplier. Figure 10 shows Matilda: nanocluster system (2nd version of nanocluster source). This system is different from the 1st version cluster source, which did not include a pumping port or an electrical feedthrough. Matilda is based on a 10" O.D. conflat "cross." The four ports on the "cross" have a nanocluster source, pump, accessory port, and a sample introduction load system. A vacuum is produced by a 400 L/s Osaka turbo pump while two MKS 10 sccm mass flow controllers (MKS Type M100B, Model number : M100B11CR1BV) are used to control the relative partial pressures of Ar and He in the aggregation tube of the cluster source during deposition, as seen in Figure 11. LabVIEW (Ver. 8.2) set the maximum voltage to fully open the valve of the mass flow controller, and then a Heliport precision potentiometer provided the final voltage for the mass flow controller to precisely control the gas flow rate. The cluster source consisted of a moveable AJA A310 series 1"-diameter magnetron sputtering gun enclosed in a water-cooled aggregation tube. The magnetron sputter gun employed DC power (Advanced Energy Industries, Inc., Model number : MDX 500) and is a conventional sputter gun having no Ar outlet skimmer on the shower head to produce plasma on the target surface; instead, a high voltage biased cathode (target) produces more sputtered atoms and makes dark space shield to direct the Ar over the target,^{51, 63} as shown in Figure 12(a).

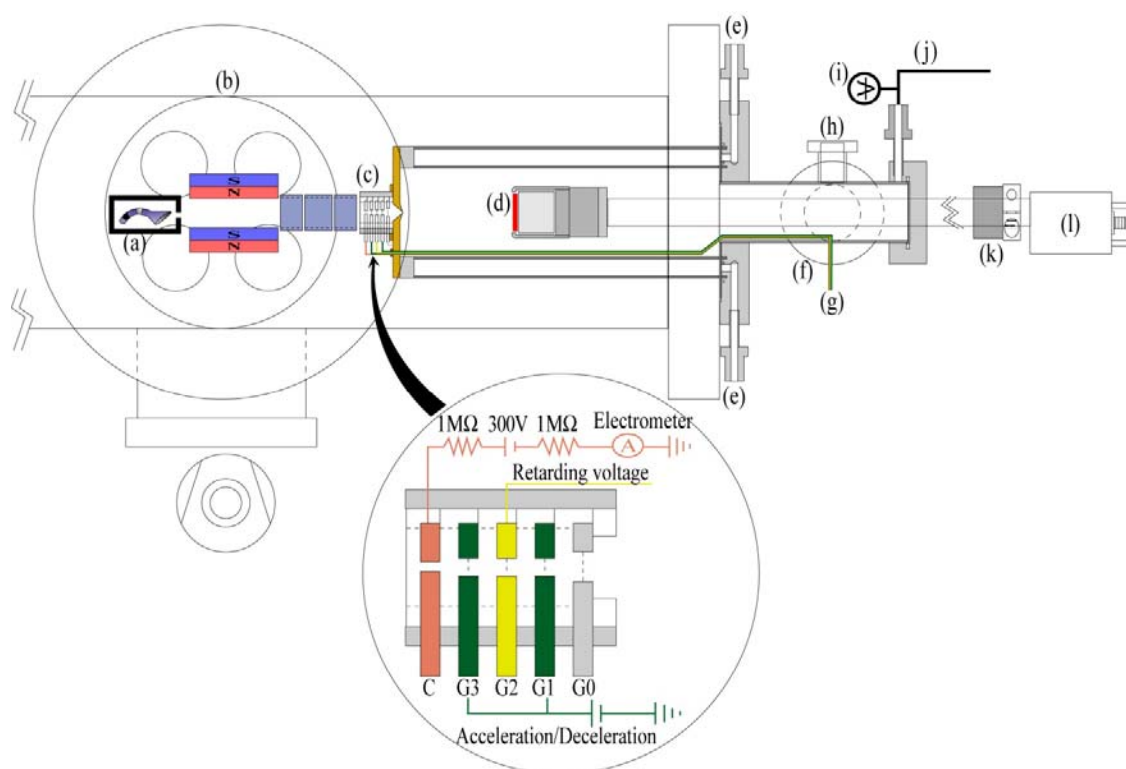


Figure 10. Schematic of the control system mounted on (a) sample holder/CEM, (b) accessory port including mass spectrometer, CEM holder, view port, and three electrical feedthroughs, (c) RFA, (d) sputter gun with target (red), (e) water in and out line, (f) electrical feedthrough port, (g) electrical lines for RFA grids, (h) pumping port for evacuating contaminant in aggregation tube, (i) convection gauge to measure pressure of aggregation tube, (j) gas mixture inlet line, (k) clamp for adjusting aggregation distance, and (l) electrical housing.

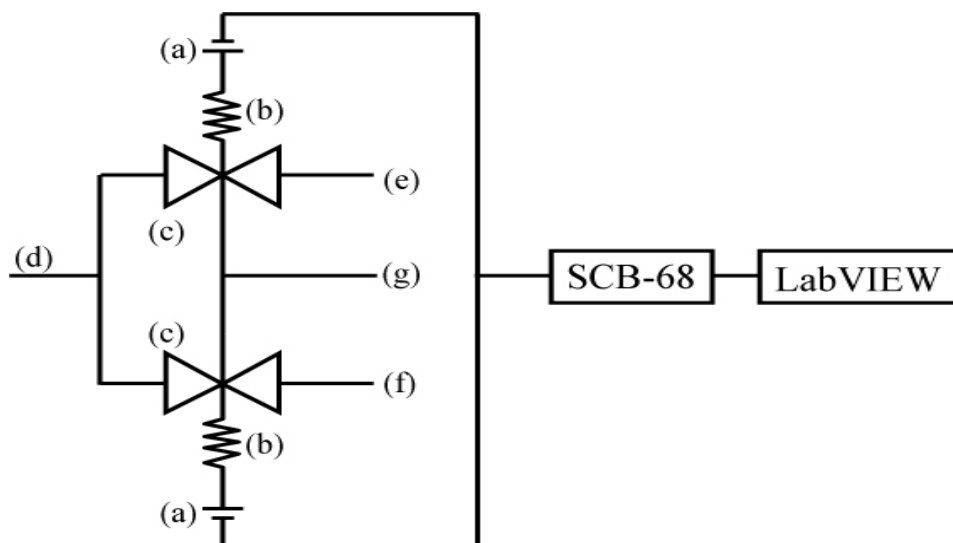


Figure 11. Schematic of gas line: (a) 0 ~ +5 VDC for flow signal output, (b) 0 ~ 10 K Ω Heliport 10 turn potentiometer for controlling flow signal output voltage, (c) mass flow controller, (d) gas mixture line to introduce into aggregation tube, (e) Ar inlet line, (f) He inlet line, and (g) ± 15 VDC power for mass flow controller. SCB-68 is a shielded I/O connector block for data communication between DAQ card and computer from National Instruments.

The AJA gun sputtered Ag reliably in 2 torr He in Figure 12(b). Unfortunately, there was no opportunity to test the semiconductor and insulator targets in a 5 torr He environment with an RF power supply.

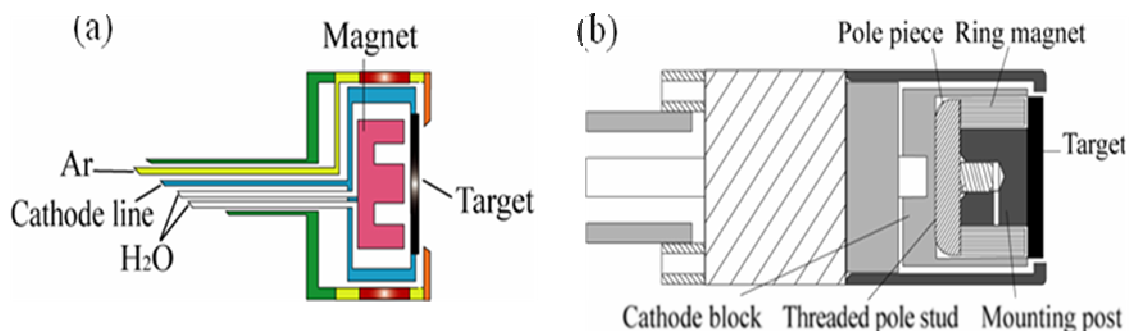


Figure 12. Comparison with (a) Haberland type, (b) conventional type of magnetron sputter gun.

The mixture of gases (Ar and He) was introduced from the back of the aggregation tube. The removable orifice used was made from oxygen-free copper and had a conical-shaped skimmer with a 0.08" inlet hole and 0.3" outlet hole for the cluster beam and also served as a holder for the RFA. The aggregation distance from the target to the inlet hole of the conical shaped skimmer could be varied up to 8". The cluster source had a pumping port to evacuate all of the contaminant in the aggregation tube, and a high voltage (5.0 kV) electrical feedthrough provided voltage to each grid of the RFA. During the sputtering process, a plasma discharge ablated material from the sputtering target. The sputtered material left the target with a kinetic energy of the order of a few electron volts. As the ions diffused through the high pressure region in the aggregation tube, they merged to form clusters of 100s to 1000s of atoms. These nanoclusters retained a positive or negative charge of one electron or were neutral as they left the aggregation tube. If a metal such as Ag, Cu, or Al was used, the material would leave the target as ions. The approximate percent of ionization depended on the materials used, such as 60%

~ 80% for Al and 20% ~ 60% for Cu.⁶³ Normally, the cluster yield of negatively charged clusters is less than the number of positively charged clusters.⁵⁴ There are many cluster charge transfer mechanisms aimed at producing positive, negative, and neutral clusters, a few of which have been explained in detail.⁴⁸ For positively charged clusters, a positively charged ion may collide with neutral clusters.



The Ar^+ transferred its charge to clusters because Ar^+ was in the majority near the target.



However, the reverse process was impossible because the ionization energy (15.8 eV) of Ar is much higher than that of metals, such as silver (7.6 eV). Penning ionization by an electronically excited Ar is another possible way to produce positively charged clusters especially in the presence of He. The asterisk in the following equation indicates the electronic excitation.



For negatively charged clusters, the electrons may collide with clusters due to the high electron density in plasma.



A loss mechanism of positively charged clusters is the collision between electrons and a charged cluster.



An RFA was constructed to determine the distribution of nanocluster ion energies leaving the aggregation tube. During cluster deposition, the pressure range in the aggregation

tube was from 70.0mtorr to 1torr, as measured by a convection gauge (Terranova-960), and 10^{-5} torr in the main chamber. To control the cluster source, the LabVIEW program collected ion currents by sweeping the retarding voltage on the RFA. Many Ar^+ and electron can exhaust from the cluster source, hit the collector, and mislead the actual cluster current if the RFA measures positively charged clusters. Also Ar and He have an unstable state for negative ion. For this reason, the ion current was obtained from negatively charged silver clusters in this experiment,⁶³ although the number of positively charged cluster was higher than the number of negatively charged clusters.

Retarding Field Analyzer

A schematic of RFA shown in Figure 13 serves as a high pass filter allowing only ions having a higher kinetic energy than the cluster charge times the retarding voltage to pass.^{64, 65} The grid plates are made from 0.04" thick titanium plates and are shielded by a cylindrical stainless steel tube that is electrically grounded. The grids are made from electroformed copper mesh with an 80% transmission (Precision Eforming LLC, Part number: MC-18) which are spot-welded on to the grid plates and isolated by ceramic spacers (McMaster-carr, Part number: 8489K131). The size of the hole in each grid is 0.16" for G0, 0.23" for G1 through G3, and 0.1" for the collector. G0 is always grounded. G1 and G3 accelerate and decelerate the ions while G2 sweeps the voltage range to find the ion energy distribution.

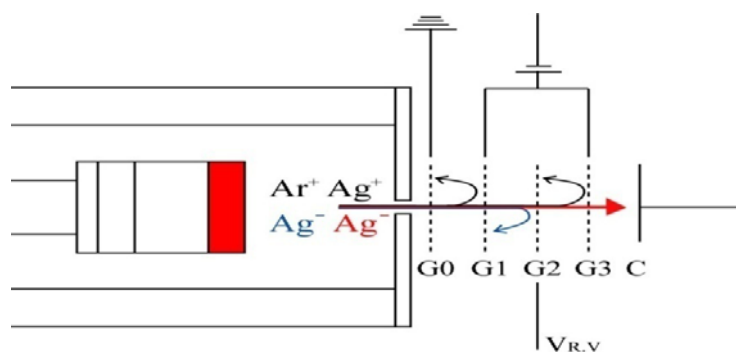


Figure 13. Schematic of the basic principle of retarding field analyzer.

The configuration of each grid depends on the experimental conditions. For hard landing of clusters, a high voltage power of 5kV will be applied to the grids to accelerate the clusters. If the kinetic energy of an ion is higher than the retarding voltage, it will pass G2. The collector, which is connected to an electrical box having a 300V battery (Enerziger, Part number: Eveready 493) between resistors of 1.0 M Ω , maintains a constant positive potential to collect the ion energy distribution (using a Keithley 614 electrometer) of negatively charged particles striking a specific place on the collector. In the 1st version of the RFA, the diameter of the holes in the mesh was larger than that of the 2nd version. In the 2nd version, a copper mesh was used to prevent disturbance from the magnetic field from the MSMF instead of the nickel mesh used in the 1st version. The two versions are shown as photographs while the grids are seen in the insets of Figure 14.

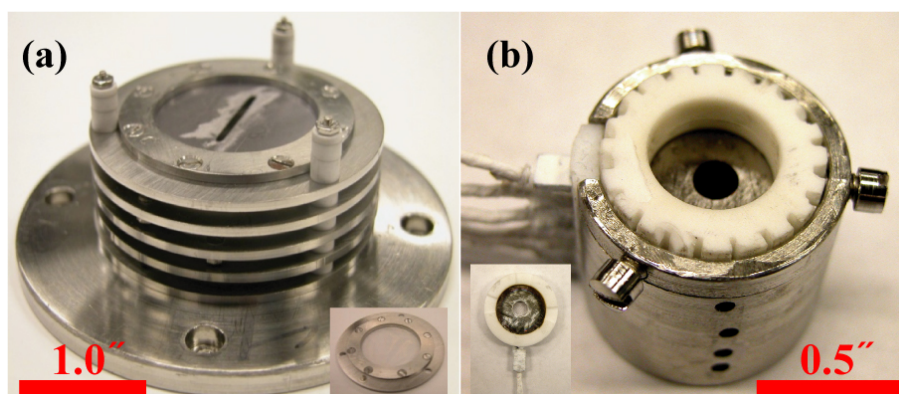


Figure 14. (a) 1st version and (b) 2nd version of RFA, and their grids shown as insets. The holes on cover of (b) vent the gas mixture to prevent a short circuit at high voltage.

Three-Element Lenses

The Einzel lens is used to focus the charged clusters in flight by manipulating the electric field in the path of the charged clusters. It consists of a three-element electrode in which the outer electrodes have the same potential. The number of electrode depends on the experimental environment. Beam focusing is achieved by changing the potential on the middle electrode. The kinetic energy of the beam must not be changed while it is focused. Figure 15(a) and (d) exemplify the focusing effect with different electric fields on the middle electrode in an Einzel lens using trajectories of charged clusters calculated using the ion optics simulation program SIMION.⁶⁶ Figure 15(b) and (c) are different views of Figure 15(a). The focal point is changed in Figure 15(c) and (d) when a different electric field is applied to the middle electrode.

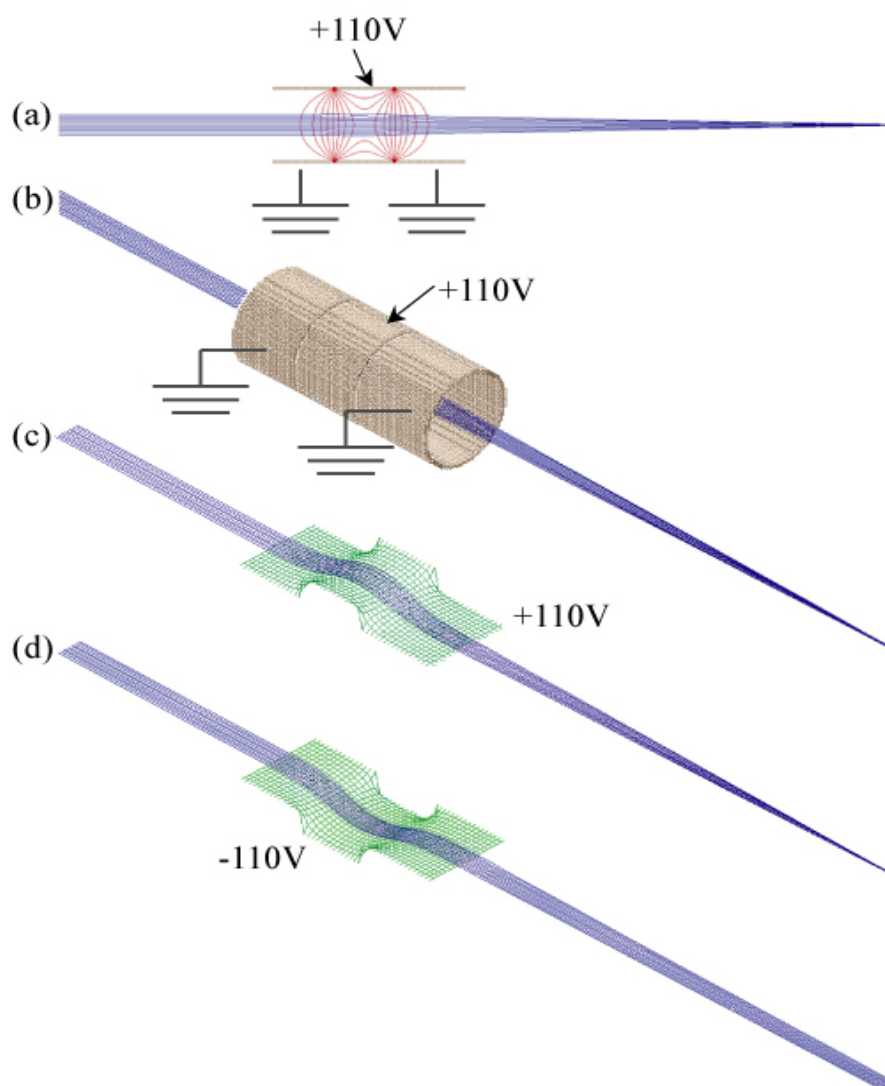


Figure 15. SIMION simulation of an Einzel lens. (a) cross sectional view of an Einzel lens with electric potential line (red line). Two electrodes are set to ground potential, the middle electrode to +110V. (b) three-dimensional view of the three electrodes and the particle beam. (c) and (d) show focusing effect in a different field of middle electrode. Roll outward shows positive and roll inward indicates negative potential.

Figure 16 shows the Einzel lens used for Matilda. Three cylindrical lenses made of aluminum were held using a cylindrical piece of ceramic (McMaster-carr, Part number:

8489K81). The inner diameter of the lenses was 0.5" and the thickness of the wall was 0.1". The lenses were mounted on ceramic rods 0.2" in diameter that insulated the lenses from one another and from a grounded mounting block and lens holder. The gap between the electrodes was 0.025".



Figure 16. Picture of the three-element lenses used for Matilda.

Magnetic Sector Mass Filter for Mass Separation

According to the principle underlying the MSMF separation of masses in Figure 17, the radius of ion trajectory is proportional to the root of the particle's mass, m , and V , which is the retarding voltage provided by the RFA and is inversely proportional to the magnetic field strength. e is the charge on the mass selected ion.⁶⁷

$$R = \frac{1}{B} \sqrt{\frac{2mV}{e}} \quad (8)$$

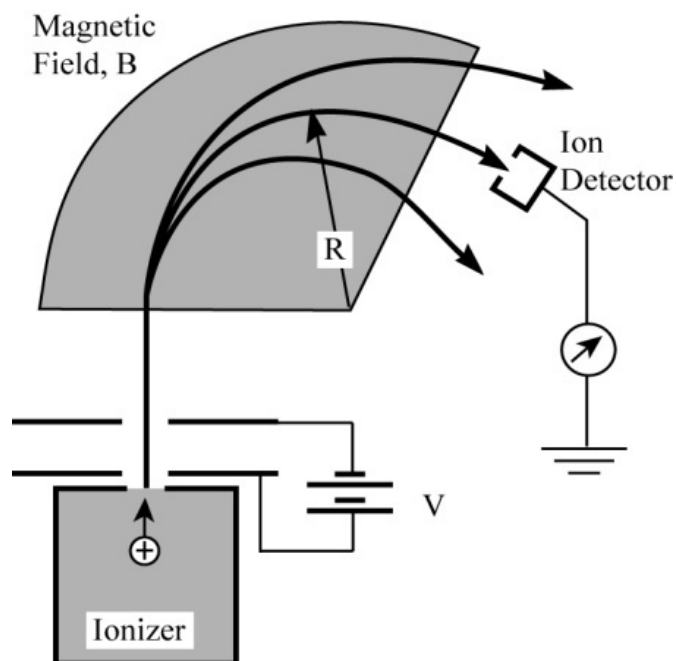


Figure 17. Schematic of MSMF for mass separation.

In the experiment, two neodymium (NdFeB) block magnets (Kjmagnetics, Inc., Part number: BZX0Y08) were used for size separation. Figure 18 shows a picture of the MSMF, which is enclosed by soft iron (a) to confine the magnetic field. Each magnet was 4" width \times 2" long \times 0.5" thick. The gap between the magnets was 0.5". Aluminum rod and bolts and nuts were used to adjust the height of the gap with the beam line. Three pink insulators were used to separate the electrical grounds from each other.

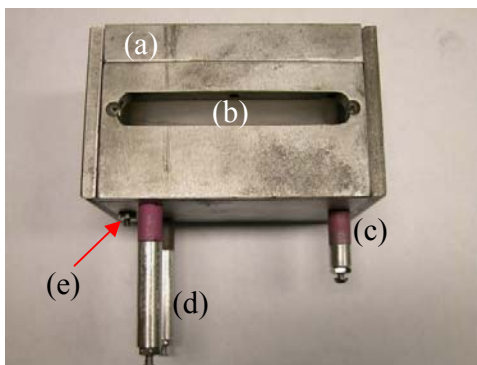


Figure 18. Picture of MSMF: (a) cover, (b) neodymium block, (c) pink colored insulator, (d) supporter with bolt and nut, and (e) electrical connector.

Detection Methods of Charged Particle

For charged particle detection, there are two widely used detection methods:

Faraday cup and CEM (see Figure 19). A Faraday cup is a conductive metal cup designed to collect charged particles in a vacuum. A Faraday cup acts as a collector for electrons from an electron beam. In this case, electrons simply hit the metal plate or cup and a current is produced. Faraday cups are not as sensitive as electron multiplier detectors but are highly regarded for accuracy because of the direct relation between the measured current and the number of ions. The Faraday cup was used as a collector for Matilda (see Figure 10.)

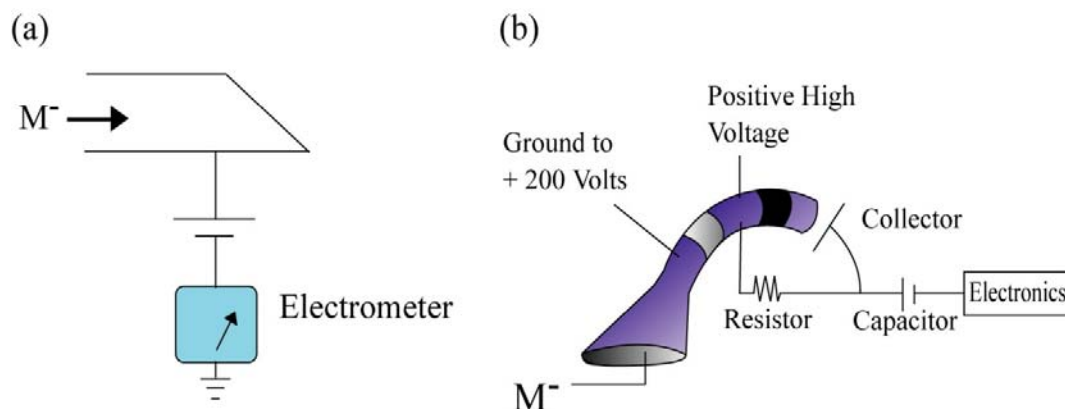


Figure 19. Schematics of (a) Faraday cup and (b) CEM for detection of negatively charged ions.

A CEM is a glass tube with semiconducting inner surfaces that multiply incident particles. Incident particles must have an excess energy to ensure efficient secondary electron emission because semiconducting inner surfaces are made of materials with a high work function to inhibit thermionic emission that would increase noise at the multiplier output. On the other hand, when working with lower energy particles, it is necessary to provide an acceleration stage at the multiplier input. For positive ions, the input is generally at a negative potential of 1000 volts; output is normally grounded. For detection of negative ions, the input is normally grounded or at some positive potential, and the output is at a high positive voltage.^{68, 69} Figure 20 shows the current CEM setup with a discriminator to obtain the charged cluster signals.

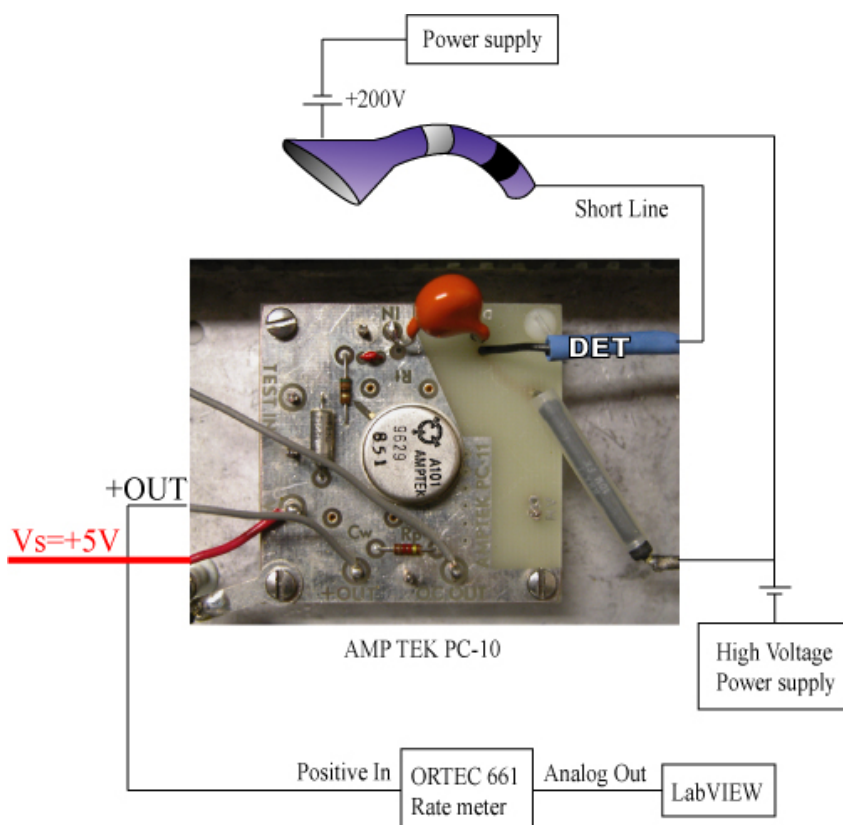


Figure 20. The circuit of CEM with discriminator (AMPTEK A101 and PC-10 board).

For the detection of negative charged particles in Matilda, CEM (Burle Model No: 4774) was used and installed downstream of the MSMF. An AMPTEK A101 is used for the preamplifier and for removing noise from the discriminator. At the multiplier input, the potential (200V) repels positively charged particles and only accepts negatively charged particles. They were accelerated by high voltage (2.5kV), which achieved the saturated signal. The PC-10 board sent the signal to the ORTEC 661 ratemeter, which can produce an analog signal in the 0-10V range.

Modification of Nanocluster Source

After testing the 1st version of the nanocluster source, an electrical feedthrough, a pumping port, and a shortened aggregation tube length was added. The schematics of the 1st and 2nd version of the cluster source are shown in Appendices A and B. During deposition of the 1st version of the cluster source, target material was deposited on the side wall of the aggregation tube, as shown in Figure 21(a). Next, the pumping port was added behind the aggregation tube to easily evacuate all contaminants, as shown in Figure 21(b). The electrical lines for the RFA were cumbersome to connect when the cluster source was dismantled from the chamber. All electrical lines ran through the aggregation tube and were connected with feedthrough connectors (Ceramtec, Part number: 9791-08-W) in the aperture, shown in Figure 21(c) and (d). The 1st cluster source produced particles in the 20 to 80nm range at a 4" aggregation distance. A major goal for catalysis is to produce particle sizes from atomic scale to 10nm. Therefore, the aggregation tube length was shortened from 10" to 8.5", as shown in Appendix A.

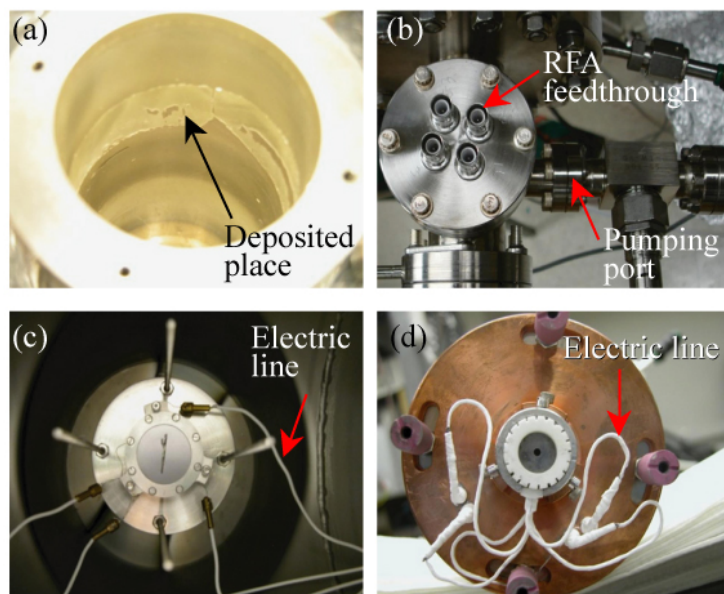


Figure 21. The pictures of the modification of the 1st version cluster source. (a) Deposited place after deposition, (b) pumping port and feedthrough for RFA, and electrical line with (c) 1st and (d) 2nd versions of the RFA.

CHAPTER V

PERFORMANCE OF MATILDA

The range of cluster sizes produced can be varied by changing parameters such as gas pressure, aggregation distance, and sputter power. The pressures of Ar and He are most effective for controlling cluster size. If calculated correctly, these parameters will produce clusters which have a proper range of cluster size, from a few atoms to a few thousand atoms per cluster, depending on the target material.⁵¹ Figure 22 shows the High angle annual dark field (HAADF) image and the spectra from XPS and EDX analysis to confirm the deposited materials. Binding energy of Ag is lower than that of pure silver (B.E:368.4eV) due to contaminations of breaking vacuum and deposition. Blank data of EDX analysis in Figure 22 has low intensity than that of Ag on C-TEM grid because blank data was collected at low magnification. Particle size distribution was measured by NIS-Element BR (Version 2.20, Nikon Instruments Inc.) from the TEM images and the Nanoscope (Version 5.12r4, Digital Instruments). Experiments were performed with RFA.

Pressure Ratio of Helium to Argon

First, the Ar flow rate was varied to find the conditions which could produce small clusters. Then, He was increased to obtain the desired cluster size. Changing the ratio of He to Ar pressure has a marked influence on the mean particle size, as shown by TEM in Figure 23. At a 14sccm Ar flow rate, the range of particle size was 20 ~ 80nm

(not shown) and was 1.5 ~ 8nm at 0.4sccm Ar, which is the minimum flow rate for sputtering. At a zero pressure ratio, the pressure on the aggregation tube was 70mtorr. Changing flow rate conditions generated a wide range of cluster sizes. The mean size of the particles was dramatically decreased by increasing the He pressure in the gas mixture. Clusters of 0.5 ~ 4.0nm in size were produced when the pressure ratio was 9.5. The mean size of these clusters was 1.6nm. The effect of He gas pressure is the most important factor for producing small particles. Figure 24 shows that the He flow rate not only decreased the particle size distribution, but also decreased the width of the distribution peak. At a low pressure ratio, the size distribution was broad, from small clusters to large clusters. As large clusters deposited on TEM grid start to agglomerate each other during long deposition time and they become peanut shape. Most of large clusters are polycrystalline. For small clusters which are less than 2nm in size, high resolution TEM hardly provides a clear image. In this range of cluster size clusters have single crystalline and polycrystalline. The crystalline effect of cluster for chemical activity wasn't tested.

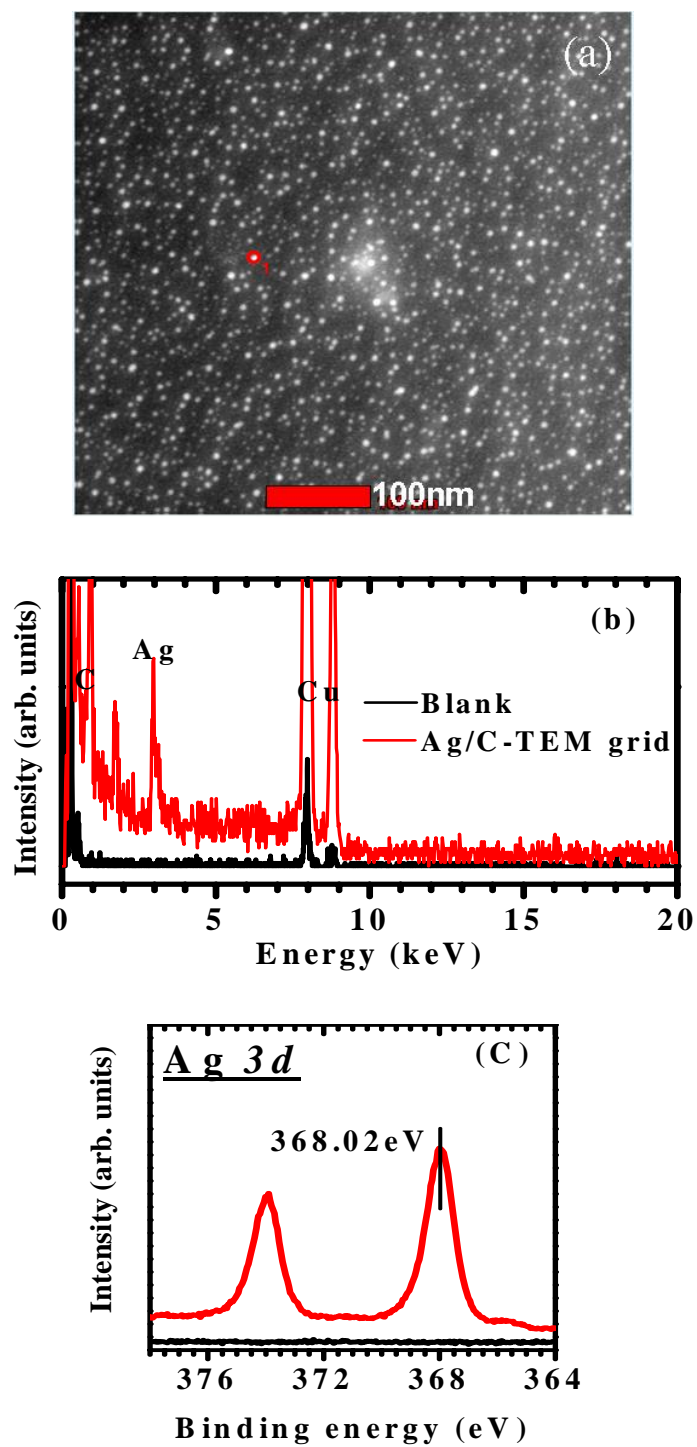


Figure 22. (a) HAADF image, (b) EDX analysis of Ag on c-TEM grid in red circle area of (a), and (c) XPS spectra of Ag/Si. Red lines are for Ag and black lines are for substrate.

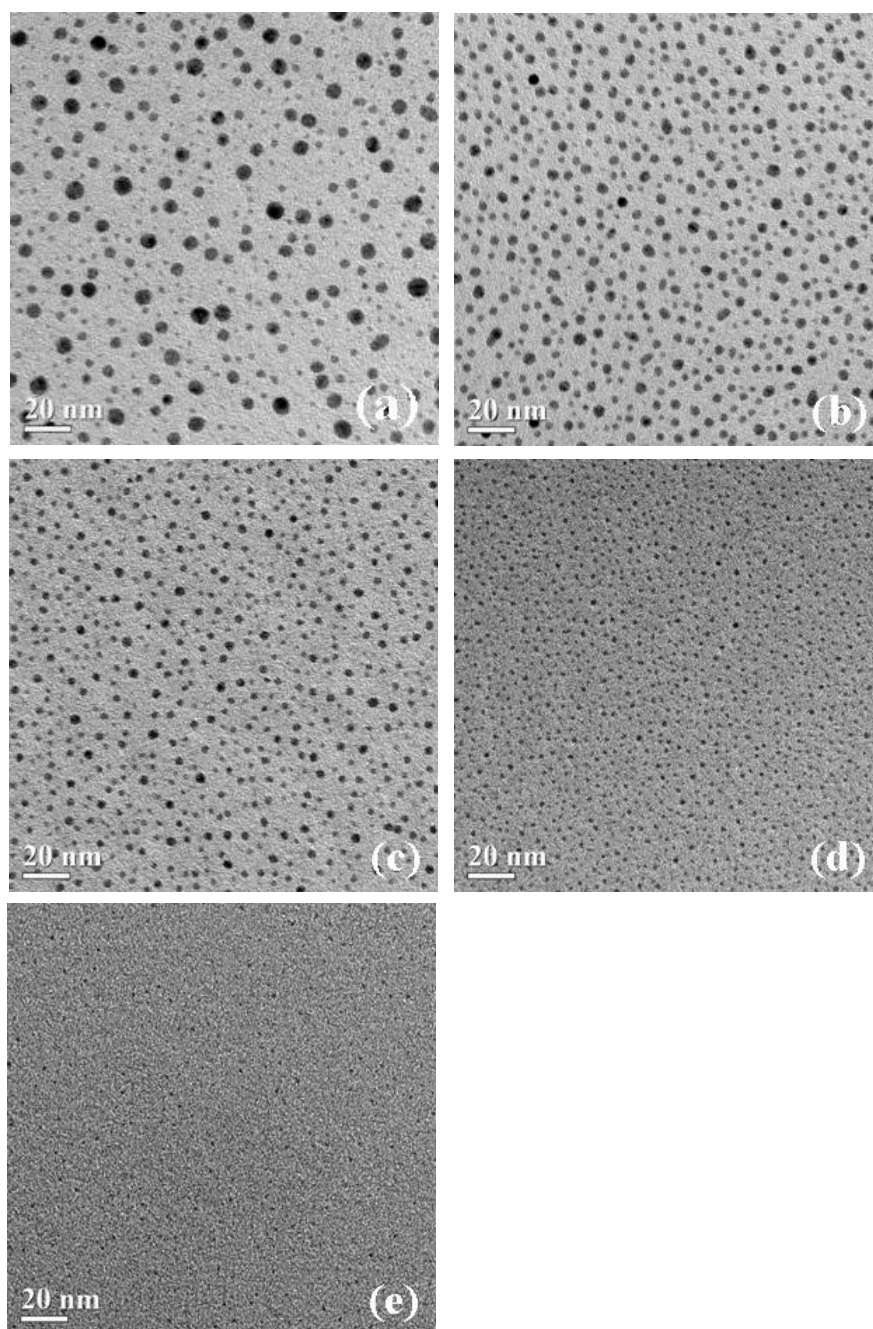


Figure 23. TEM images of Ag on c-coated grid with RFA as pressure ratio of He to Ar (a) 0, (b) 2.5 (c) 4.5, (d) 6, and (e) 9.5 at 2" aggregation distance and 20 minutes deposition.

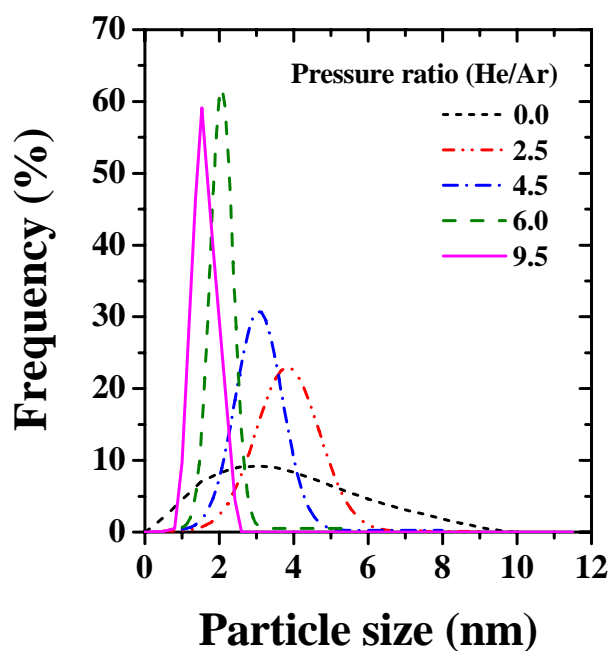


Figure 24. Particle size distribution from Fig. 23.

Two growth modes; two body (cluster collision) and three body collision (two sputtered atoms collide with He, removing the excess kinetic energy of the sputtered atoms), simultaneously occur in this condition. At a high pressure ratio, three body collision dominates to produce small clusters.⁵¹ Thus, He promotes the growth of small clusters from a few atoms at a high pressure ratio. A higher cluster current was obtained with a decreasing pressure ratio as shown in Figure 25.

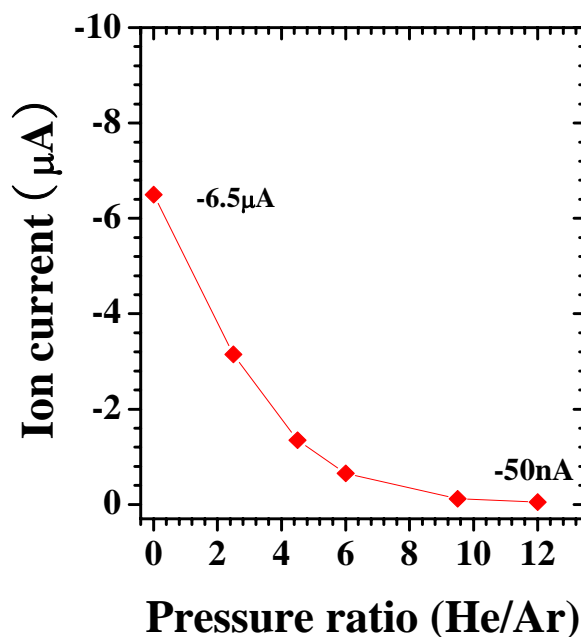


Figure 25. Saturation ion current vs. pressure ratio (He/Ar) at 20 watt sputter power (Pressure ratio = 0 (only 0.4 sccm of Ar)).

This means that charged clusters left the skimmer more efficiently, with a higher partial pressure of Ar and a low partial pressure of He. Only a small amount of clusters were skimmed out, because most of the sputtered clusters had a short mean free path and were deposited on the aggregation tube wall. For this reason, particles are not seen at a pressure ratio of 12; however, an ion current is detectable as the increasing He flow decreases the ion current from $-6.5\mu\text{A}$ to -50nA as seen in Figure 25. The Ag peak on the TEM grid was not seen using XPS at a pressure ratio of 12.

Ion Energy Distribution

The sputter gun power supply was regulated, that is, both the voltage and current were increased in correct proportion to maintain a constant power during the deposition. This ensured that the flux of atoms leaving the source remained constant. Changing the target voltage had a direct influence on the measured ion energy distribution curves. Ion energy distribution is presented as dI/dV , as current decreased when the retarding voltage was increased. The ion energy distribution slightly increased with increasing sputter power, as shown in Figure 26. As the ions diffused through the aggregation region, they lost some of their kinetic energy. Since the sputter target was moveable in the cluster source, the length of the aggregation region could be changed. The ion energy distribution decreased with increasing aggregation distance; the number of clusters decreased by collision and deposition in the aggregation tube, as shown in Figure 27. Thus, the mean particle size increased beyond 20nm at 4" and up to 80nm at 6" aggregation distance. Also, the number of particles decreased with increasing aggregation distance. The ion energy distribution decreased with increasing He flow rates due to more collisions as shown in Figure 28. The cluster landing energy could be predicted by the ion energy distribution, and would determine if the clusters had been deformed or not during deposition. Figure 29 shows the ion energy distributions of different acceleration voltages at a zero pressure ratio and at 0.4 sccm Ar with 20 watt sputter power and a 2" aggregation distance. The peaks widen with an increasing acceleration voltage, which may allow the separation of ions with mass occupying high energy regions and high mass occupying low energy regions. As the acceleration voltage was increased, the ion energy distribution started to stretch out on the positive side of the retarding voltage. However,

the reason for this was unclear. The degree of stretching depended on the acceleration voltage.

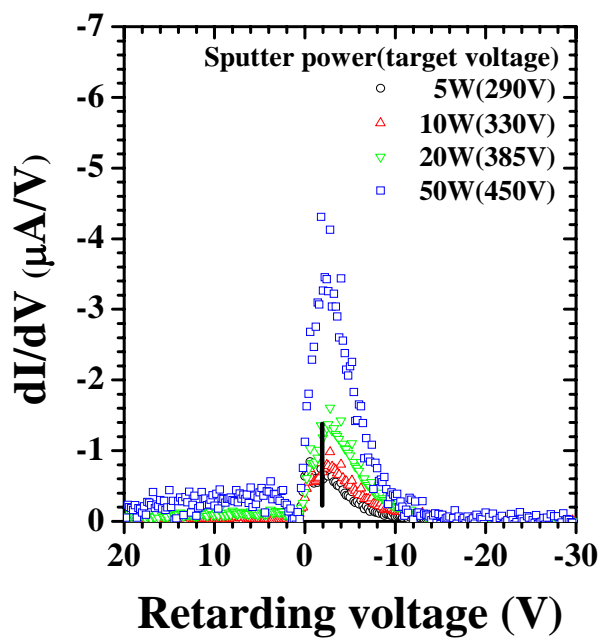


Figure 26. Ion energy distribution with different sputter power at 2" aggregation distance and 0.4 sccm Ar flow rate (solid line is the indicator of the center of ion energy distribution).

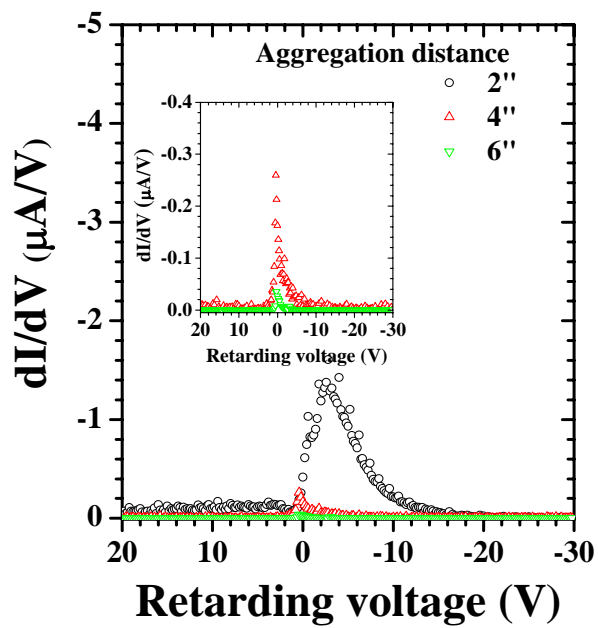


Figure 27. Ion energy distribution with different aggregation distances at 20 watt sputter power and a 0.4sccm Ar flow rate.

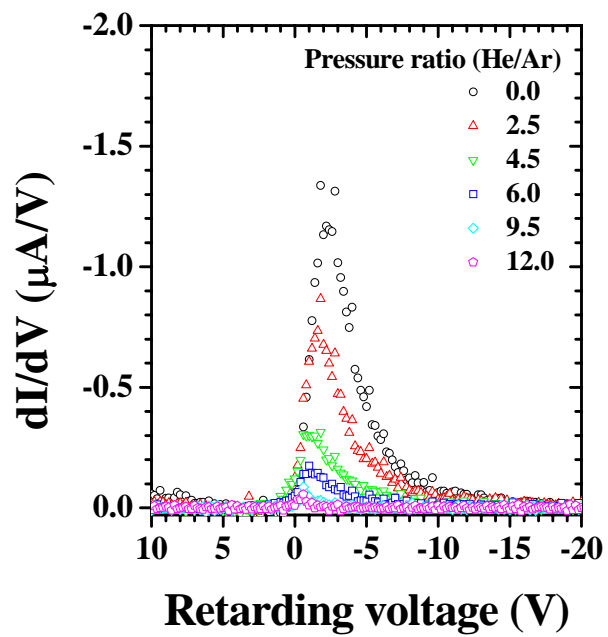


Figure 28. Ion energy distribution with different He flow rates at 0.4 sccm Ar with 20watt sputter power and 2" aggregation distance.

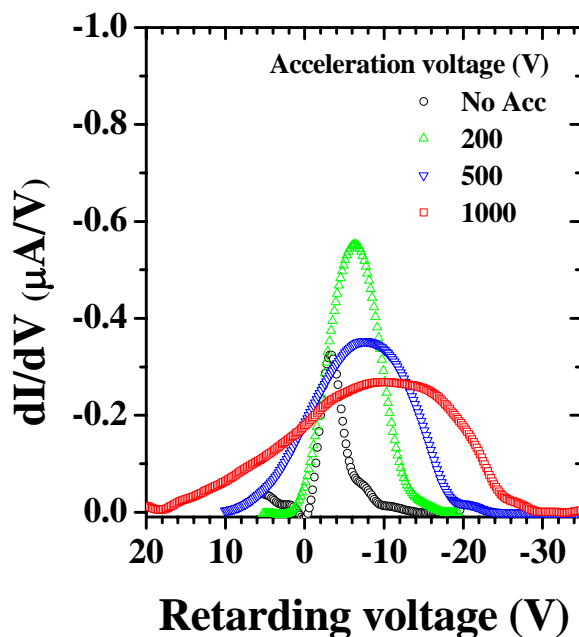


Figure 29. Ion energy distribution with different acceleration voltages at a zero pressure ratio and at 0.4 sccm Ar with 20 watt sputter power and 2" aggregation distance. G1 and G2 are applied with an acceleration voltage and G3 is the retarding grid.

To understand this phenomena, a retarding test with particle size distribution may be required. Voltage leaking occurred at a high acceleration voltage (2.0kV), perhaps caused by the ionization of the gas mixture. Maximum cluster landing energy, which is the maximum ion energy (Figure 26) per minimum cluster size (Figures 23 and 24), was calculated as reported in Appendix H. At a zero pressure ratio, in Figure 30, the maximum landing energy was $\sim 2.9\text{eV/atom}$, which was higher than in the soft landing condition ($\leq 0.1\text{eV/atom}$),^{30, 70} because there was a single negatively charged ion and a spherical particle. Most clusters will be soft landed during deposition. To accurately verify landing energy, further analysis with a scanning tunneling microscope would be needed to acquire three dimensional images of the clusters.

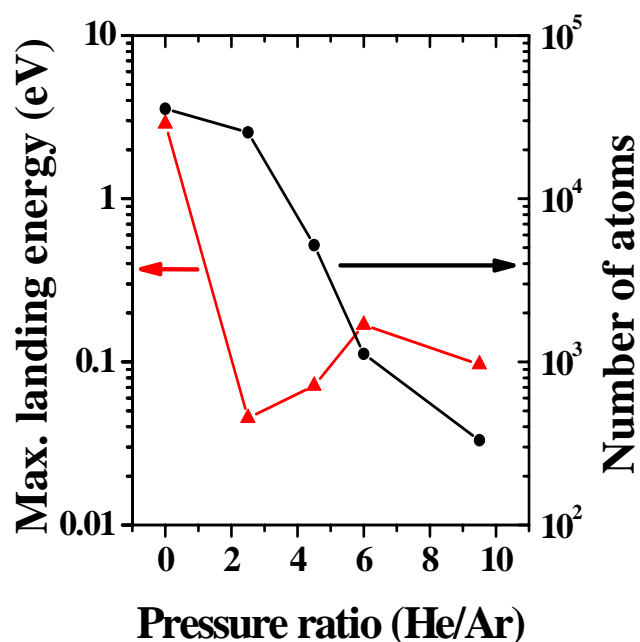


Figure 30. Maximum cluster landing energy at different pressure ratios (He/Ar).

Ion Optics for Retarding Field Analyzer

The RFA was designed to suppress the beam expansion, to some extent, after skimming. Cluster beam size was measured by the mark on the colloidal graphite-coated Cu plate used as a collector grid without and with RFA after deposition. Without the RFA, the beam size was about 0.74". The size of the cluster beam was about 0.18" in diameter at the collector grids and 0.28" from the collector grid of the RFA. Beam intensity was ~ - 1206.0 μ A/in² at a zero pressure ratio. Beam intensity decreased with increasing pressure ratios due to the decreasing number of ions from the cluster source, shown in Figure 25. Figure 31(a) shows the schematic of the RFA by SIMION 3D coding and the magnification of the copper mesh. A 100% transparent ideal grid was used during the simulation without ceramic spacers due to the reduction of beam transmission.⁷¹ Each of

the RFA could be biased with negative voltages for the deceleration of particles, or a positive voltage could be applied for the acceleration of negative ions, and with opposite voltages on the grids to prevent the deposition of Ar⁺ ions and positively charged silver clusters on the substrate. Neutral clusters cannot be removed in this experiment. Only ions having a higher energy than the retarding voltage at the G2 grid can pass and are deposited on the substrate in Figure 31(b) and (c). Some ions evacuated from the skimmer cannot pass the RFA by the initial beam position; however, the kinetic energy of the beam is higher than the retarding voltage in Figure 31(b) and (c). The ions represented by the red and green lines are different in their incoming position for the RFA, but neither can pass the retarding grid. The incoming position of the ion may also influence the ion current. The ion current depends on the number of negatively charged particle hitting the collector. It increases with an increasing acceleration voltage to promote the hitting rate of ions and decreases with increasing retarding voltage to prevent passing ions at the retarding grid, shown in Figure 32(a). The number of particles from Figures 33 and 34 follows the same trend as the ion current in Figure 32(a).

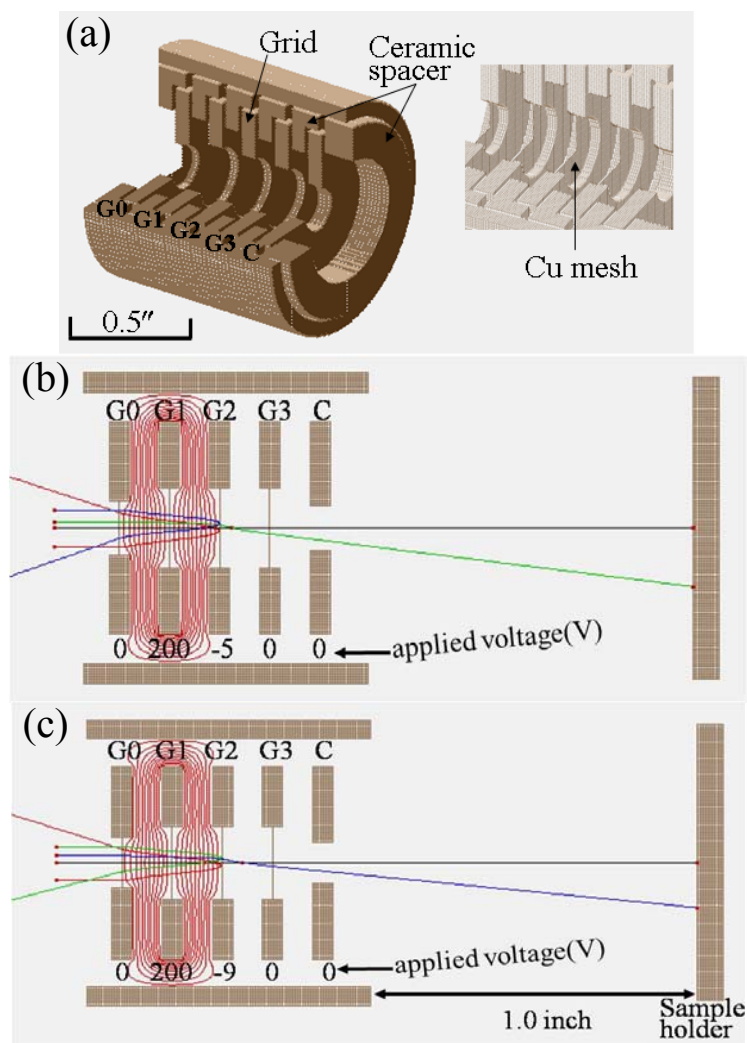


Figure 31. (a) Five grids and ceramic spacer in retarding field analyzer with magnification of 100% transparency copper mesh (real grids have 80% transparency) of each grid. (b) Beam trajectories for retarding voltage (-5V) at G2 (200V). Initial K.E of black and red line = 5eV, and other lines have 6eV. (c) Beam trajectories for retarding voltage (-9V) at G2 (200V). Initial K.E of black and red line = 9eV and other lines have 10eV. Sample holder is grounded.

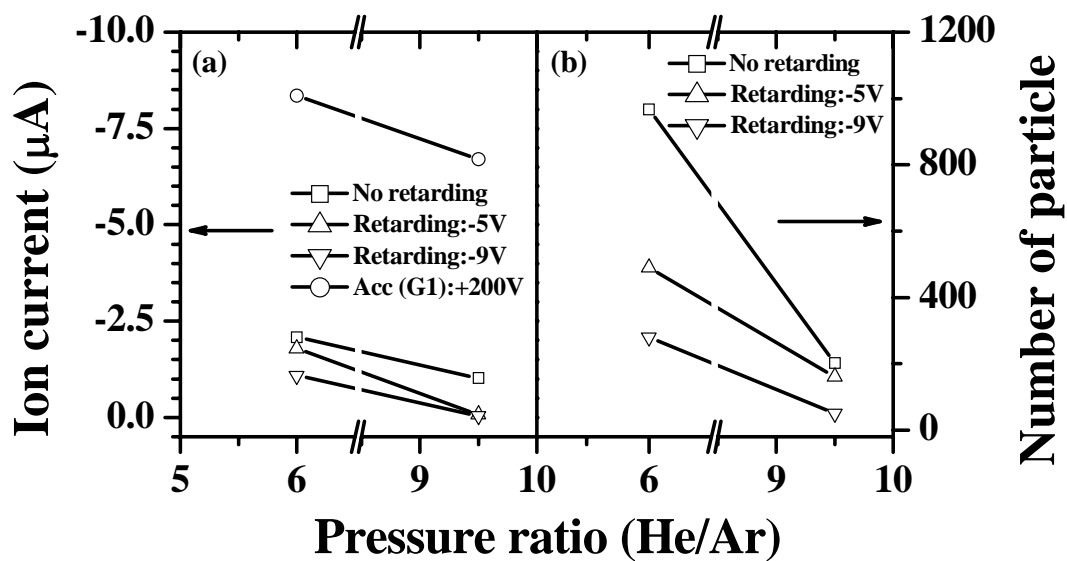


Figure 32. (a) Ion current and (b) number of particles collected from TEM images

To verify the cluster ion energy for large and small clusters at 6.0 and 9.5 pressure ratios in Figures 33 and 34, the retarding grid was applied with -5 and -9V to compare with a control condition with no retarding. The results did not clearly verify the retarding effect because both large and small cluster existed in the same images. Also, size distribution had no distinct trend in Figure 33, although Figure 34 shows a trend in size distribution.

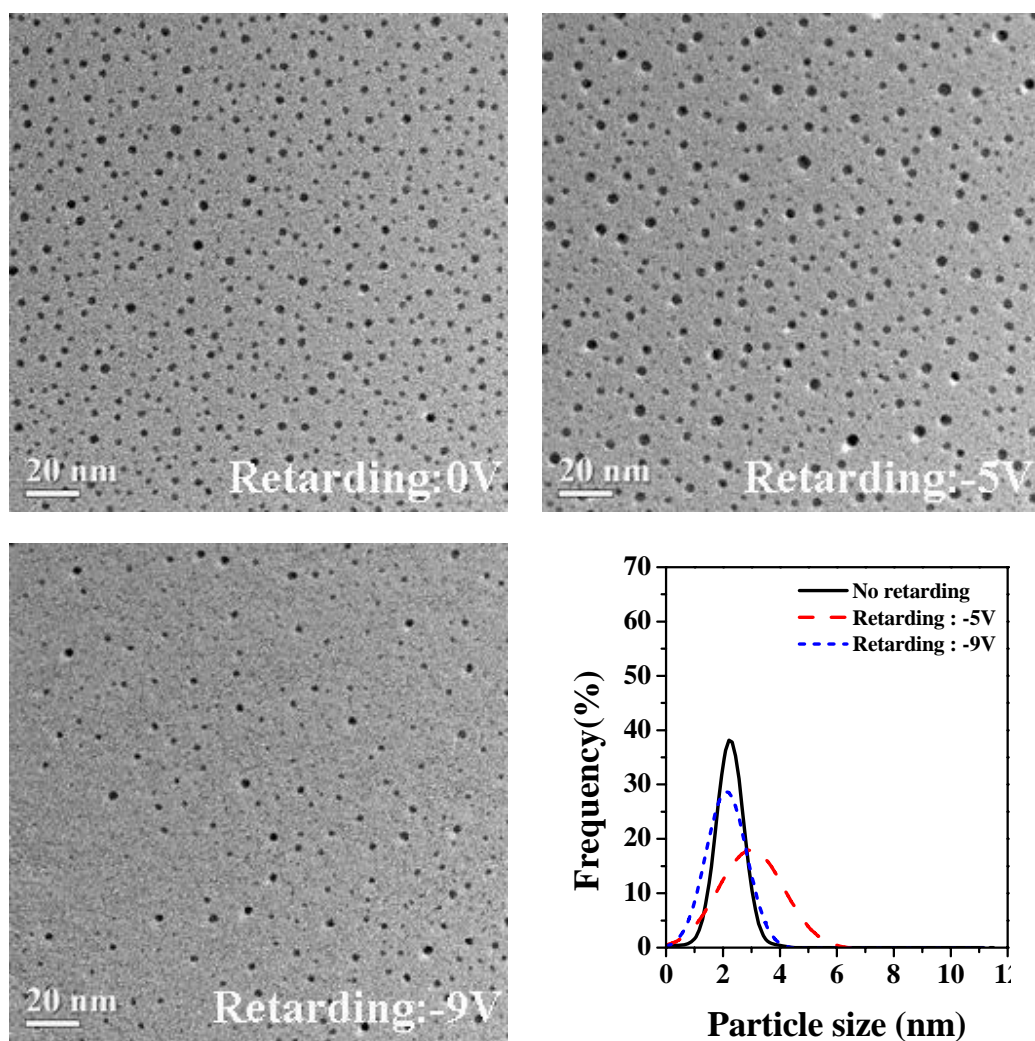


Figure 33. TEM image and particle size distribution at -5V of retarding voltage with a 6.0 pressure ratio at $G1=+200V$. Other grids and sample holder are grounded.

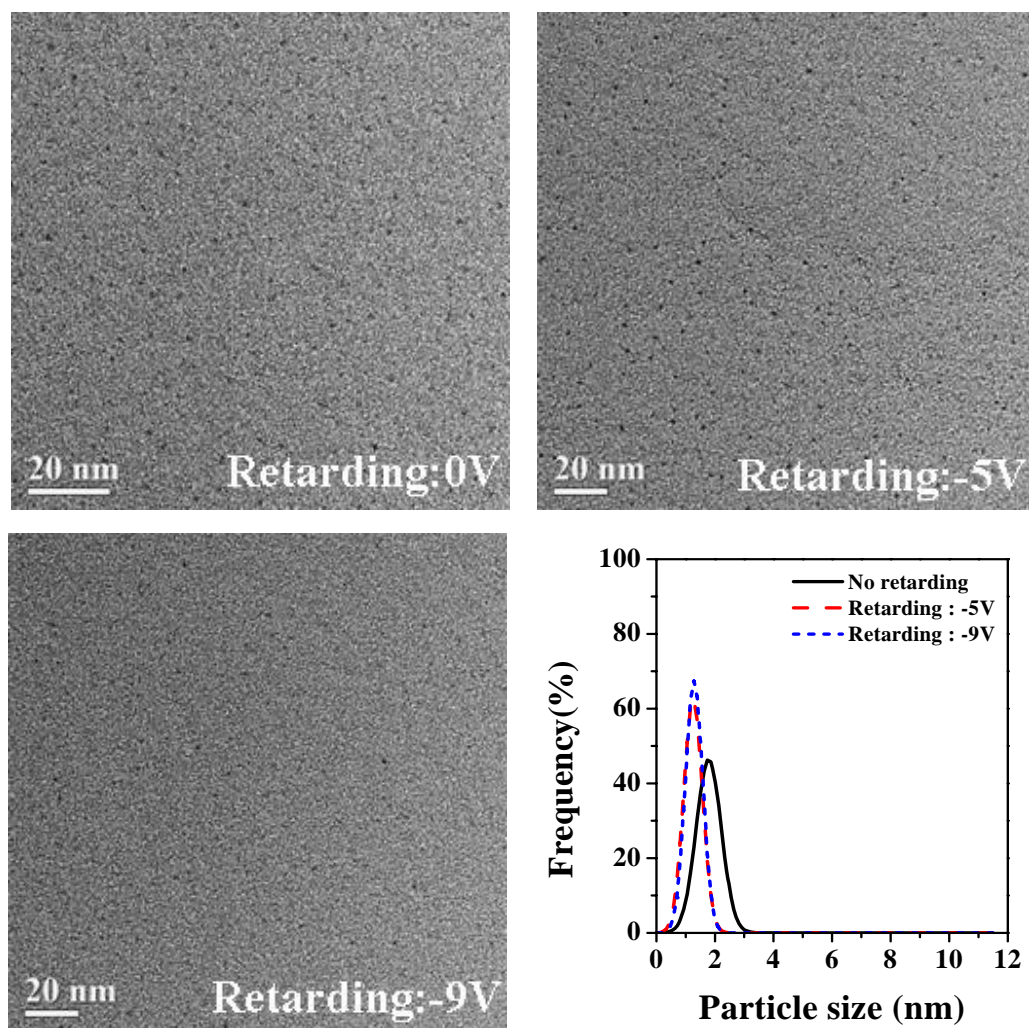


Figure 34. TEM image and particle size distribution at -9V of retarding voltage with a 9.5 pressure ratio at $G1=+200V$. Other grids and sample holder are grounded.

CHAPTER VI

PROGRESS OF SIZE SELECTION OF CLUSTER

Beam Profile

Previously, a Ag target was used to deposit clusters on carbon-coated TEM grids downstream of the MSMF for two hours at the zero pressure ratio with 20 watts of sputter power, but particles were not seen on the grids with TEM and XPS. Therefore, during the experiment and simulation, the hole size of the collector was increased from 0.04" to 0.16" in diameter. The cluster beam profile was measured at 0.15" from the end of the Einzel lens and 1.4" from MSMF downstream by moving the CEM, which gives the ion voltage. For this experiment, clusters were produced at a zero pressure ratio of He to Ar, which was desirable to produce cluster sizes from the atomic scale to 10nm. To minimize beam divergence at the end of the lens, SIMION shows the best value of the potential on each electrode. When the middle electrode (V2) was 100V, shown in Figure 35, there was not a lot of divergence in the beam. Although the beam was well focused at the end of the lens in other conditions, it started to expand through the MSMF. Beam divergence can inhibit size selection of clusters at some positions and makes the selection area small. For simulation, the initial beam spread was set at 0.08" in diameter with an entrance angle of 12.4° , which is the same value of outlet angle in aperture shown in Appendix D. The energy of a 2nm cluster is 4eV from Figure 26. The distance between the starting beam

position and the RFA is 0.7", which is the real distance according to Appendix D. The ion voltage distribution of the experiment was broader.

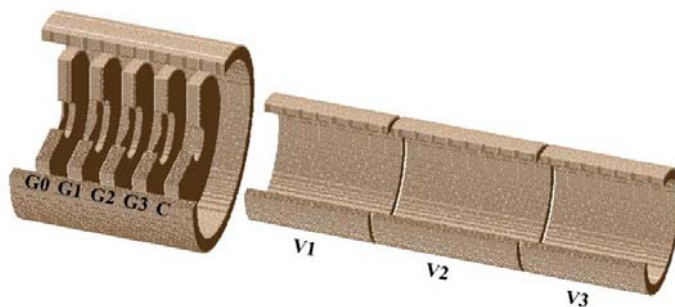


Figure 35. RFA and three-element lenses in SIMION for the potential setting. G0: ground, G1~ C: +20V, V1 and V3: +20V, and V2: +100V. This condition makes the beam spread the least after passing the lens.

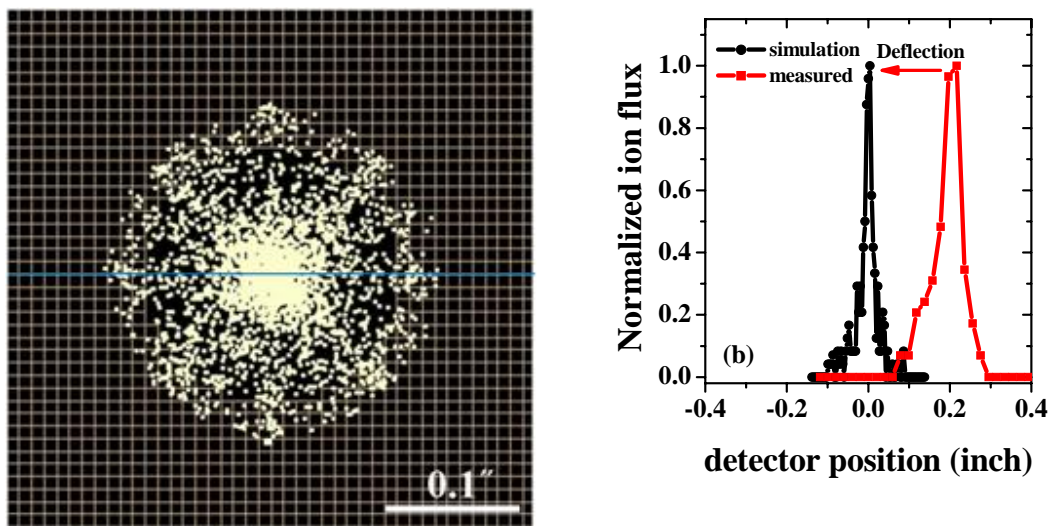


Figure 36. (a) The distribution of ions from the simulation and (b) simulated and experiment at 0.15" from lens. The ion beam is approximately 0.2" in diameter. Blue line in (a) is the beam profile line for (b). Deflector can shift the experimental peak to the simulation result.

Although the beam was not centered on the lens, the simulated result was similar to the experimental trend. The position of the beam could be shifted by a deflector made of four electrodes, which changed the center of the beam by applying an electric potential at different electrodes. The data in Figure 37 using a CEM also shows that the beam spread is almost three times as big as the beam size in Figure 36. SIMION was used to model two separate simulations, because it cannot manipulate two different potentials at the same time, such as the electric and magnetic potentials.

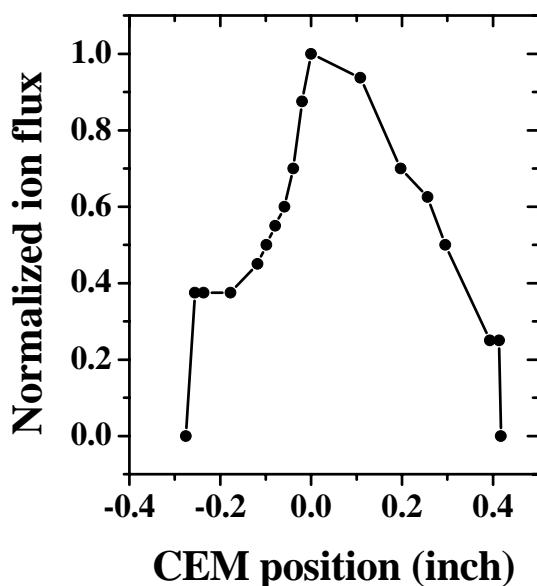


Figure 37. The ion beam profile of 1.4" distance from MSMF. Beam diameter is 0.7".

Figure 38 shows the beam spread superimposed on the magnetic sector to verify the size-selection region. The size-selection region decreases as the distance from the MSMF decreases. Sample substrate and CEM must be installed as close as possible

behind the MSMF. A new lens had to be redesigned to make a well-focused beam through the MSMF.

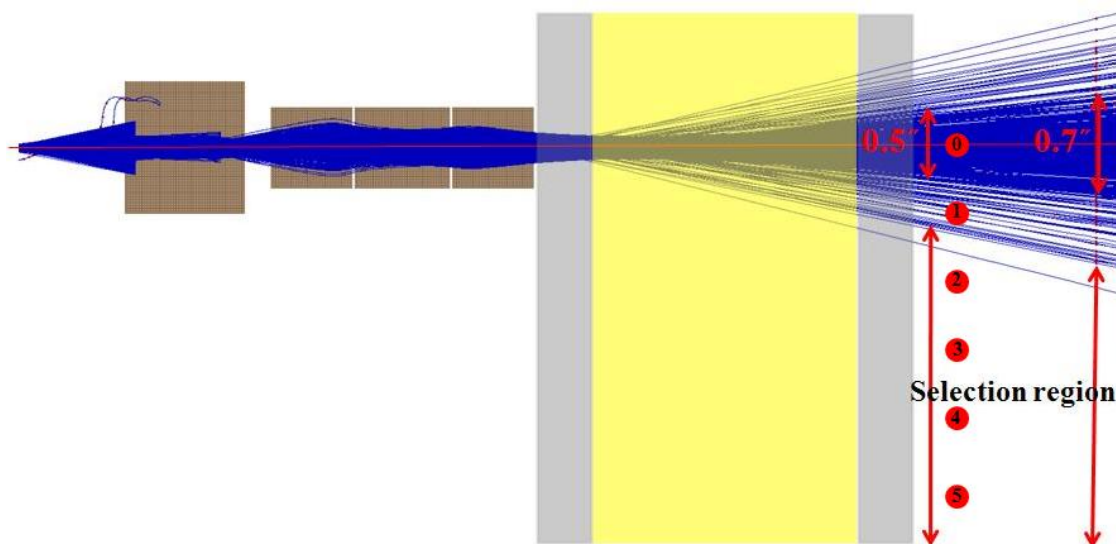


Figure 38. The real area for size selection after MSMF. Beam diameter is 0.5" and 0.7" from direct behind and 1.4" from MSMF. Yellow color is magnet and gray color is the cover of magnets. CEM must be installed as close as possible to increase selection region. Six TEM grids (from 0 to 5 in red circle) were installed at the end of MSMF at intervals of 0.5". TEM grid (0 in red circle) is neutral position.

Magnetic Field Distribution in Magnetic Sector Mass Filter

Figure 39(a) shows the distribution of measured magnetic fields in the MSMF. The magnetic field was measured by a gauss probe (Lake Shore Cryotronics, Inc., Model 410) at the center position of the gap between two magnets by a 0.25" and 0.1" distance from the z-axis and x-axis, respectively. At only 3" and 1" from the z-axis and x-axis was an almost even magnetic field. The Lua program⁷² was introduced to the measured field of the MSMF to apply the same magnetic field in simulation. SIMION brought only one dimensional (y-axis) magnetic field, because three-dimensional magnetic fields could not

be obtained. The measured magnetic field was similar to the simulated field in Figure 39(b).

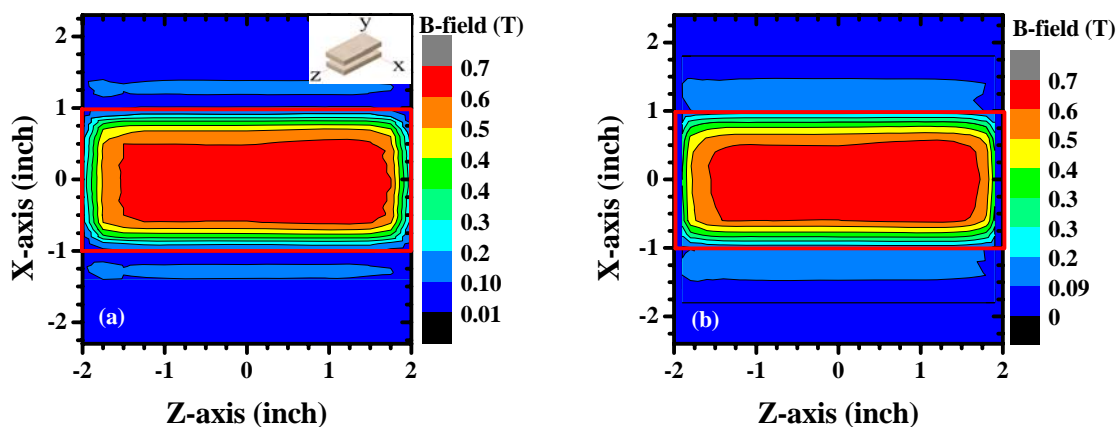


Figure 39. Comparison between (a) real magnetic field and (b) simulated magnetic field. Red line is the size of magnet. Both show the magnetic field without magnets.

The magnetic field was not completely even in the MSMF. It was almost even through the z-axis direction but had a 1" range in the x-axis direction. The beam was introduced at a -1.0" position at the x-axis. Although the area outside of the field was defined by the measured magnetic field, SIMION assumed the fields were zero. Ion trajectories may not be realistic outside of the region.

Size Selection of Cluster

Ion trajectories of different kinetic energies of mass were estimated by SIMION. Figure 40 shows the ion trajectories with different kinetic energy conditions. This helps in evaluating the capability of the MSMF.

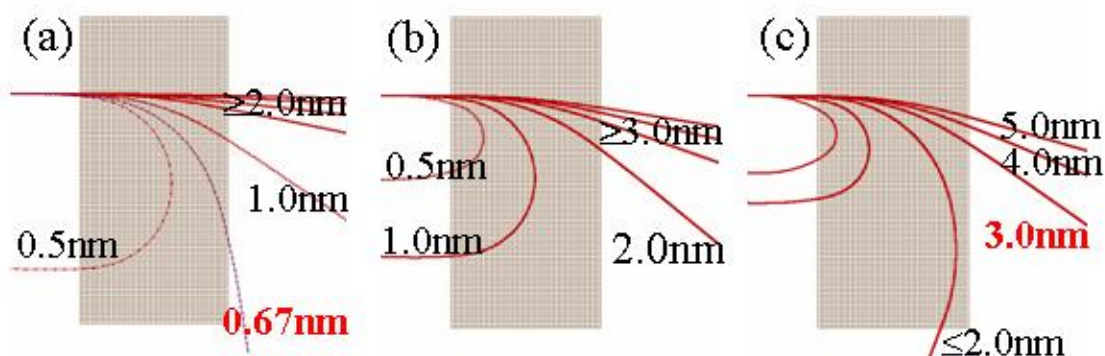


Figure 40. Ion trajectories of (a) 30eV kinetic energy for low mass ($\geq 2.0\text{nm}$), (b) 4eV for the zero pressure ratio, and (c) 1eV kinetic energy for high mass ($\leq 2.0\text{nm}$).

In the previous acceleration experiment shown in Figure 29, the ion energy distribution only goes up to 30V and is not enough to separate clusters less than 1.0nm. As a simulation result, the range of size selection is from 0.67nm (13atoms) to 3.0nm (1120atoms). A better RFA design would be required to control the cluster energy. Before obtaining the ion signal downstream of the MSMF with CEM, the ORTEC 661 ratemeter was set to an optimal threshold to prevent dark current signals, which lead to wrong signals from the CEM, and to 5000 count/sec of full scale range, fast response, 1x multiplier, and 0 ~ 10V of analog output, which was collected by LabVIEW. An oscilloscope also confirmed whether the signals came from the clusters or not. Sixteen data points were collected 10 sec/each position at 1.4" distance from MSMF, as seen in Figure 41.

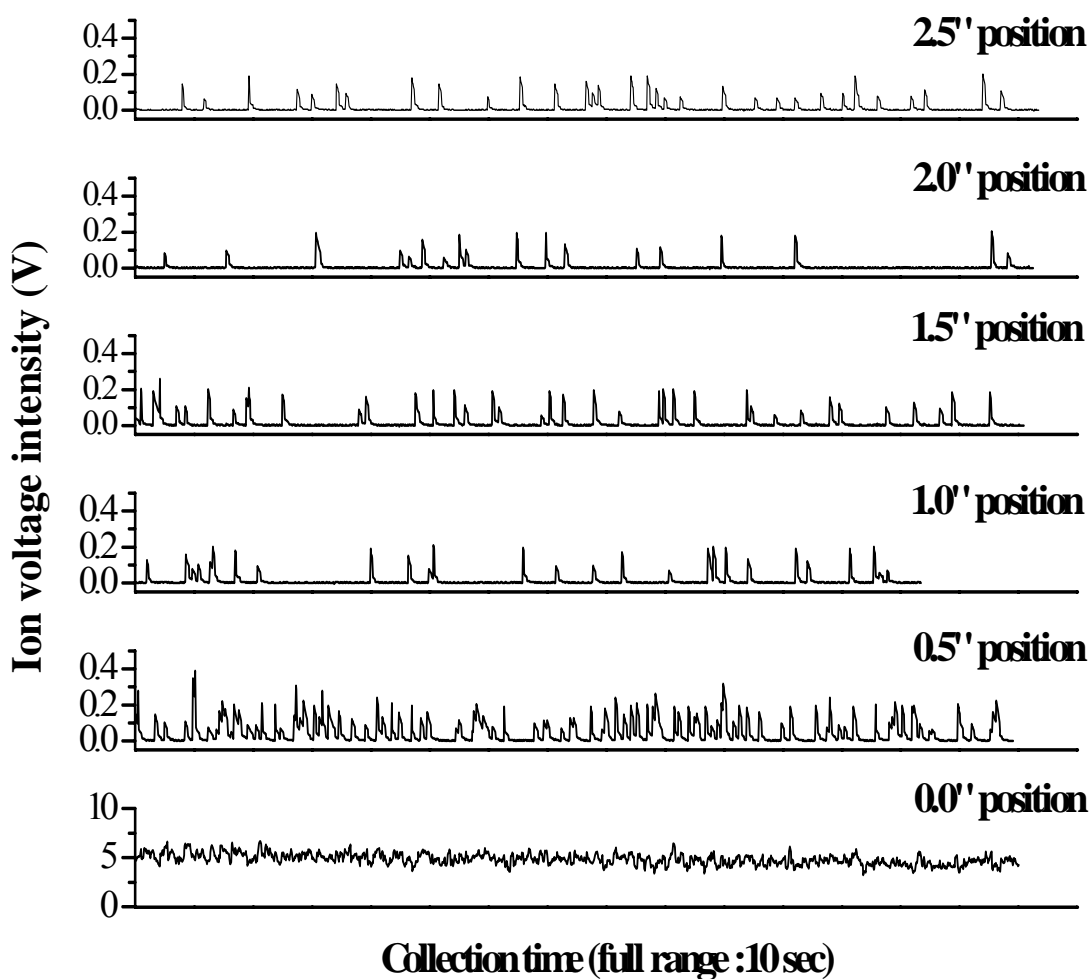


Figure 41. CEM data of Ag clusters at different positions.

At the 0" position of the CEM, the cluster signal was almost constant, unlike other positions, which had only a few signals with low ion voltage intensity. There were many large clusters as well as neutral clusters. Figure 42 shows the normalized ion voltage signal from Figure 41. From 0 (neutral cluster region) to 0.25", the cluster signal was almost constant. Then, the cluster signal dramatically decreased and was almost constant because only a few clusters hit the CEM, as seen in Figure 41.

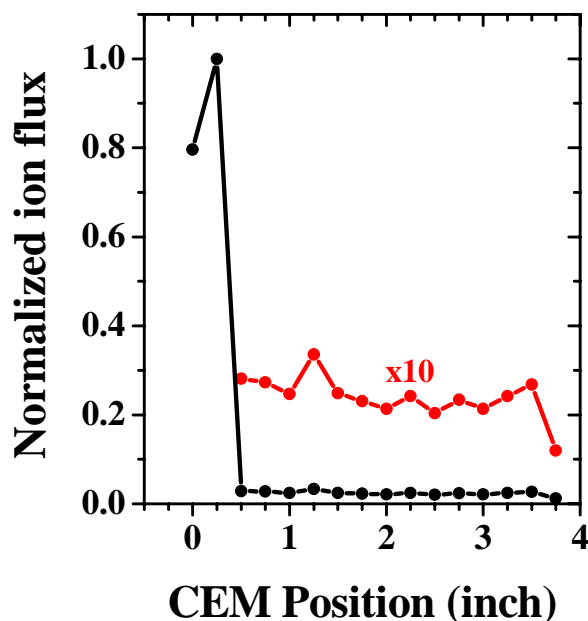


Figure 42. CEM spectrum of negatively charged Ag nanoparticles. 0 position of CEM is for neutral and large clusters. All signals of positions are averaged and normalized from the previous figure.

Before deposition, The MSMF and TEM grids was applied with the same potential, with V3 of lens (Figure 35) to remove the retardation of clusters on six TEM grids installed at intervals of 0.5" as seen in Figure 38. Two Ag targets were sputtered at a zero pressure ratio for four and a half hours. Before obtaining TEM images, the existence of Ag clusters on the TEM grids was tested by XPS. Only two TEM grids (neutral and 0.5" position) had an XPS signal and were imaged by TEM. The results of the size selection of Ag clusters are shown in Figure 43 for the neutral position and in Figure 44 for the 0.5" interval. The particle size in Figure 43 has two different ranges: one area has only clusters ranging from 1.0 to 2.5nm and other areas have a wider cluster range, from 0.9 to 7.0nm. Figure 44 depicts cluster sizes ranging only from 0.8 to 2.2nm, which is

similar to one area seen in Figure 43. The cluster sizes at the neutral position ranged from 0.8 to 7.0nm, as seen in Figure 43. By the trajectory simulation, clusters from 1.7 to 2.5nm having from 5 to 15eV passed through the 0.5" position in the MSMF. For the simulation, this range of kinetic energy of clusters was well matched with Figure 26. Although images show uniformly sized clusters, Figure 44 was not fully supported for size selection because the neutral clusters passed the 0.5" position in Figure 38. More deposition for verifying size selection may be required.

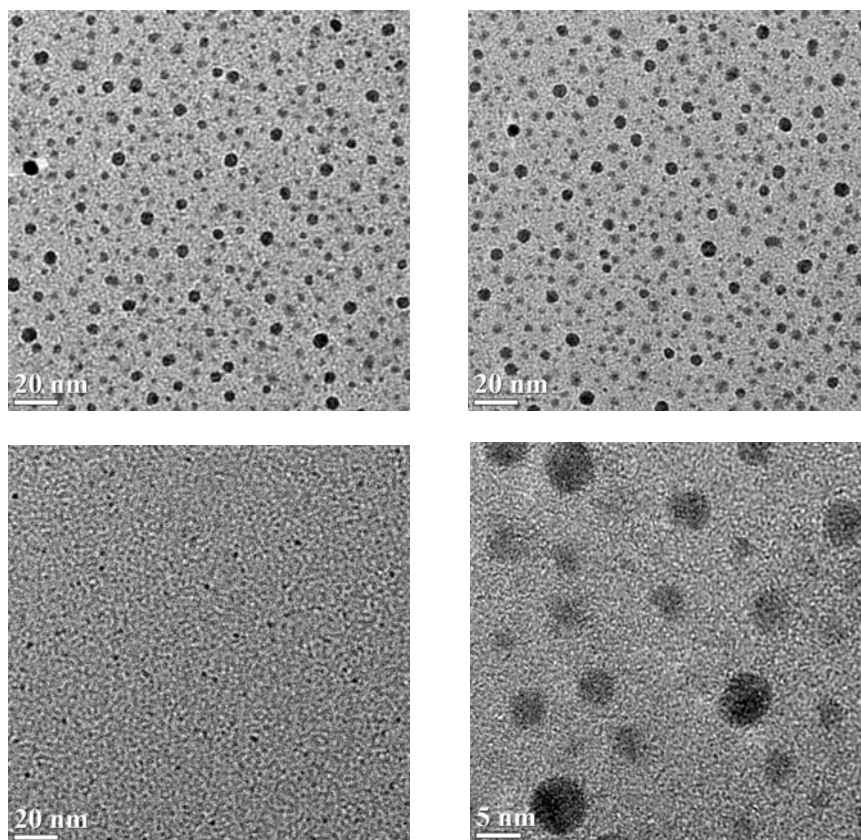


Figure 43. Ag clusters on the TEM grids at the neutral position.

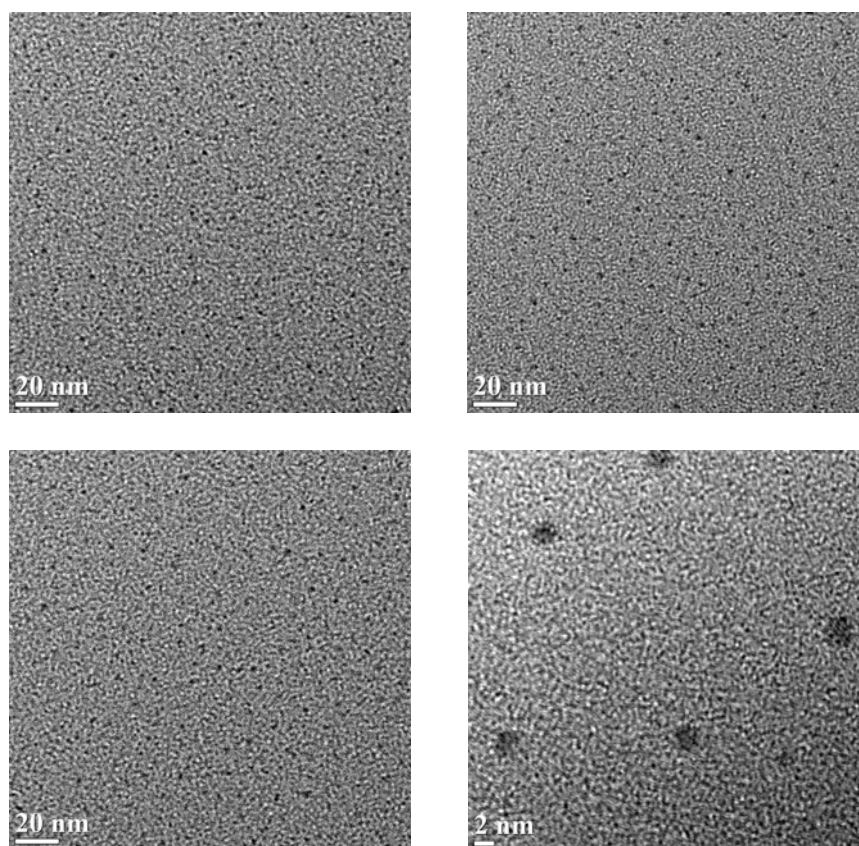


Figure 44. Ag clusters on the TEM grids at the 0.5'' position.

2nd Version of Lens for Focusing Beam

In the previous three-element lens pictured in Figure 38, the charged beam started to spread when the beams left the electric field. To minimize the spread of the beam, a new three-element lens was modified in the first (V1) and last tube (V3) in Figure 45 and Figure 46(a). For the first tube, its conical shape played a role in minimizing beam spread after the third lens. The third tube had a beam guider, a small-sized tube to be introduced directly into the gap of the magnetic sector. The beam guider can be placed on the inside edge of the MSMF.

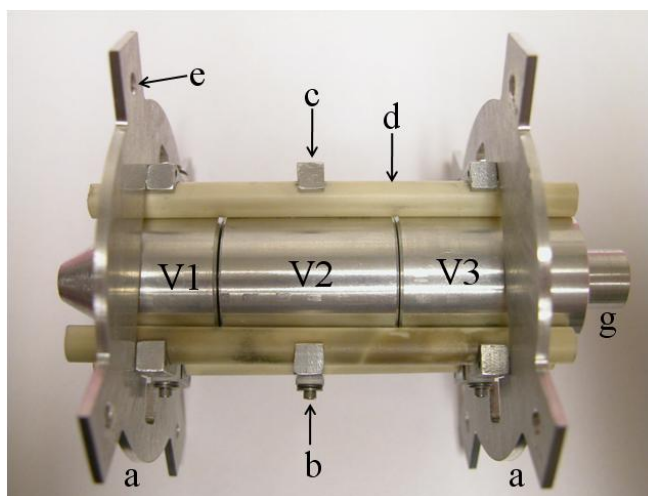


Figure 45. 2nd version of three-element lens. *a* is the holder for installation on the cluster source. *b* is the electrical connector. *c* is the holder for fixing three tubes (V1, V2, and V3). *d* is the ceramic rod from electric field. *e* is the hole for threaded rods which are connected with cluster source. *g* is the beam guider.

When the 2nd version of the lens was designed, beam transmission was considered in order to deal with its spread. If the hole of the conical tube is large, beam transmission is good at the hole of the conical tube, but the spread gets worse downstream in the third tube. Figure 46(b) and (c) show the beam trajectories at low and high electric fields. Both beam diameters in the MSMF were well focused and not spread. For this simulation, the initial beam spread and entrance angle were set to the same value in Appendix D. 30,000 particles which have a negatively charged silver ion of 2nm in diameter were sent into the RFA, and then the beam transmission was calculated by the number of ions passing RFA and lens. The transmission percentage of the ions was about 65% from the end of the RFA to the end of the guider in Figure 45(b). At high voltage, beam transmission goes down to 15%. A long deposition time was required to get a high enough number of

clusters. Ion current after RFA and lens may be required to find proper deposition time.

The 2nd version of the lens will be tested soon.

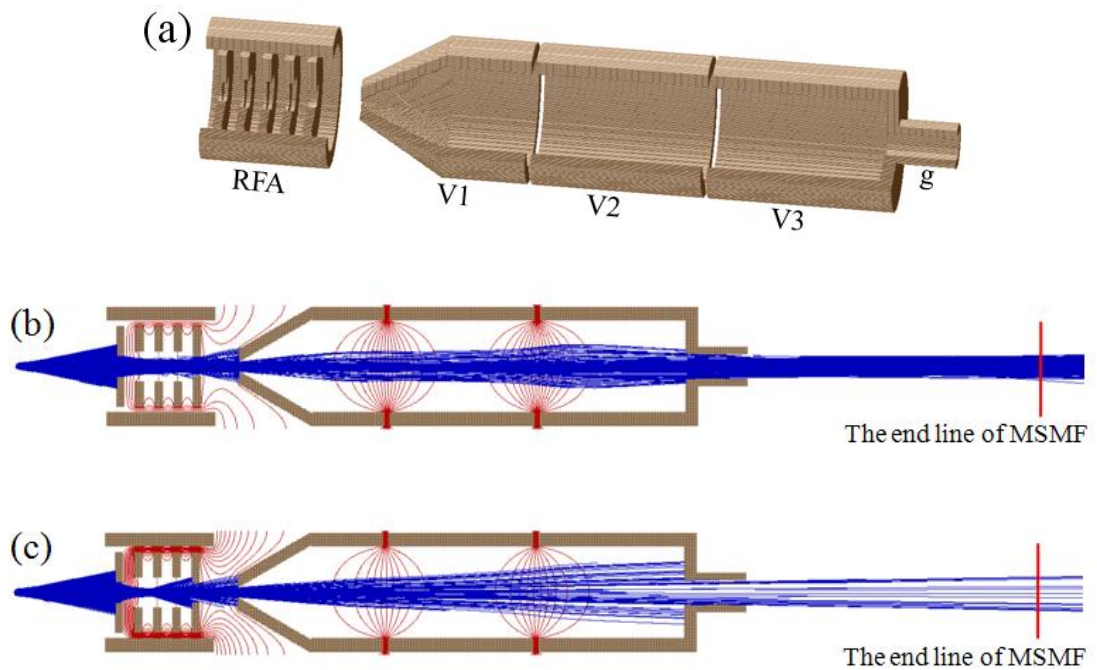


Figure 46. (a) 2nd version of Einzel lens to minimize the beam spread including g, beam guider. (b) Beam trajectory at V1 and V3 = +20V, V2 = +100V. (c) Beam trajectory at V1 and V3 = +1.0kV, and V2 = +2.0kV.

CHAPTER VII

CONCLUSION AND FUTURE WORK

Conclusions

Nanoclusters have recently received a tremendous amount of attention because of their fundamental importance in chemistry and physics for application in catalysis and nanotechnology. Cluster properties can be changed by controlling the size of the cluster. Current mass filters, which are Wien velocity, time of flight, quadrupole, and magnetic sector mass, have a limited range of mass selection. A new mass filter is required for a high-flux beam of clusters that can separate clusters up to 10nm in diameter without sacrificing its resolution.

In this experiment, Matilda was designed for the deposition of size-selected nanoparticles ranging from atomic scale to 10nm. Matilda has a nanocluster source (1st and 2nd version) based on magnetron sputtering, an RFA (1st and 2nd version) providing ion energy distribution information, a three-element lens to focus and introduce beams into the MSMF, and an MSMF for size separation up to 3nm. For testing size distribution, nanoclusters were deposited on carbon-coated TEM grids with different pressure ratios between He and Ar. Size distribution varied from 10nm to 0.5nm by increasing the pressure ratio. At the highest pressure ratio, size distribution was much more narrow than at the low pressure ratio. This means that pressure ratio can control size selection up to 4nm, although 4nm in diameter has a size variation of ± 2 nm. The RFA collected ion

energy distribution with different sputter powers, aggregation distances, pressure ratios, and acceleration voltages. The ion energy distribution increased with increasing sputter power because of the increase in ion flux. With increasing aggregation distances, the ion energy distribution and flux decreased, because kinetic energy was lowered by many body collisions before the skimmer. Increasing the pressure ratio decreased ion energy and flux. When grids were applied with a high voltage, the ion energy distribution broadened. An acceleration voltage may allow separation between low mass occupying high energy regions and high mass occupying low energy regions. To understand the stretching of ion energy distribution, further tests varying the retarding voltage are required for determining the correlation between mass and acceleration. Most of clusters were deposited on the substrate with soft landing ($\leq 0.1\text{eV}$ kinetic energy). Only at a zero pressure ratio of He/Ar was the maximum landing energy higher than that of the soft landing. Further analysis with scanning tunneling microscope is needed to acquire three-dimensional images of clusters which would verify the soft and hard landing cluster cases. The retarding effect was demonstrated by SIMION, as well as experiments to verify the design of ion optics of the RFA. This effect clearly shows the number of transmitted clusters, which was decreased by increasing the retarding voltage; however, the particle size distribution could not clearly be explained because of the outlier effect of neutral clusters.

For the size selection experiment, the three-element lens, the MSMF, and the CEM were installed in the chamber. The three-element lens produced the narrow-sized and focused beam for the MSMF. The beam profile was about 0.25" at the end of the lens and 0.7" from a distance of 1.4" from the MSMF. The simulation result was well

matched to the experimental results. The real magnetic field was introduced into SIMION by the Lua program for simulating similar conditions. The results agreed with the real magnetic field. The CEM collected cluster signals at different positions, and a Ag target was used to deposit clusters on the TEM grid for four and a half hours. The cluster signal was high from the 0 to 0.25" position, but the signal decreased rapidly far away from the neutral cluster region. By simulation and TEM images, size selection was verified, but more testing may be required because of the beam spread. For cluster separation according to mass-to-charge ratio in the MSMF, the ion energy of the clusters and their distribution must be precisely controlled by acceleration or deceleration. Finally, Matilda provided narrow particle sized distribution from atomic scale to 4nm in size with different pressure ratio without additional mass filter. It is very economical way to produce relatively narrow particle size distribution.

Future Work

The cluster source of the 2nd version still has difficulties in the line connection of the RFA. Electrical connectors need to be installed on flange. Also, a translator is needed to adjust the aggregation distance without breaking the vacuum. The RFA may not only require an increased copper mesh diameter to accelerate clusters and control ion energy efficiently, but also require many holes to exhaust gas mixtures to prevent a short circuit. Also, a high mass flow rate with several stages of a differential pumping system is helpful for increasing the ion energy distribution effectively. For beam focusing, the lens requires longer and bigger diameters and a deflector to shift the center of the beam to the center of the lens. The simulation will be required to find the proper sizes of lens and

deflector. For high mass filtering, the cluster system requires a large magnet to obtain a high magnetic field which is up to 1.5T. The additional setup required may add to the cost of the experiment. However, these adjustments are not the final solution for building a size-selected cluster system for the high mass region. To control particle size distribution up to the 10nm regime, a new system consisting of two mass filters, such as a QMF and PFMS, is required. The QMF is suitable for low mass regions with high resolution, and the PFMS is desirable for high mass regions with a simple design, high transmission, and fairly good mass resolution. For this system, a quadrupole deflector is required to send beams to the QMF and PFMS.

REFERENCES

1. See, U.S. Department of Energy Hydrogen, Fuel Cells and Infrastructure Technologies Program Multi-Year Research, Development and Demonstration Plan, U.S Department of Energy; <http://www1.eere.energy.gov/hydrogenandfuelcells/> (2007).
2. Chalk, S. G.; Miller, J. E., Key challenges and recent progress in batteries, fuel cells, and hydrogen storage for clean energy systems. *Journal of Power Sources* **2006**, 159, (1), 73-80.
3. Antolini, E., Formation, microstructural characteristics and stability of carbon supported platinum catalysts for low temperature fuel cells. *Journal of Materials Science* **2003**, 38, (14), 2995-3005.
4. Ertl, G.; Knozinger, H.; Weitkamp, J.; Shchuth, F.; Weitkamp, J., *Handbook of Heterogenous Catalysis, Vol. 1* **1997**, second ed. (Wiley-VCH, 2008).
5. Moulijn, J. A.; van leeuwen, P. W. N. M.; van Santen, R. A., *Catalysis: An Integrated Approach to Homogeneous, Heterogeneous and Industrial Catalysis*, (Elsevier Science, Amsterdam, 2002).
6. Kasemo, B.; Johansson, S.; Persson, H.; Thormahlen, P.; Zhdanov, V. P., Catalysis in the nm-regime: manufacturing of supported model catalysts and theoretical studies of the reaction kinetics. *Topics in Catalysis* **2000**, 13, (1-2), 43-53.
7. Song, H.; Rioux, R. M.; Hoefelmeyer, J. D.; Komor, R.; Niesz, K.; Grass, M.; Yang, P. D.; Somorjai, G. A., Hydrothermal growth of mesoporous SBA-15 silica in the presence of PVP-stabilized Pt nanoparticles: Synthesis, characterization, and catalytic properties. *Journal of the American Chemical Society* **2006**, 128, (9), 3027-3037.
8. Gates, B. C., Models of metal catalysts: beyond single crystals. *Topics in Catalysis* **2001**, 14, (1-4), 173-180.
9. Somorjai, G. A.; Tao, F.; Park, J. Y., The nanoscience revolution: Merging of colloid science, catalysis and nanoelectronics. *Topics in Catalysis* **2008**, 47, (1-2), 1-14.

10. Liu, Z.; Reed, D.; Kwon, G.; Shamsuzzoha, M.; Nikles, D. E., Pt₃Sn nanoparticles with controlled size: High-temperature synthesis and room-temperature catalytic activation for electrochemical methanol oxidation. *Journal of Physical Chemistry C* **2007**, 111, 14223-14229.
11. Liu, Z. F.; Shamsuzzoha, M.; Ada, E. T.; Reichert, W. M.; Nikles, D. E., Synthesis and activation of Pt nanoparticles with controlled size for fuel cell electrocatalysts. *Journal of Power Sources* **2007**, 164, (2), 472-480.
12. Zeng, J. H.; Su, F. B.; Han, Y. F.; Tian, Z. Q.; Poh, C. K.; Liu, Z. L.; Lin, J. Y.; Lee, J. Y.; Zhao, X. S., Pt nanoparticles supported on sandwiched Ru/Carbon nanocomposite as a bimetallic catalyst for methanol electrooxidation. *Journal of Physical Chemistry C* **2008**, 112, (40), 15908-15914.
13. Haruta, M., Size- and support-dependency in the catalysis of gold. *Catalysis Today* **1997**, 36, (1), 153-166.
14. Valden, M.; Lai, X.; Goodman, D. W., Onset of catalytic activity of gold clusters on titania with the appearance of nonmetallic properties. *Science* **1998**, 281, (5383), 1647-1650.
15. Valden, M.; Pak, S.; Lai, X.; Goodman, D. W., Structure sensitivity of CO oxidation over model Au/TiO₂ catalysts. *Catalysis Letters* **1998**, 56, (1), 7-10.
16. Haruta, M.; Ueda, A.; Tsubota, S.; Sanchez, R. M. T., Low-temperature catalytic combustion of methanol and its decomposed derivatives over supported gold catalysts. *Catalysis Today* **1996**, 29, (1-4), 443-447.
17. Wong, K.; Johansson, S.; Kasemo, B., Nanofabricated model catalysts - Manufacturing and model studies. *Faraday Discussions* **1996**, 105, 237-246.
18. Hwang, K. S.; Yang, M. C.; Zhu, J.; Grunes, J.; Somorjai, G. A., The molecular mechanism of the poisoning of platinum and rhodium catalyzed ethylene hydrogenation by carbon monoxide. *Journal of Molecular Catalysis A-Chemical* **2003**, 204, 499-507.
19. Eppler, A. S.; Zhu, J.; Anderson, E. A.; Somorjai, G. A., Model catalysts fabricated by electron beam lithography: AFM and TPD surface studies and hydrogenation/dehydrogenation of cyclohexene plus H₂ on a Pt nanoparticle array supported by silica. *Topics in Catalysis* **2000**, 13, (1-2), 33-41.

20. Zhu, J.; Somorjai, G. A., Formation of platinum silicide on a platinum nanoparticle array model catalyst deposited on silica during chemical reaction. *Nano Letters* **2001**, 1, (1), 8-13.
21. Bowker, M., Catalysis resolved using scanning tunnelling microscopy. *Chemical Society Reviews* **2007**, 36, 1656-1673.
22. Poppa, H., Nucleation, Growth, and Tem Analysis of Metal Particles and Clusters Deposited in UHV. *Catalysis Reviews-Science and Engineering* **1993**, 35, (3), 359-398.
23. Thomas, M.; Dickinson, J. T.; Poppa, H.; Pound, G. M., Chemisorption of CO on Pd particles supported on mica. *Journal of Vacuum Science and Technology* **1978** 15, (2), 568-571
24. Abbet, S.; Sanchez, A.; Heiz, U.; Schneider, W. D.; Ferrari, A. M.; Pacchioni, G.; Rosch, N., Acetylene cyclotrimerization on supported size-selected Pd-n clusters ($1 \leq n \leq 30$): one atom is enough! *Journal of the American Chemical Society* **2000**, 122, (14), 3453-3457.
25. Sanchez, A.; Abbet, S.; Heiz, U.; Schneider, W. D.; Hakkinen, H.; Barnett, R. N.; Landman, U., When gold is not noble: Nanoscale gold catalysts. *Journal of Physical Chemistry A* **1999**, 103, (48), 9573-9578.
26. Heiz, U.; Sanchez, A.; Abbet, S.; Schneider, W. D., Catalytic oxidation of carbon monoxide on monodispersed platinum clusters: Each atom counts. *Journal of the American Chemical Society* **1999**, 121, (13), 3214-3217.
27. Lee, S.; Fan, C. Y.; Wu, T. P.; Anderson, S. L., Cluster size effects on CO oxidation activity, adsorbate affinity, and temporal behavior of model Au-n/TiO₂ catalysts. *Journal of Chemical Physics* **2005**, 123.124701-124713
28. Toyoda, N.; Houzumi, S.; Yamada, I., Development of a size-selected gas cluster ion beam system for low-damage processing. *Nuclear Instruments & Methods in Physics Research Section B* **2005**, 241, (1-4), 609-613.
29. Yamada, I.; Matsuo, J.; Toyoda, N.; Kirkpatrick, A., Materials processing by gas cluster ion beams. *Materials Science & Engineering R-Reports* **2001**, 34, (6), 231-295.

30. Bromann, K.; Brune, H.; Felix, C.; Harbich, W.; Monot, R.; Buttet, J.; Kern, K., Hard and soft landing of mass selected Ag clusters on Pt(111). *Surface Science* **1997**, 377, (1-3), 1051-1055.
31. Carroll, S. J.; Pratontep, S.; Streun, M.; Palmer, R. E.; Hobday, S.; Smith, R., Pinning of size-selected Ag clusters on graphite surfaces. *Journal of Chemical Physics* **2000**, 113, (18), 7723-7727.
32. Parent, F.; Tuaille, J.; Stern, L. B.; Dupuis, V.; Prevel, B.; Perez, A.; Melinon, P.; Guiraud, G.; Morel, R.; Barthelemy, A.; Fert, A., Giant magnetoresistance in Co-Ag granular films prepared by low-energy cluster beam deposition. *Physical Review B* **1997**, 55, (6), 3683-3687.
33. Lidgi-Guigui, N.; Leung, C.; Palmer, R. E., Weak precursor state binding of protein molecules to size-selected gold nanoclusters on surfaces. *Surface Science* **2008**, 602, (4), 1006-1009.
34. Sattler, K.; Muhlbach, J.; Recknagel, E., Generation of Metal Clusters Containing from 2 to 500 Atoms. *Physical Review Letters* **1980**, 45, (10), 821-824.
35. Dietz, T. G., Duncan, M. A., Powers, D. E., and Smalley, R. E. , Laser production of supersonic metal cluster beams. *Journal of Chemical Physics* **1981**, 74, (11), 6511-6512.
36. Binns, C., Nanoclusters deposited on surfaces. *Surface Science Reports* **2001**, 44, (1-2), 1-49.
37. Laaksonen, R. T.; Goetsch, D. A.; Owens, D. W.; Poirier, D. M.; Stepniak, F.; Weaver, J. H., Supersonic Cluster Source with Mass Selection and Energy Control. *Review of Scientific Instruments* **1994**, 65, (7), 2267-2275.
38. Nakajima, A.; Hoshino, K.; Naganuma, T.; Sone, Y.; Kaya, K., Ionization-Potentials of Aluminum Sodium Bimetallic Clusters (Al_nNa_m). *Journal of Chemical Physics* **1991**, 95, (10), 7061-7066.
39. Lau, J. T.; Achleitner, A.; Ehrke, H. U.; Langenbuch, U.; Reif, M.; Wurth, W., Ultrahigh vacuum cluster deposition source for spectroscopy with synchrotron radiation. *Review of Scientific Instruments* **2005**, 76, (6), 63902-63908.

40. Haberland, H.; Karrais, M.; Mall, M., A New Type of Cluster and Cluster Ion-Source. *Zeitschrift Fur Physik D-Atoms Molecules and Clusters* **1991**, 20, (1-4), 413-415.
41. Siekmann, H. R.; Luder, C.; Faehrmann, J.; Lutz, H. O.; Meiwesbroer, K. H., The Pulsed-Arc Cluster Ion-Source (Pacis). *Zeitschrift Fur Physik D-Atoms Molecules and Clusters* **1991**, 20, (1-4), 417-420.
42. Heiz, U.; Vanolli, F.; Trento, L.; Schneider, W. D., Chemical reactivity of size-selected supported clusters: An experimental setup. *Review of Scientific Instruments* **1997**, 68, (5), 1986-1994.
43. Baker, S. H.; Thornton, S. C.; Keen, A. M.; Preston, T. I.; Norris, C.; Edmonds, K. W.; Binns, C., The construction of a gas aggregation source for the preparation of mass-selected ultrasmall metal particles. *Review of Scientific Instruments* **1997**, 68, (4), 1853-1857.
44. Bromann, K.; Felix, C.; Brune, H.; Harbich, W.; Monot, R.; Buttet, J.; Kern, K., Controlled deposition of size-selected silver nanoclusters. *Science* **1996**, 274, (5289), 956-958.
45. Smith, R., Clampitt, R., and Lee, M. , Magnetron-based nanocluster source: capabilities, limitations and future possibilities presented in University of Alabama. **2005**.
46. Goldby, I. M.; vonIssendorff, B.; Kuipers, L.; Palmer, R. E., Gas condensation source for production and deposition of size-selected metal clusters. *Review of Scientific Instruments* **1997**, 68, (9), 3327-3334.
47. Wrenger, B.; MeiwesBroer, K. H., The application of a Wien filter Its mass analysis of heavy clusters from a pulsed supersonic nozzle source. *Review of Scientific Instruments* **1997**, 68, (5), 2027-2030.
48. Haberland, H.; Karrais, M.; Mall, M.; Thurner, Y., Thin-films from energetic cluster impact - A feasibility study. *Journal of Vacuum Science & Technology A* **1992**, 10, (5), 3266-3271.
49. Turra, M.; Waldschmidt, B.; Kaiser, B.; Schafer, R., An improved time-of-flight method for cluster deposition and ion-scattering experiments. *Review of Scientific Instruments* **2008**, 79, (1), 13905-13909.

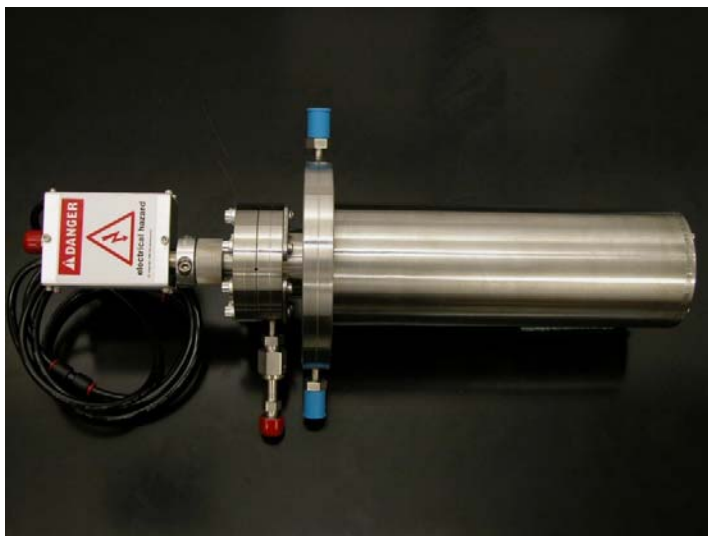
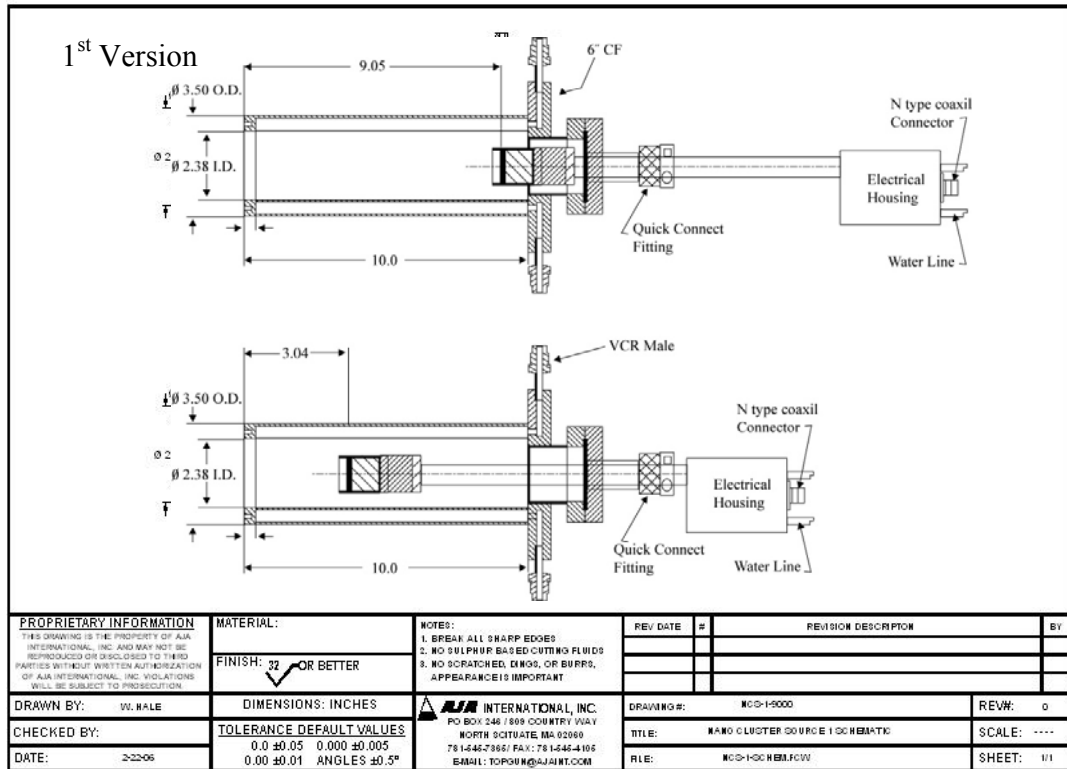
50. von Issendorff, B.; Palmer, R. E., A new high transmission infinite range mass selector for cluster and nanoparticle beams. *Review of Scientific Instruments* **1999**, 70, (12), 4497-4501.
51. Pratontep, S.; Carroll, S. J.; Xirouchaki, C.; Streun, M.; Palmer, R. E., Size-selected cluster beam source based on radio frequency magnetron plasma sputtering and gas condensation. *Review of Scientific Instruments* **2005**, 76, (4), 45103-45109.
52. Kemper, P.; Kolmakov, A.; Tong, X.; Lilach, Y.; Benz, L.; Manard, M.; Metiu, H.; Buratto, S. K.; Bowers, M. T., Formation, deposition and examination of size selected metal clusters on semiconductor surfaces: An experimental setup. *International Journal of Mass Spectrometry* **2006**, 254, (3), 202-209.
53. Klingeler, R.; Bechthold, P. S.; Neeb, M.; Eberhardt, W., An experimental setup for nondestructive deposition of size-selected clusters. *Review of Scientific Instruments* **2002**, 73, (4), 1803-1808.
54. Wucher, A.; Wahl, M.; Oechsner, H., The mass-distribution of sputtered metal-clusters .1. Experiment. *Nuclear Instruments & Methods in Physics Research Section B-Beam Interactions with Materials and Atoms* **1993**, 83, (1-2), 73-78.
55. Ayesh, A. I.; Lassesson, A.; Brown, S. A.; Dunbar, A. D. F.; Kaufmann, M.; Partridge, J. G.; Reichel, R.; van Lith, J., Experimental and simulational study of the operation conditions for a high transmission mass filter. *Review of Scientific Instruments* **2007**, 78, (5), 53906-53912.
56. de Hoffman, E.; Stroobant, V., *Mass Spectrometry Principles and Applications*, (John Wiley and Sons, Ltd, 2002).
57. Henderson, W.; McIndoe, J. S., *Mass Spectrometry of Inorganic and Organometallic Compounds*, (Wiley-Interscience, 2005).
58. Moulder, J. F.; Stickle, W. F.; Sobol, P. E.; Bomben, K. D.; Chastain, J.; King, J., R. C. , *Handbook of X-ray Photoelectron Spectroscopy* (Physcal Electronics, Inc. Eden Prairie, MN, 1995).
59. Attard, G.; Barness, C., *Surfaces*, (Oxford University Press Inc., New York, NY, 1998).

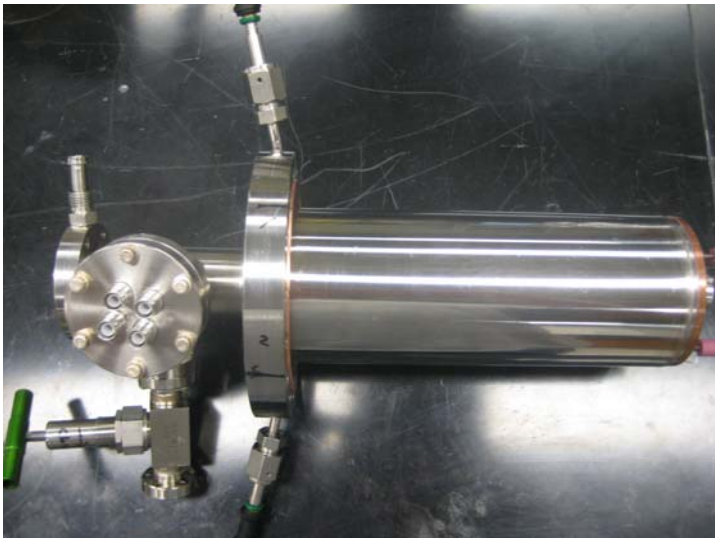
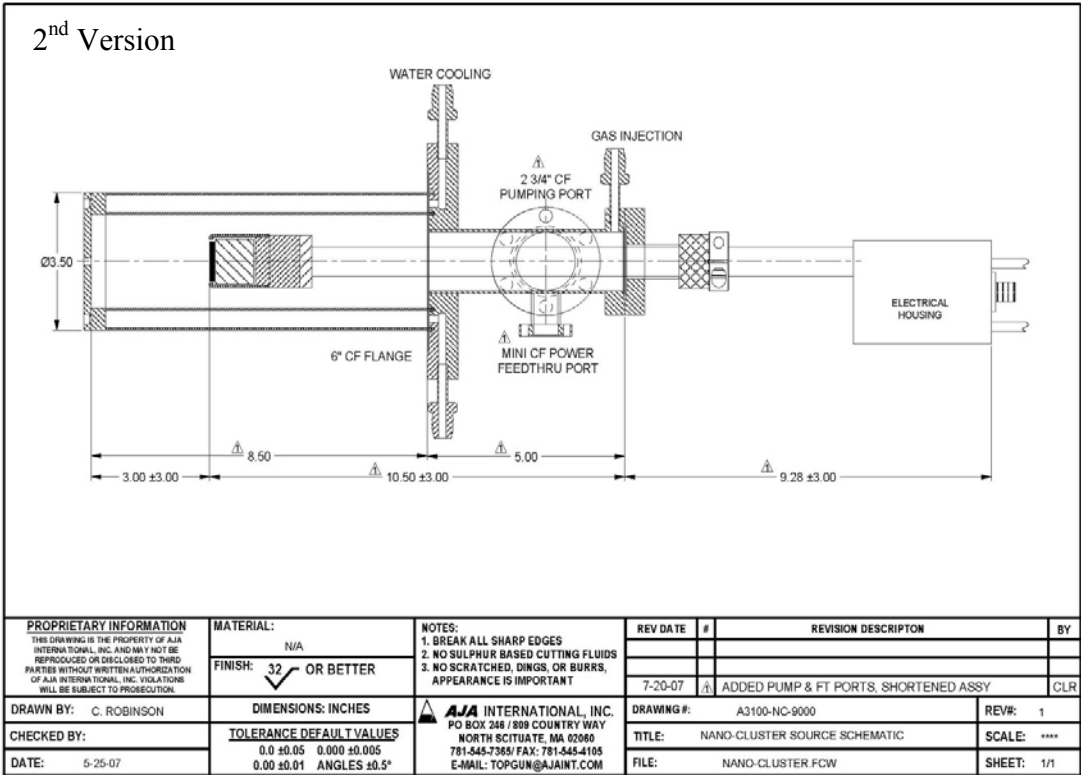
60. Williams, D. B.; Carter, C. B., *Transmission Electron Microscopy*, first ed. (Springer, New York, NY, 2004).
61. Liu, J. Y., Scanning transmission electron microscopy and its application to the study of nanoparticles and nanoparticle systems. *Journal of Electron Microscopy* **2005**, 54, 251-278.
62. Rioux, R. M.; Song, H.; Hoefelmeyer, J. D.; Yang, P.; Somorjai, G. A., High-surface-area catalyst design: Synthesis, characterization, and reaction studies of platinum nanoparticles in mesoporous SBA-15 silica. *Journal of Physical Chemistry B* **2005**, 109, (6), 2192-2202.
63. Haberland, H.; Mall, M.; Moseler, M.; Qian, Y.; Reiners, T.; Thurner, Y., Filing of micron-sized contact holes with copper by energetic cluster-impact. *Journal of Vacuum Science & Technology A* **1994**, 12, (5), 2925-2930.
64. Koch, J., A small retarding field analyzer for Auger electron spectroscopy. *Review of Scientific Instruments* **1974**, 45, (10), 1212-1213.
65. Bohm, C.; Perrin, J., Retarding-field analyzer for measurements of ion energy distributions and secondary electron emission coefficients in low-pressure radio frequency discharges. *Review of Scientific Instruments* **1993**, 64, (1), 31-44.
66. Manura, D. J.; Dahl, D. A., *SIMION Version 8.0 User Manual*, (Scientific Instrument Services, Inc, USA, Ringoes, NJ, 2007).
67. Tompkins, H. G., *Vacuum Gauging and Control*, (The American Vacuum Society Education Committee, New York, NY, 1994).
68. See, *Technical Notes*, Detector Technology, Inc;
<http://www.detechnic.com/notes.htm>.
69. See, *Channeltron Electron Multiplier Handbook for Spectrometry Applications* Burle Industries, Inc;
<http://www.burle.com/cgi-bin/byteserver.pl/pdf/ChannelBook.pdf>.
70. Haberland, H.; Insepov, Z.; Moseler, M., Molecular-dynamics simulation of thin-film growth by energetic cluster-impact. *Physical Review B* **1995**, 51, (16), 11061-11067.

71. Anderson, T. G.; Birdsey, B. G.; Woehner, S. M.; Rosenberry, M. A.; Gay, T. J., A theoretical study of the effects of insulators on electron transport through electrostatic tube lenses. *Review of Scientific Instruments* **2001**, 72, (7), 2923-2925.
72. Ierusalimschy, R., *Programming in Lua* (Departamento de Informatica, PUC-Rio, Brazil, Rio de Janeiro, 2006).

APPENDIX A

SCHEMATICS OF NANOCUSTER SOURCES





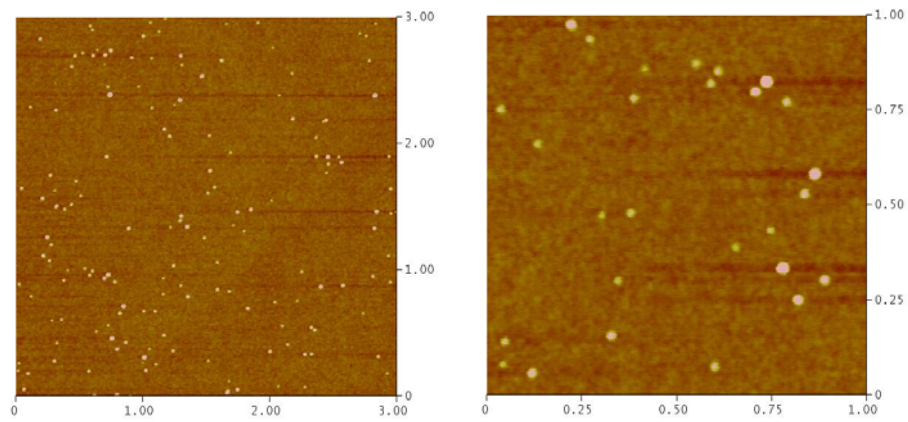
APPENDIX B

PERFORMANCE OF 1ST VERSION OF NANOCUSTER SOURCE

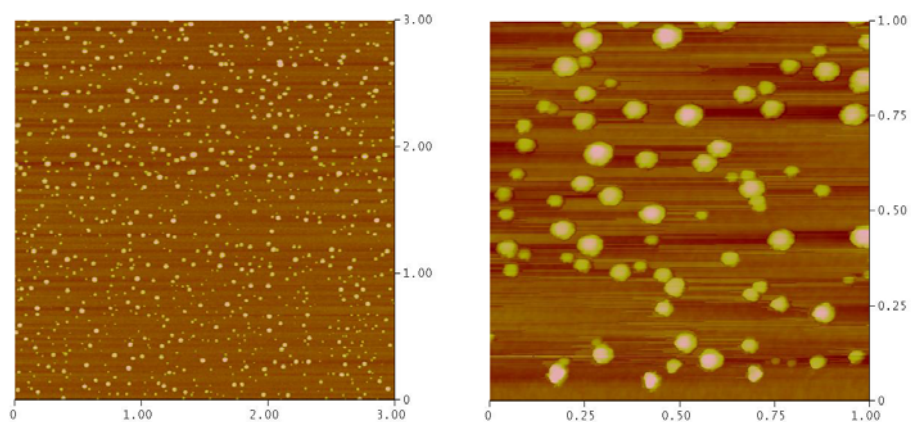
First we strove to find the conditions for controlling the size of the nanoclusters, but we did not have much time to test it thoroughly because it had some problems. Test results were introduced with the AFM and TEM.

AFM Images (Image Scale: $1 \times 1 \mu\text{m}$)

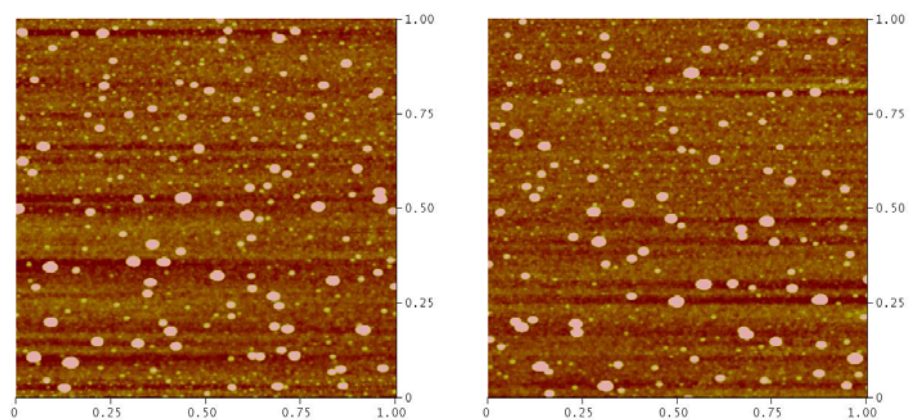
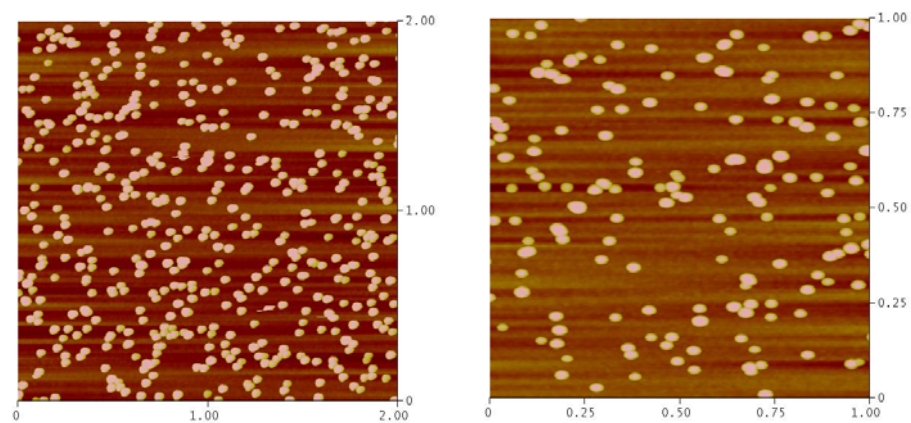
Sample 12



Sample 17

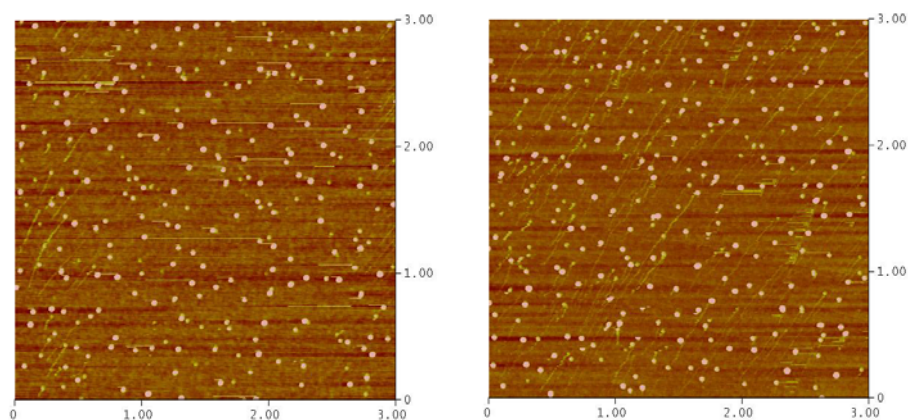


Sample 23



Sample 30

Sample 31



Experimental Conditions

Sample	Sputter power (watt)	Gas flow rate (sccm)		Pressure (torr)	Dep.time (min)	Agg. Distance (inch)	RFA
		Ar	He				
12	10	14	0	6.0×10^{-4}	10	4	Yes
17	50	14	0	5.8×10^{-4}	10	2	No
23	50	7	0	2.1×10^{-4}	3	4	No
30	50	14	14	5.9×10^{-4}	10	2	No
31	10	0.4	14	5.3×10^{-4}	20	2	No

* Pressures are not much different due to main chamber pressure.

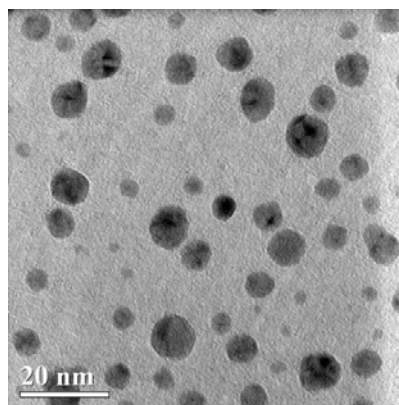
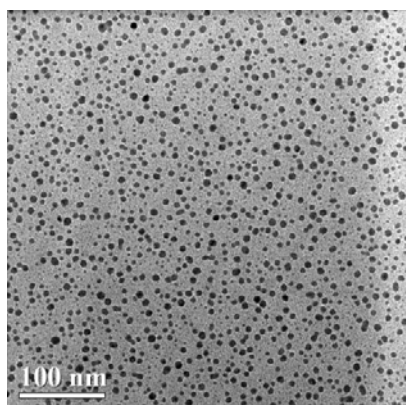
Particle Size Distribution

Sample	Range of particle size (nm)
12	25 ~ 65
17	25 ~ 80
23	40 ~ 70
30	10 ~ 55
31	35 ~ 70

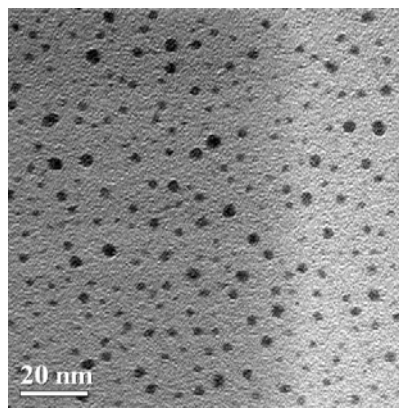
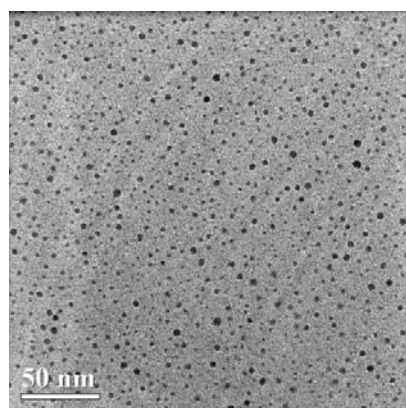
TEM Images

Increasing the He flow rate narrowed the size distribution of the Ag nanoparticles deposited on the carbon-coated TEM grid.

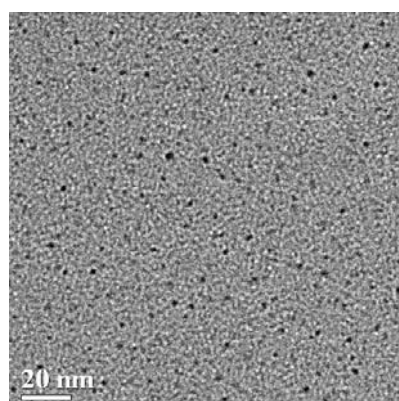
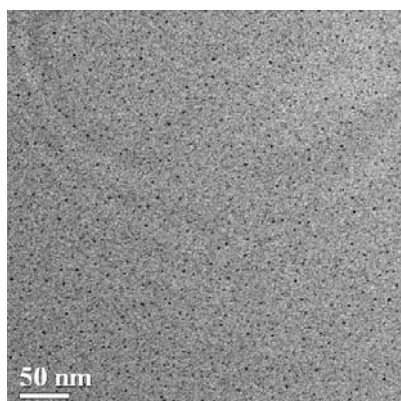
Sample 33



Sample 34



Sample 37

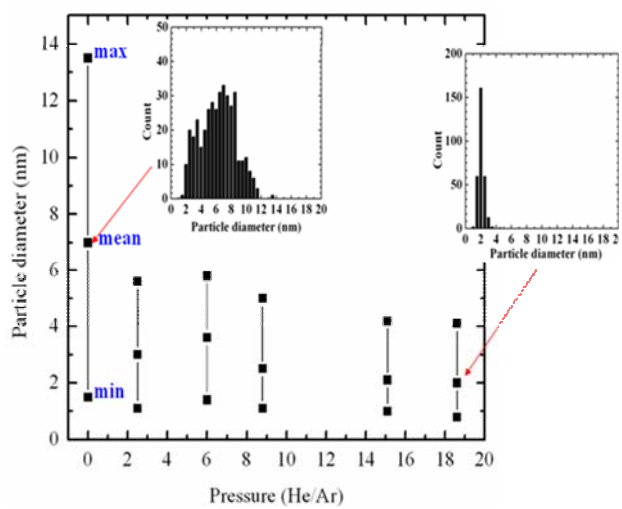


Experimental Conditions

sample	Sputter power (watt)	Gas flow rate (sccm)		Pressure (torr)	Dep.time (min)	Agg. Distance (inch)	RFA
		Ar	He				
33	50	0.212	0	1.0×10^{-5}	10	2	No
34	50	0.217	5	2.4×10^{-5}	10	2	No
37	50	0.217	14	4.6×10^{-5}	10	2	No

* Pressures are not much different due to main chamber pressure.

Particle Size Distribution



APPENDIX C

ION ENERGY DISTRIBUTION OF 1ST VERSION RFA

An increasing sputter power increased the center peak of the ion energy distribution, and an increased aggregation distance decreased cluster ion flux.

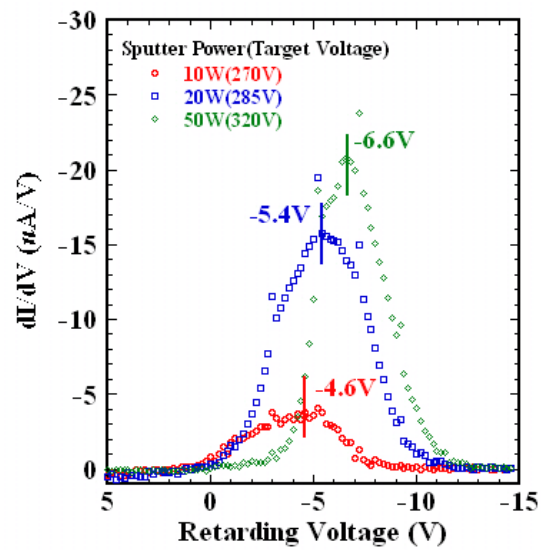


Figure 47. Ion energy distribution at 4" aggregation distance.

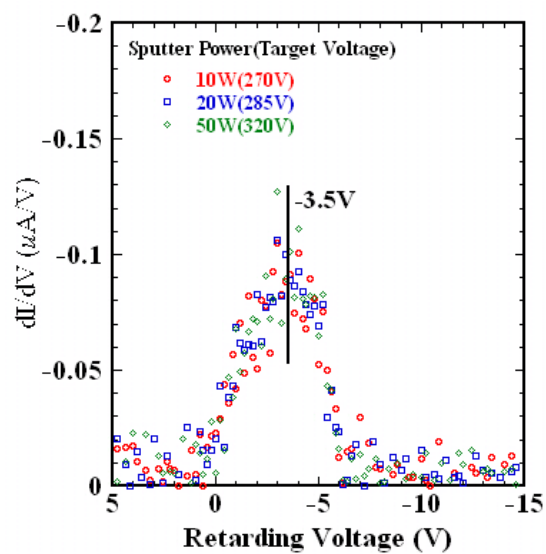


Figure 48. Ion energy distribution at 6" aggregation distance.

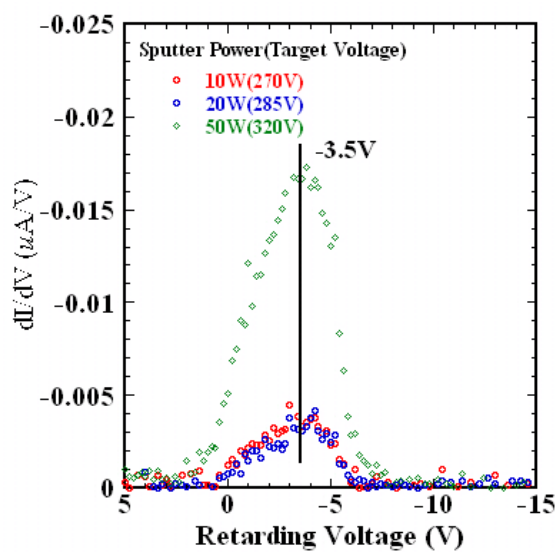
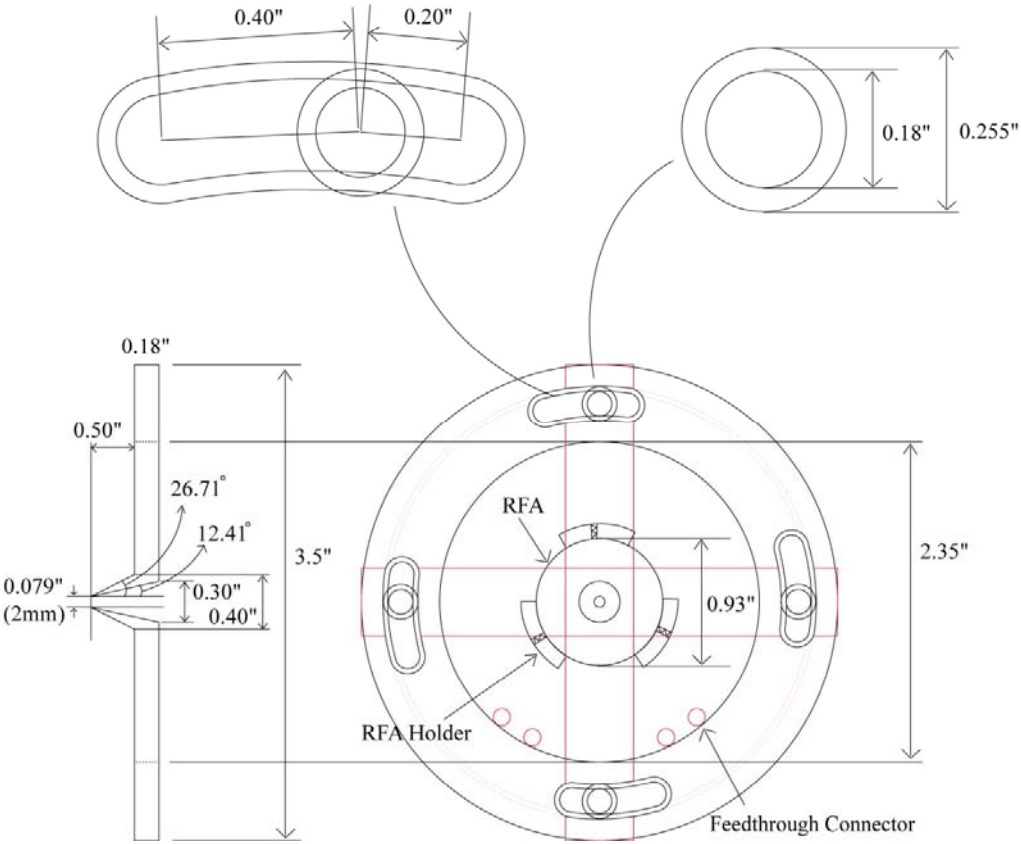


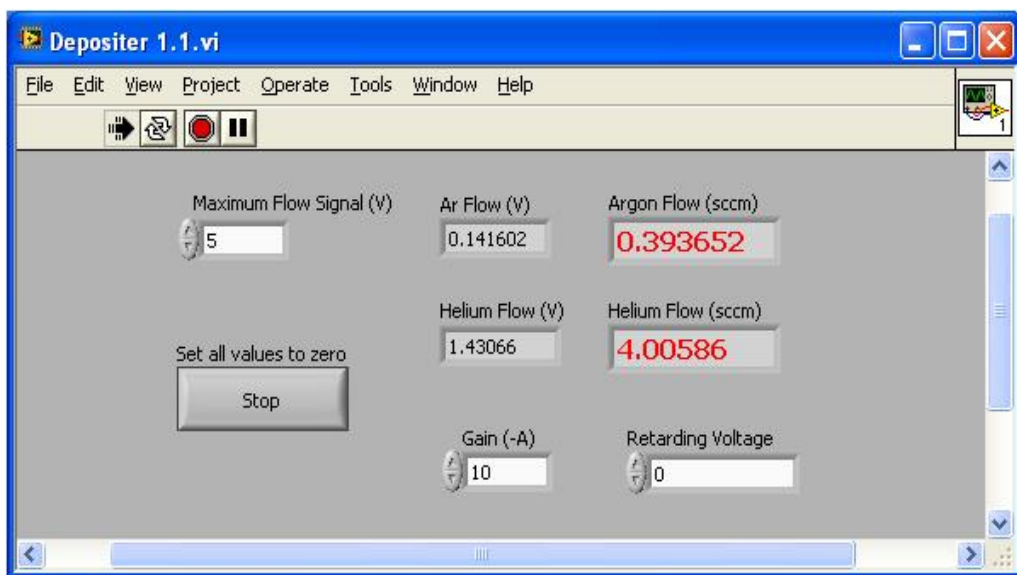
Figure 49. Ion energy distribution at 8" aggregation distance.

APPENDIX D
SCHEMATIC OF APERTURE

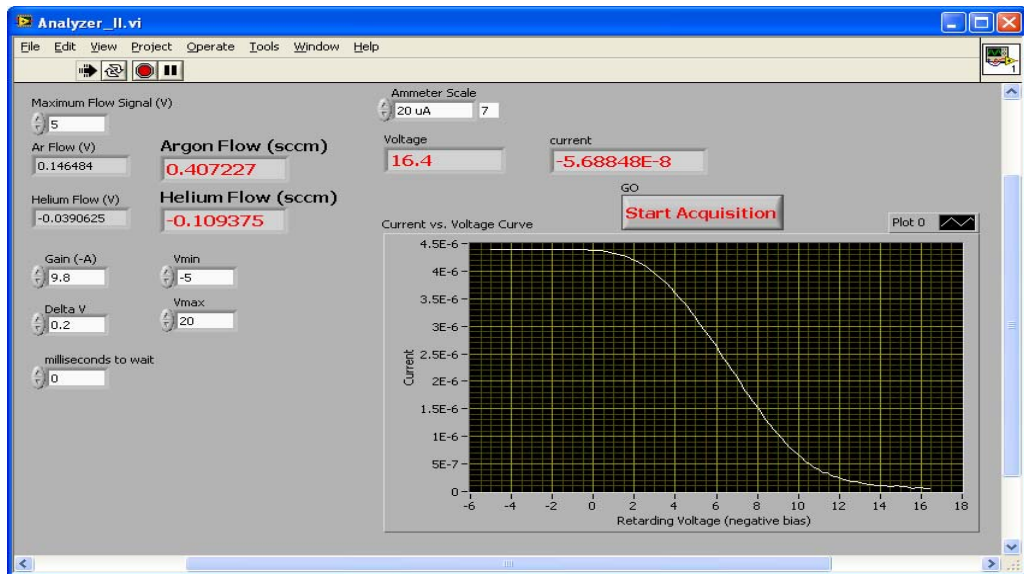


APPENDIX E
LABVIEW PROGRAMMING

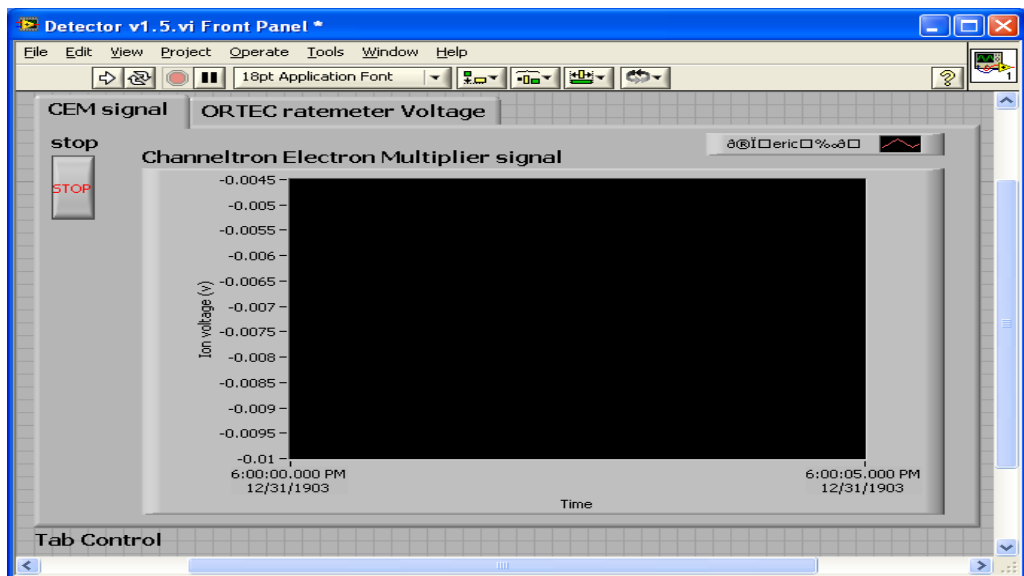
Depositer of Nanoclusters



Analyzer for Measuring Ion Energy Distribution



Detector for Measuring Ion Voltage Signal from CEM.



APPENDIX F

SIMULATION CODING FOR RFA AND LENS

```
; RFA and 1st version lens system with deflector  
; with housing electrode  
; by GiHan Kwon, 1-3-2009
```

```
pa_define(520,130,130,p,n)
```

```
=====
```

```
; housing elemet E1 in Fig.1a of RSI 2008
```

```
locate(0,65,65,,,,0)
```

```
{  
e(1){rotate_fill(360){within{box(27,62,140,54)}}}  
}
```

```
=====
```

```
;Five grids electrodes
```

```
=====
```

```
;Grid 0 : always grounded
```

```
locate(0,65,65,,,,0)
```

```
{  
e(2){rotate_fill(360){  
                          within{box(37,42,45,11)}  
                          within{box(41,11,41,0)}  
                          }  
}  
}
```

```
=====
```

```
;Grid 1
```

```
locate(0,65,65,,,,0)
```

```
{  
e(3){rotate_fill(360){  
                          within{box(57,42,65,16)}  
                          within{box(61,16,61,0)}  
                          }  
}  
}
```

```

}
;
=====
;Grid 2
;
=====
locate(0,65,65,,,,0)
{
e(4){rotate_fill(360){
                within{box(77,42,85,16)}
                within{box(81,16,81,0)}
            }
}
}
;
=====
;Grid 3
;
=====
locate(0,65,65,,,,0)
{
e(5){rotate_fill(360){
                within{box(97,42,105,16)}
                within{box(101,16,101,0)}
            }
}
}
;
=====
;Grid 4: collector
;
=====
locate(0,65,65,,,,0)
{
e(6){rotate_fill(360){within{box(117,42,125,10)}}}
}
;
=====
;Einzel lens system for focusing beam into magnetic
;-sector
;Wall thickness : 6 blocks
;Gap between lens : 6 blocks, Gap = 0.1xdiameter
;Inside diameter of lens : 64 blocks
;Width of lens V1 and V3 : 76 blocks
;width of lens V2 : 89 blocks
;
=====
locate(0,65,65,,,,0)
{
e(7){rotate_fill(360){
                within{box(165,38,241,32)}
                within{box(244,38,333,32)}
                within{box(336,38,412,32)}
            }
}
}

```

```

    }
  }
  ;=====
  ; Four deflector electrodes
  ;=====
  ;locate(0,65,65,,,,0)
  ;{
  ;e(12){rotate_fill(360){within{box(244,38,320,32)}}}
  ;}
  ;locate(0,67,67,,,,0)
  ;{
  ;e(13){rotate_fill(90){within{box(244,36,320,30)}}}
  ;}
  ;locate(0,67,63,,,,-90)
  ;{
  ;e(14){rotate_fill(90){within{box(244,36,320,30)}}}
  ;}
  ;locate(0,63,63,,,,-180)
  ;{
  ;e(15){rotate_fill(90){within{box(244,36,320,30)}}}
  ;}
  ;locate(0,63,67,,,,90)
  ;{
  ;e(16){rotate_fill(90){within{box(244,36,320,30)}}}
  ;}
  ;=====
  ;locate(0,65,65,,,,0)
  ;{
  ;e(17){rotate_fill(360){within{box(323,38,412,32)}}}
  ;}
  ;locate(0,65,65,,,,0)
  ;{
  ;e(18){rotate_fill(360){within{box(415,38,494,32)}}}
  ;}

; RFA and 2nd version lens system
; with housing electrode
; by GiHan Kwon, 1-3-2009

pa_define(720,130,130,p,n)
;=====
; housing elemet E1 in Fig.1a of RSI 2008
;=====
locate(0,65,65,,,,0)
{

```

```
e(1){rotate_fill(360){within{box(27,62,140,48)}}}
}
```

```
=====
;Five grids electrodes
=====
```

```
=====
;Grid 0 : always grounded
=====
```

```
locate(0,65,65,,,,0)
{
e(2){rotate_fill(360){
      within{box(37,42,45,11)}
      within{box(41,11,41,0)}
    }
}
}
```

```
=====
;Grid 1
=====
```

```
locate(0,65,65,,,,0)
{
e(3){rotate_fill(360){
      within{box(57,42,65,16)}
      within{box(61,16,61,0)}
    }
}
}
```

```
=====
;Grid 2
=====
```

```
locate(0,65,65,,,,0)
{
e(4){rotate_fill(360){
      within{box(77,42,85,16)}
      within{box(81,16,81,0)}
    }
}
}
```

```
=====
;Grid 3
=====
```

```
locate(0,65,65,,,,0)
{
e(5){rotate_fill(360){
      within{box(97,42,105,16)}
      within{box(101,16,101,0)}
    }
}
```

```

    }
  }
}
=====
;Grid 4: collector
=====
locate(0,65,65,,,,0)
{
e(6){rotate_fill(360){within{box(117,42,125,10)}}}
}
=====
;Einzel lens system for focusing beam into magnetic
;-sector
;Wall thickness : 6 blocks
;Gap between lens : 6 blocks, Gap = 0.1xdiameter
;Inside diameter of lens : 64 blocks
;Width of lens V1 and V3 : 76 blocks
;width of lens V2 : 89 blocks
=====
locate(0,65,65,,,,0)
{
  e(7){
    rotate_fill(360){
      within
        polyline( 165,5,
                  165,18,
                  241,62
                  241,49)}
    }
  rotate_fill(360){within{box(242,62,317,48)}}
}
}
locate(0,65,65,,,,0)
{
e(8){rotate_fill(360){within{box(322,62,474,48)}}}
}
locate(0,65,65,,,,0)
{
e(9){
  rotate_fill(360){
    within{box(479,62,631,48)}
    within{box(632,62,644,13)}
    within{box(645,20,696,13)}
  }
}
}

```

APPENDIX G

SIMULATION CODING FOR MSMF

```
; Magnetic field : a completely uniform B-field  
pa_define(90,90,160,planar,non-mirrored,m,13)  
e(0){fill{within{box3d(20,43,26,69,30,128)}}}  
e(1){fill{within{box3d(20,69,26,69,56,128)}}}
```

```
-- SIMION workbench Lua program to apply magnetic field from CSV file.  
--"MyFieldArray" was made by D. Manura.  
--"magneticfield.csv" was made by Gihan  
simion.workbench_program()  
-- Load field interpolation support.  
local FieldArray = require "MyFieldArray"
```

APPENDIX H

MAXIMUM CLUSTER LANDING ENERGY

Fundamental data for calculation

Bond length between silver atom (d) = 0.2889nm (<http://www.webelements.com>)

Radius of silver atom (r) = bond length of silver atom (d) / 2 = 0.1445nm

$$\text{Volume of silver atom} = \frac{4 \times \pi \times r^3}{3} = 0.0126 \text{ nm}^3$$

Density of silver = 10500000 nanogram / nm³

Number of silver atom in cluster = volume of silver cluster / volume of silver atom

For example of 1nm diameter of Ag cluster,

$$41.5 \text{ atoms in cluster} = 0.523 \text{ nm}^3 / 0.0126 \text{ nm}^3$$

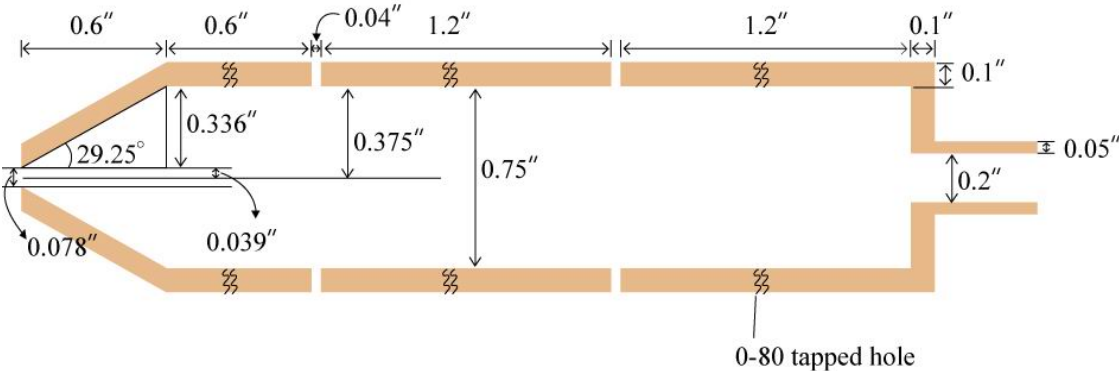
Maximum cluster landing energy = Maximum ion energy / minimum cluster size

Pressure ratio (He/Ar)	Maximum cluster energy (eV)	Minimum cluster diameter (nm)	Minimum number of atom	Maximum cluster landing energy (eV)
0	15	0.5	5.2	2.88
2.5	15	2	331.8	0.05
4.5	10	1.5	140	0.07
6	7	1	41.5	0.17
9.5	4	1	41.5	0.10
12	1	-	-	-

APPENDIX I

SCHEMATIC DIAGRAM OF 2nd VERSION OF LENS AND LENS HOLDER

Schematic Diagram of 2nd Version of Lens



Lens Holder

